Site-selective Labeling of the Nitrogenase Iron-Molybdenum Cofactor

By

Edward D. Badding

B.S., Pennsylvania State University, 2017

Submitted to the Department of Chemistry
in Partial Fulfillment of the Requirements for the Degree of

DOCTOR OF PHILOSOPHY IN CHEMISTRY

at the

MASSACHUSETTS INSTITUTE OF TECHNOLOGY

June 2023

Authored by: Edward D. Badding

Department of Chemistry

April 14th, 2023

Certified by: Daniel L. M. Suess

Associate Professor of Chemistry, Thesis Supervisor

Accepted by: Adam Willard

Associate Professor of Chemistry

Graduate Officer

This doctoral thesis has been examined by a committee of the Department of Chemistry as follows:

Professor Elizabeth M. Nolan _____

Ivan R. Cottrell Professor of Immunology
Thesis Committee Chair

Professor Daniel L. M. Suess_____

Associate Professor
Thesis Supervisor

Professor Catherine L. Drennan_____

Professor of Biology and Chemistry
Investigator and Professor, Howard Hughes Medical Institute
Thesis Committee Member

Site-selective Labeling of the Nitrogenase Iron-Molybdenum Cofactor

Edward D. Badding

Submitted to the Department of Chemistry on May 12th, 2023 in Partial Fulfillment of the Requirement for the Degree of Doctor of Philosophy in Chemistry

ABSTRACT

Nitrogenases are enzymes known to catalyze the kinetically challenging, and biologically important, reduction of N_2 to NH_3. The mechanism of these enzymes, and in particular, the chemistry that occurs at the catalytic cofactor of the Mo nitrogenase, the iron-molybdenum cofactor (FeMo-co), has been studied for decades. A challenge in understanding its unique reactivity is knowing how the valence electrons of FeMo-co are distributed and coupled, and how those change during catalysis. Because the large number of metal sites present within FeMo-co gives rise to a complex set of spectroscopic responses, correlating that information to a specific metal site within the three-dimensional structure is a substantial challenge. My thesis is focused on addressing this problem by incorporating ^{57}Fe site-selectively within FeMo-co—specifically its terminal Fe site (Fe1). Spectroscopic analysis of the site-selectively labeled Mo nitrogenase in its resting state informed on the valence and spin orientation of the Fe1 site, and as a result, ruled out multiple proposed spin-coupling schemes for the entire cluster. Characterization of the oxidized resting state and the first intermediate of nitrogen fixation provided insight into the cofactor's redox chemistry, and established the utility for using this methodology to study other states of FeMo-co. Finally, the methodology to site-selectively label FeMo-co was expanded to manipulate its chemical composition by substituting the Fe1 site with Co^{2+}. Incorporation of this new artificial metallocofactor into the Mo nitrogenase and its subsequent characterization revealed that, within the same charge state, CoFeMo-co is EPR active for states that are EPR silent in the WT enzyme. This work opens the door for studying these states using advanced EPR techniques or magnetic Mössbauer spectroscopy.

Thesis Supervisor: Daniel L. M. Suess

Title: Associate Professor

To my father,
John V. Badding
(1962-2019)

ACKNOWLEDGEMENTS

Working at MIT for the past 6 years has been truly a fantastic experience; 10 years ago, I could not have imagined myself having the privilege to be surrounded by so many bright and incredible people. I have many people to thank. First, I would like to thank Dan for his years of mentorship and support; I have learned a tremendous amount from him. My grandfather has lectured me relentlessly (even at the end of my PhD) on how choosing the right PI is one of the most important decisions of my professional career. All I can say is I would do it all again if I could. Dan is someone who I try to aspire to be, and I loved working at MIT largely thanks to him and the space he has created. Additionally, my thesis committee members, Prof. Cathy Drennan and Prof. Liz Nolan, have provided valuable advice not only on my science, but as well as my professional career—particularly towards the end of my PhD—and for that I thank them.

I would like to thank the past and present Suess lab members: Alex, Soop, Gil, Arun, Mengshan, Jess, Nik, Joe, Alex M., Trever, Brighton, Brittany, Hyunsoo, Mackenzie, Madeleine, Young, Anna, and Josh. Everyone in this lab is so talented and knowledgeable; it was easy to talk to anyone about science or honestly anything. Arun has my thanks for being the person I could nerd out with: from talking about recent papers published, to talking about the lore of Lord of the Rings and Star Wars. Our recent visit to NYC to watch the LotR: The Fellowship of the Ring with a live orchestra was awesome. Additionally, I'll hold the memories of cooking together fondly: like making (sort of) ice cream by hand or pizza from scratch (they were delicious). Mengshan has my appreciation for her ability to simultaneously bring this intense but fun atmosphere to the group; she contributed to so many of what I thought were iconic moments in the lab: "my mind is going cloudy", when she realized she drew a knife for the word "fork", or several of her intense group meetings where she broke down some pretty complicated concepts. She helped create such a great atmosphere to work in, and I look forward to seeing her again in Berkeley in the Fall. I'd also like to thank Joe who sat next to my desk for 2 years; he never failed to make me smile with his jokes like "hmmmmDSO". Shoutout to Jess who had this ability to make me laugh what felt like almost every day and was always

ready to chat about anything. Nik has my thanks for his mentorship. He quite literally is one of the brightest people I have ever had the pleasure to work with. I really appreciated the time he took to support me and the rest of the lab when we were younger students.

The work in my thesis would not have been possible without my labmates Soop and Gil; I have worked very closely with them for most of my PhD. Soop was basically my "brother in nitrogenase" for six years. He is an incredible scientist and he contributed so much to making my science better. Beyond working in the lab, he has been a great friend. I will remember our awesome trips to NYC for the US Open in 2018 (shout out to the infamous brunch) and in 2019, as well as his support in getting me to weightlift! I'll always look back fondly at our time together at MIT. Gil has my eternal appreciation for his patience, his constant support, and all the time he took to entertain the discussions we had about our science and the literature. Working with these two so closely has been an incredible honor and I will miss their companionship. I will especially miss the almost daily impromptu mini-subgroup meetings.

I'd also like to thank Zhiyong, Dmitriy, Emilio, Valarie, Lance, Dennis, and Brian for their help and collaboration. Starting up the lab was at times very challenging, and I appreciated their enthusiasm and time when we asked to meet and discuss various problems I had in the lab. I would also like to thank Valarie and Dennis for sending us the numerous strains and plasmids I used throughout my PhD. Thanks to Emilio who visited our lab and taught me how determine the C_2H_2 reduction specific activity of our samples. Dmitriy and Brian, I really appreciated the effort and time they put in on the ^{57}Fe selective labeling; the ENDOR data is beautiful.

As part of my first year at MIT, I was excited to do a short rotation with Dan in the summer between graduating from Penn State and formally starting my PhD at MIT. Fortunately for me, Alex Brown, also had the same idea. That summer was truly an experience; it was a lot of fun, and I am glad to have met her. I'll treasure the times when we marathon'd various shows, the dinners we cooked, our (often) adventures into the labyrinth that is the MIT basement, our walks outside MIT, walks to get coffee…there's too much to list! Alex has constantly inspired me as a scientist and friend. I greatly appreciate her friendship and support inside and outside of the lab.

I'd like to thank the various people I overlapped with at MIT who were great mentors and friends. I greatly appreciate John and Walt at the DCIF who have kept the EPR running smoothly for my entire PhD. Thanks to John especially for his time teaching me how to warm and cool the EPR and responding after hours when I would screw something up in my first couple years here. Thanks to the Lippard lab: Chris, Jake, Fang, and Amanda who all provided support when we were first started in 2017. Thanks to the Drennan lab: Steve, Alison, Gisele, Mary, Kelsey, and Francesca. Y'all are a great group to hang out and talk science with! Thanks to Phil from the Kiessling lab; I appreciated his friendship and mentorship. Thanks to the friends I made from the '17 cohort: Dio, Francesca, Katherine, Mike, Tony, Jessica, Will, Alex K., Andrew, and Steph.

A big thanks to my past and present roommates at 158 Holland Street: Dio, Tim, Mike, Jackson, and Selorm. It's been great forming so many memories from just chilling in the living room, cooking together, or throwing one of our many parties. Dio has been one of my closest friends here at MIT. I first met Dio at the Harvard and MIT visits (we were roommates at Harvard), and I was so glad he ended up coming to MIT because I still remember how we just fed off each other's energy at the visit weekends. I've learned so much from Dio and I have had so much fun being his friend and roommate. I will cherish our random trips (always done at the last minute), like going to Puerto Rico, the US open trips in '18 and '19, the trips around Mass, the Tennis HOF in Newport, the MV marathon, all the 5Ks we did, and again too much to list. Thanks to Tim, who I've known for about a decade now. I've appreciated his comradery from our first days in organic chem. 1 to being roommates. We've shared so many laughs over beer, the video games we've played, watching the Penn State Football games, and the TV shows we'd watch together. Thanks to both of you for making my time in Boston so great.

Shoutout to the MIT club tennis team, in particular Neeraj, Arun K., Joseph, Alex B. (Deans!), Sarah, Avi, Stephanie, Nikhil, Ilan, Harsh, Vidit and Alex C. I wish I had joined the club tennis team earlier than my 3rd year; being around so many great people to play tennis with was always a highlight to my weeks here. This was especially the case when the science wasn't going as smoothly as I'd liked. It was always great to take some of that negative energy out on the fuzzy tennis balls.

I'd like to express my gratitude to my previous mentors and friends from State College and Penn State: my undergraduate advisor, Squire Booker, and the rest of the Booker lab (Tyler, Erin, Joey, Matt, Bo, Nick, Brad, Erica, and Hayley). Their support and mentorship with bioinorganic chemistry, particularly working with FeS cluster-containing enzymes, was invaluable in starting up the nitrogenase research. Thanks to Sarah Chang who I've known since high school; I always enjoyed cooking together, getting drinks, or getting dinner. Thanks to Ben Woolston who I've played tennis with since high school and provided a lot of advice when we met up again here in Boston.

Finally, I'd like to thank my family. I want to express my gratitude to my father, who unexpectedly passed away in 2019. He is one of the biggest reasons I had the opportunity to pursue my PhD at MIT. He constantly supported me throughout my life. Without his guidance, I would not be at MIT today and I miss him dearly. I'd like to thank my mother who somehow always brought a gift that I didn't know I needed/wanted when she would visit Boston; the amount of incredibly soft blankets and socks that keep me warm are all thanks to her. Thanks to my sister, Cathy, who is in the Freedman lab here at MIT. She has provided a lot of support to me throughout my PhD and it's been great to have family here in the department. I'd like to thank my grandparents for their constant support and love. Thanks to my extended family, Uncle Mike, Aunt Margaret, Margaret Ellen, and Michael. I appreciate your support and providing another home for my family after my father's death. I would also like to thank Mark and my great Aunt Margaret who also came up and supported my family when my father passed away.

This thesis is comprised of materials adapted from the following publications or collaborations. The funding for the work discussed in this thesis was provided by MIT and the NIH.

Chapters 2 and 3 consist of work published from:

Badding E. D., Srisantitham, S., Lukoyanov, D.A., Hoffman, B.M., Suess, D. L.M., Connecting the geometric and electronic structures of the nitrogenase iron–molybdenum cofactor through site-selective ^{57}Fe labeling. Nat. Chem. 2023, https://doi.org/10.1038/s41557-023-01154-9

The ^{57}Fe ENDOR data presented in Chapter 2 was performed in collaboration with the Hoffman lab at Northwestern. Dmitriy Lukayanov performed the ^{57}Fe ENDOR experiments. Dmitriy Lukayanov and Brian M. Hoffman performed the data analysis.

Chapter 4 consists of work done in collaboration with Gil Namkoong, who helped work on developing protocols for minimizing the amount of FeMo-co generated during CoFeMo-co reconstitution.

Table of Contents

Table of Figures

Table of Tables

Chapter 1: Mechanistic studies of nitrogenases

1.1. Brief overview of nitrogenases

Nitrogen is an indispensable component of life, and is often a limiting nutrient.[1-3] Despite the atmosphere containing a large source of nitrogen, in its molecular form, dinitrogen (N_2), most organisms cannot use N_2 as a building block; instead, nature relies on more bioavailable forms of nitrogen, such as ammonia (NH_3).[4] While reduction of N_2 to NH_3 is thermodynamically feasible under ambient conditions, it is kinetically very challenging because the first step, cleavage of the N≡N triple bond, is so unfavorable. A specific group of organisms called diazotrophs encode a unique class of enzymes called nitrogenases that catalyze the reduction of N_2 to NH_3 under physiological conditions (Fig. 1A). Diazotrophs are vital to the sustainability of our biosphere as they provide a constant influx of bioavailable nitrogen. It is estimated altogether these organisms provide about half of the Earth's fixed nitrogen each year, the other half coming from the Haber–Bosch process and lightning strikes.[5]

Nitrogenases have been studied extensively because of the kinetic challenges associated with N_2 fixation and its importance to the sustainability of our planet.[6-11] To date, only three isozymes of nitrogenase have been discovered: the molybdenum (Mo), vanadium (V), and all-iron (Fe) nitrogenase.[12] All three isozymes are believed to have a similar architecture and mechanism based on genetic, kinetic, spectroscopic, and crystallographic studies.[9-11, 13] Each isozyme is comprised of two-components: (1) a reductase, which transfers electrons in an ATP dependent-fashion; and (2) a dinitrogenase, which is composed of 2–3 gene products (depending on the specific isozyme) and contains the active site of N_2 reduction.

The most well-characterized isozyme is the Mo nitrogenase from the diazotroph *Azotobacter vinelandii*.[7, 14] It is comprised of the Fe protein (NifH or FeP), the reductase, and the MoFe protein (NifDK), the dinitrogenase. The FeP is a homodimer that contains an Fe_4S_4 cluster bound at the dimer interface, and as discussed above, is responsible for transferring electrons to NifDK in an ATP-dependent manner.[7] NifDK is an $\alpha_2\beta_2$ tetramer (Fig. 1.1A) and contains two oxygen-sensitive metalloclusters. The P-cluster (Fig. 1.1B,

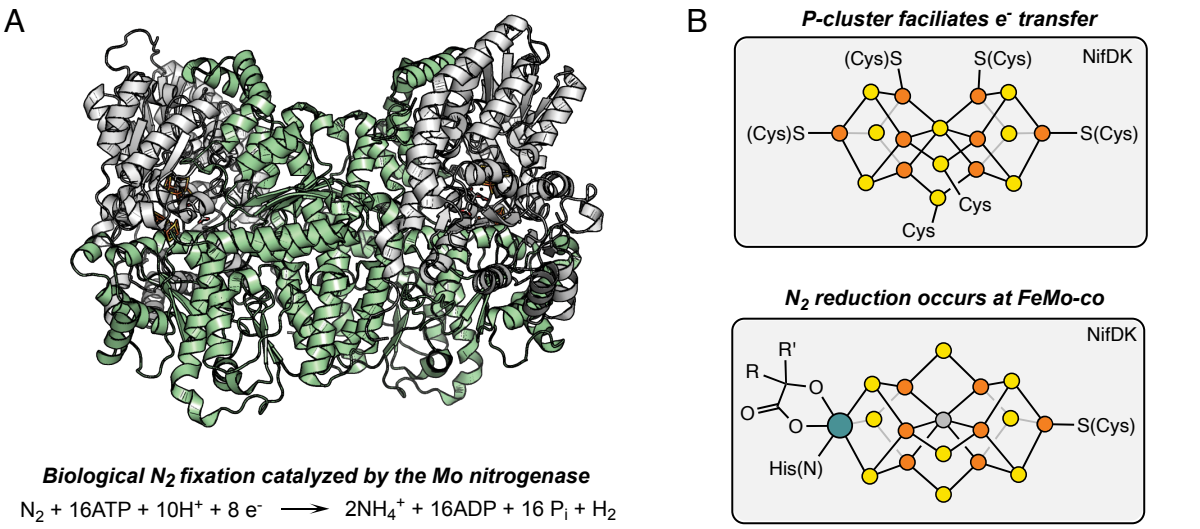

Figure 1.1 The overall architecture of the MoFe protein (NifDK). A, The crystal structure of NifDK and the overall reaction the Mo nitrogenase catalyzes. NifD and NifK are in gray and green, respectively **B,** The chemical structures of the P-cluster (top) and FeMo-co (bottom) and their respective roles in biological nitrogen fixation. PDB accession code 3U7Q. Orange, yellow, teal, and gray circles represent Fe, S, Mo, and C atoms, respectively.

top) is an Fe_8S_7 cluster bound at each interface of the heterodimer and facilitates the electron transfer between the FeP and the iron-molybdenum cofactor (FeMo-co) during catalysis. The second cofactor, FeMo-co, is a complex FeS cluster and is the site of N_2 reduction (Fig. 1.1B, bottom).[15]

In vitro kinetic studies of the Mo nitrogenase conducted by Lowe and Thorneley[7, 16] established a working kinetic model for N_2 reduction (Fig. 1.2).[8] In this model there are nine potential redox states (E_0–E_8) of NifDK, each related to one another by the addition of a proton and an electron. Because the rate limiting step is the release of inorganic phosphate from the FeP,[17] all nine "E" states of NifDK are populated under steady state; this characteristic of the Mo nitrogenase makes it difficult to study the enzyme under turnover conditions. Despite being a perpetual challenge, various groups have overcome this problem for the Mo nitrogenase by either changing the pH,[18] using site-directed mutagenesis,[19-21] tuning the flux of electron transfer,[22-24] and/or adding alternative substrates or inhibitors,[25-29] or any combination thereof to accumulate various states of FeMo-co (Table 1.1).[9, 14]

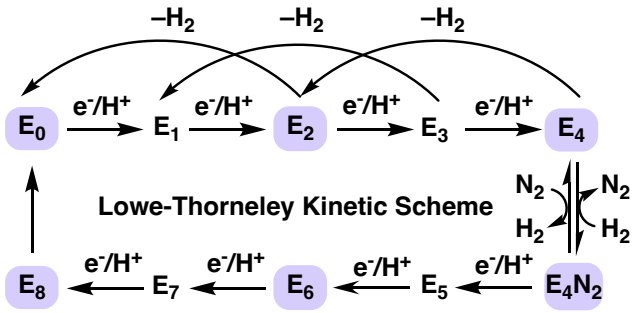

Figure 1.2. The simplified Lowe-Thorneley (LT) kinetic scheme. The simplified LT kinetic scheme of biological nitrogen fixation that guides mechanistic studies of FeMo-co. The states highlighted in light blue indicate that these states contain an odd number of electrons and therefore should be EPR active.

Table 1.1. Selected list of reported states of FeMo-co

	NifDK construct	*g*-values	Spin-state	Refs.
E_0/M^N	wt	[4.32, 3.65, 2.01]	3/2	22-23, 30
$E_0(H^+)$	wt	[4.71, 3.20, 2.01]	3/2	18
E_1/M^R	wt	-	1 or 2	22, 23–24
E_4(4H)	V70I	[2.15, 2.00,1.97]	1/2	20-21, 29
E_4(2H)*	V70I	[2.10, 2.00, 1.96]	1/2	21
E_4(2N2H)	wt	[2.09, 1.99, 1.97]	1/2	29
S_{EPR1} (C_2H_2 bound)	H195Q	[2.12, 2.00, 1.99]	1/2	27
Propargyl alcohol bound state	V70A	[2.12, 2.00, 1.87]	1/2	28
hiCO	wt	[2.17, 2.06, 2.06]	1/2	25, 26
loCO	wt	[2.09, 1.97, 1.93]	1/2	25, 26

While the field has amassed a myriad of states of FeMo-co, the tools to understand the changes to the chemical and electronic structure upon their generation have lagged. Even in the most well characterized state of NifDK, the resting state (E_0), it is still debated how many valence electrons are present in FeMo-co, how they are distributed among the eight metal centers, and how they are coupled to one another; these questions become even harder to address when studying any state beyond E_0. The next part of this chapter will discuss the current set of tools used to study the electronic structure of FeMo-co, particularly in its resting state, the issues the studies faced, and how my work will begin to address some of these challenges.

1.2. Previous studies on the electronic structure of FeMo-co in its resting state

Mössbauer and ^{57}Fe ENDOR spectroscopy, particularly when used together, can provide a wealth of information on any Fe site enriched with ^{57}Fe, including the Fe oxidation states, the covalency of Fe–L and Fe–M interactions, the local electronic-spin states, and the orientations of the valence electrons with respect to the total electronic spin. As such, both techniques have played a critical role in not only understanding the electronic structure of FeMo-co, but in any Fe-containing system.

A prerequisite for using ^{57}Fe ENDOR spectroscopy is that the species of interest must have an odd number of electrons—*i.e.* it must have an observable EPR signal. These aspects of ^{57}Fe ENDOR spectroscopy can be beneficial because it was established early on that when NifDK is in its resting state, FeMo-co exhibits a strong $S = {}^3/_2$ signal (Fig. 1.3A),[30] while the P-cluster is EPR silent.[31-35] Therefore, when samples of NifDK are prepared from cells cultivated with an Fe source enriched with ^{57}Fe, FeMo-co can be selectively probed despite the P-cluster also being enriched. The early ^{57}Fe ENDOR studies[36] of FeMo-co determined the precise hyperfine tensors of at least six of the Fe sites (A^1–A^3, B^1–B^2, where the *A* and *B* sites have negative and positive a_{iso}, respectively), with one of the *B* sites being degenerate. This data showed (1) that there had to be at least six Fe sites within FeMo-co (this was heavily debated at the time); and (2) that most of the Fe sites are magnetically unique. In addition, the study provided the hyperfine tensors that can be fixed for simulation of the magnetic Mössbauer data.

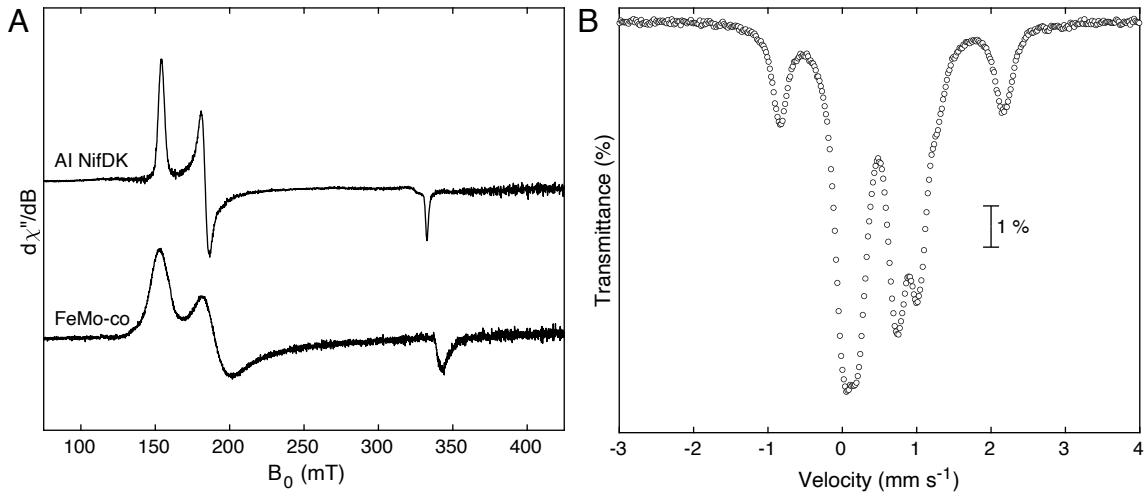

Figure 1.3. Representative Mössbauer and EPR spectra of NifDK and FeMo-co. A, CW EPR spectra of as-isolated (AI) NifDK (top) and isolated FeMo-co in NMF (bottom) in the dithionite reduced state. **B,** The Mössbauer spectrum of NifDK–P($^{57}Fe_8$)–M($^{57}Fe_7$) (all Fe sites within NifDK are enriched with ^{57}Fe) at 80 K.

Mössbauer spectroscopy, unlike ^{57}Fe ENDOR spectroscopy, probes all Fe sites enriched with ^{57}Fe, regardless of the spin state of the molecule. While this technique is indispensable for studying Fe-containing systems, the early Mössbauer studies of NifDK[31-32, 37] suffered due to its inherent low resolution. Because the Mössbauer samples were prepared from cultures enriched with ^{57}Fe, both the P-cluster and FeMo-co were enriched. The complete ^{57}Fe enrichment of NifDK made data analysis extremely difficult to interpret because the spectra had signal contributions from the eight Fe sites of the P-cluster and the seven Fe sites from FeMo-co (NifDK–P($^{57}Fe_8$)–M($^{57}Fe_7$)). Since all the Fe sites within these complex cofactors are tetrahedral, are comprised of formally Fe^{2+} and Fe^{3+}, and are coordinated by similar ligands, their Mössbauer signals largely overlapped (Fig 1.3B), which prevented any in-depth analysis of the Fe sites within FeMo-co. This problem was addressed by generating a sample in which only FeMo-co is labeled with ^{57}Fe (NifDK–M($^{57}Fe_7$)).[22] Such a sample was prepared by isolating[38] ^{57}Fe-enriched FeMo-co from ^{57}Fe-enriched NifDK and inserting it into purified FeMo-co-deficient NifDK (apo-NifDK) that contained natural abundance Fe.[39] The generation of this Mössbauer spectrum minimizes the contribution from the P-cluster Fe sites (as these sites are labeled with the natural abundance of ^{57}Fe, 2.2%), allowing for a more interpretable set of

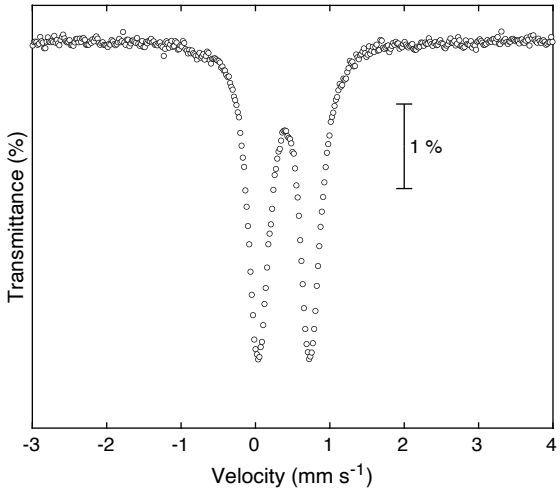

Figure 1.4. Representative Mössbauer spectrum of NifDK in which only FeMo-co is enriched with ^{57}Fe. The 80 K Mössbauer spectra of the NifDK–M($^{57}Fe_7$) sample highlighting the increased resolution obtained from cluster specific labeling. Note the disappearance of the quadrupole doublets corresponding to the P-cluster, particular those around 0 and 1.1 mm s^{-1} (when compared to Fig. 1.3B).

Mössbauer data (Fig. 1.4). Guided by the previous Mössbauer and ^{57}Fe ENDOR studies,[30-33, 36-37] the authors pursued what remains the most comprehensive Mössbauer study of FeMo-co, and provided a working set of Mössbauer parameters for all seven Fe sites of FeMo-co (in M^N) (Table 1.2). Based on these parameters and previous studies attempting to assign the formal valence of the Mo site,[26, 40] the authors proposed that FeMo-co was comprised of: Mo^{4+}-$3Fe^{3+}$-$4Fe^{2+}$. However, the authors acknowledged: (1) the difficulties in simulating the Mössbauer data due to the poor resolution of the Fe sites (even with the selective labeling of FeMo-co), as well as the large number of parameters required (as many as 84 hyperfine parameters!); and (2) the limitations of their interpretation owing to the inability to assign the spectroscopic features to specific sites in the structure.

Few experimental methods have been able to connect the spectroscopic and structural properties of FeMo-co. For example, a recent spatially resolved anomalous dispersion (SpReAD) analysis[41] of NifDK crystals was able to assign formal valences to each of the Fe sites within FeMo-co by effectively building an X-ray absorption spectrum for an individual metal site based on its anomalous scattering. By using the P-cluster in

Table 1.2. The 4.2 K Hyperfine Parameters of FeMo-co in M^N taken from Yoo and coauthors[22]

	A^1	A^2	A^3	A^4	B^1	B^2
δ (mm s^{-1})	0.39	0.48	0.39	0.41	0.33	0.50
ΔE_Q (mm s^{-1})	–0.69	–0.94	–0.56	0.68	–0.66	–0.65
η	1	1	1	1	0.9	1
α_{efg}	120	115	60	0	40	6
$ß_{efg}$	0	20	30	130	125	70
γ_{efg}	0	4	176	30	0	0
A_x (MHz)	–13.8	–17.3	–13.9	–1.5	11.7	8.5
A_y (MHz)	–21.1	–15.1	–11.6	–9.5	14.1	11.0
A_z (MHz)	–19	–19	–10	0	9.2	8.2
α_A	20	13	25	112	0	9
$ß_A$	0	22	0	60	56	0
γ_A	0	0	0	0	0	0

the P^N state (all ferrous) as an internal reference, the authors were able to compare the SpReAD profiles of each of the Fe sites of FeMo-co to the Fe sites of the P-cluster. Through this analysis, the authors determined that Fe1, Fe3, and Fe7 were more "reduced" (*i.e.* ferrous-like) than the rest of the Fe sites. This data are consistent with a Mo^{3+}-$4Fe^{3+}$-$3Fe^{2+}$ configuration, which has been proposed in recent computational[42-43] and experimental studies.[44] However, there are several drawbacks to SpReAD: (1) its inherent low resolution to differences in oxidation state; (2) its reliance on needing a crystal which prohibits studying the electronic structure of any short-lived intermediate; and (3) the lack of any insight into the magnetic behavior of individual metal sites (*e.g.*, the orientation of the local electronic spin of each metal site with respect to the total electronic spin).

1.3. Brief discussion of the layout of the thesis

The work in my thesis is focused on developing chemical based tools to address the problem of connecting the spectroscopic and structural properties of FeMo-co in any state. Whereas the information obtained from ^{57}Fe-specific techniques is limited due to

the reasons discussed above, one can begin to overcome these challenges by developing methods to selectively enrich specific Fe sites with ^{57}Fe. This strategy was first explored by the research groups of Orme-Johnson, Burgess, and Münck,[22, 33] who developed methods to generate NifDK samples that contain either selectively labeled P-cluster or FeMo-co. This work enabled assigning the spectroscopic signals to a particular cluster. My thesis is focused on targeting specific site(s) within the seven Fe sites of FeMo-co and replacing it with a spectroscopic probe. The isotopic labeling of a single Fe site with ^{57}Fe will be the focus of Chapters 2 and 3. Pursuing this methodology addresses the issues with resolution (for techniques such as Mössbauer spectroscopy) and the inability to map spectroscopic data to chemical structure. Chapter 2 discusses my efforts on the development and application of this methodology to study FeMo-co in NifDK in E_0, and Chapter 3 will discuss using this methodology to study states beyond E_0. Chapter 4 will discuss the expansion of the site-selective ^{57}Fe labeling strategy to incorporate different transition metals, such as Co, into FeMo-co. Like the site-selective ^{57}Fe labeling, the incorporation of Co also serves as a site-selective probe for mechanistic studies. Furthermore, the introduction of Co^{2+} offsets the total electron count of FeMo-co. As a result, the EPR-active species in the LT kinetic scheme are offset by one, enabling ENDOR (^{57}Fe, Co) and magnetic Mössbauer studies on originally EPR-inactive states.

1.4 References

1. Elser, J. J., Bracken, M. E. S., Cleland, E. E., Gruner, D. S., Harpole, W. S., Hillebrand, H., Ngai, J. T., Seabloom, E. W., Shurin, J. B. & Smith, J. E., Global analysis of nitrogen and phosphorus limitation of primary producers in freshwater, marine and terrestrial ecosystems. *Ecology Letters* **2007,** *10* (12), 1135-1142.
2. LeBauer, D. S. & Treseder, K. K., Nitrogen Limititation of Net Primary Productivity in Terrestrial Ecosystems is Globally Distributed. *Ecology* **2008,** *89* (2), 371-379.
3. Du, E., Terrer, C., Pellegrini, A. F. A., Ahlström, A., van Lissa, C. J., Zhao, X., Xia, N., Wu, X. & Jackson, R. B., Global patterns of terrestrial nitrogen and phosphorus limitation. *Nature Geoscience* **2020,** *13* (3), 221-226.
4. Canfield, D. E., Glazer, A. N. & Falkowski, P. G., The evolution and future of Earth's nitrogen cycle. *Science* **2010,** *330* (6001), 192-6.
5. Igarashi, R. Y. & Seefeldt, L. C., Nitrogen Fixation: The Mechanism of the Mo-Dependent Nitrogenase. *Critical Reviews in Biochemistry and Molecular Biology* **2003,** *38* (4), 351-384.
6. Winter, H. C. & Burris, R. H., Nitrogenase. *Annual Review of Biochemistry* **1976,** *45* (1), 409-426.
7. Burgess, B. K. & Lowe, D. J., Mechanism of Molybdenum Nitrogenase. *Chemical Reviews* **1996,** *96* (7), 2983-3012.
8. Hoffman, B. M., Lukoyanov, D., Yang, Z.-Y., Dean, D. R. & Seefeldt, L. C., Mechanism of Nitrogen Fixation by Nitrogenase: The Next Stage. *Chemical Reviews* **2014,** *114* (8), 4041-4062.
9. Van Stappen, C., Decamps, L., Cutsail, G. E., Bjornsson, R., Henthorn, J. T., Birrell, J. A. & DeBeer, S., The Spectroscopy of Nitrogenases. *Chemical Reviews* **2020,** *120* (12), 5005-5081.
10. Einsle, O. & Rees, D. C., Structural Enzymology of Nitrogenase Enzymes. *Chemical Reviews* **2020,** *120* (12), 4969-5004.
11. Seefeldt, L. C., Yang, Z.-Y., Lukoyanov, D. A., Harris, D. F., Dean, D. R., Raugei, S. & Hoffman, B. M., Reduction of Substrates by Nitrogenases. *Chemical Reviews* **2020,** *120* (12), 5082-5106.
12. Eady, R. R., Structure-Function Relationships of Alternative Nitrogenases. *Chemical Reviews* **1996,** *96* (7), 3013-3030.
13. Burén, S., Jiménez-Vicente, E., Echavarri-Erasun, C. & Rubio, L. M., Biosynthesis of Nitrogenase Cofactors. *Chemical Reviews* **2020,** *120* (12), 4921-4968.
14. Seefeldt, L. C., Hoffman, B. M. & Dean, D. R., Mechanism of Mo-dependent nitrogenase. *Annual Review of Biochemistry* **2009,** *78*, 701-22.
15. Einsle, O., Tezcan, F. A., Andrade, S. L., Schmid, B., Yoshida, M., Howard, J. B. & Rees, D. C., Nitrogenase MoFe-protein at 1.16 A resolution: a central ligand in the FeMo-cofactor. *Science* **2002,** *297* (5587), 1696-700.
16. Thorneley, R. & Lowe, D., Molybdenum Enzymes. Spiro, TG., editor. Vol. Vol. 7. New York: Wiley-Interscience: 1985.
17. Yang, Z.-Y., Ledbetter, R., Shaw, S., Pence, N., Tokmina-Lukaszewska, M., Eilers, B., Guo, Q., Pokhrel, N., Cash, V. L., Dean, D. R., Antony, E., Bothner, B., Peters, J. W.

& Seefeldt, L. C., Evidence That the Pi Release Event Is the Rate-Limiting Step in the Nitrogenase Catalytic Cycle. *Biochemistry* **2016,** *55* (26), 3625-3635.
18. Morrison, C. N., Spatzal, T. & Rees, D. C., Reversible Protonated Resting State of the Nitrogenase Active Site. *Journal of the American Chemical Society* **2017,** *139* (31), 10856-10862.
19. Barney, B. M., Igarashi, R. Y., Dos Santos, P. C., Dean, D. R. & Seefeldt, L. C., Substrate Interaction at an Iron-Sulfur Face of the FeMo-cofactor during Nitrogenase Catalysis*. *Journal of Biological Chemistry* **2004,** *279* (51), 53621-53624.
20. Igarashi, R. Y., Laryukhin, M., Dos Santos, P. C., Lee, H.-I., Dean, D. R., Seefeldt, L. C. & Hoffman, B. M., Trapping H^- Bound to the Nitrogenase FeMo-Cofactor Active Site during H_2 Evolution: Characterization by ENDOR Spectroscopy. *Journal of the American Chemical Society* **2005,** *127* (17), 6231-6241.
21. Lukoyanov, D., Barney, B. M., Dean, D. R., Seefeldt, L. C. & Hoffman, B. M., Connecting nitrogenase intermediates with the kinetic scheme for N_2 reduction by a relaxation protocol and identification of the N_2 binding state. *Proceedings of the National Academy of Sciences* **2007,** *104* (5), 1451-1455.
22. Yoo, S. J., Angove, H. C., Papaefthymiou, V., Burgess, B. K. & Münck, E., Mössbauer Study of the MoFe Protein of Nitrogenase from *Azotobacter vinelandii* Using Selective ^{57}Fe Enrichment of the M-Centers. *Journal of the American Chemical Society* **2000,** *122* (20), 4926-4936.
23. Van Stappen, C., Thorhallsson, A. T., Decamps, L., Bjornsson, R. & DeBeer, S., Resolving the structure of the E_1 state of Mo nitrogenase through Mo and Fe K-edge EXAFS and QM/MM calculations. *Chemical Science* **2019,** *10* (42), 9807-9821.
24. Van Stappen, C., Davydov, R., Yang, Z.-Y., Fan, R., Guo, Y., Bill, E., Seefeldt, L. C., Hoffman, B. M. & DeBeer, S., Spectroscopic Description of the E_1 State of Mo Nitrogenase Based on Mo and Fe X-ray Absorption and Mössbauer Studies. *Inorganic Chemistry* **2019,** *58* (18), 12365-12376.
25. Cameron, L. M. & Hales, B. J., Investigation of CO Binding and Release from Mo-Nitrogenase during Catalytic Turnover. *Biochemistry* **1998,** *37* (26), 9449-9456.
26. Lee, H.-I., Hales, B. J. & Hoffman, B. M., Metal-Ion Valencies of the FeMo Cofactor in CO-Inhibited and Resting State Nitrogenase by 57Fe Q-Band ENDOR. *Journal of the American Chemical Society* **1997,** *119* (47), 11395-11400.
27. Lee, H.-I., Sørlie, M., Christiansen, J., Song, R., Dean, D. R., Hales, B. J. & Hoffman, B. M., Characterization of an Intermediate in the Reduction of Acetylene by the Nitrogenase α-Gln195 MoFe Protein by Q-band EPR and 13C,1H ENDOR. *Journal of the American Chemical Society* **2000,** *122* (23), 5582-5587.
28. Benton, P. M. C., Laryukhin, M., Mayer, S. M., Hoffman, B. M., Dean, D. R. & Seefeldt, L. C., Localization of a Substrate Binding Site on the FeMo-Cofactor in Nitrogenase: Trapping Propargyl Alcohol with an α-70-Substituted MoFe Protein. *Biochemistry* **2003,** *42* (30), 9102-9109.
29. Lukoyanov, D., Khadka, N., Yang, Z.-Y., Dean, D. R., Seefeldt, L. C. & Hoffman, B. M., Reductive Elimination of H2 Activates Nitrogenase to Reduce the N≡N Triple Bond: Characterization of the E4(4H) Janus Intermediate in Wild-Type Enzyme. *Journal of the American Chemical Society* **2016,** *138* (33), 10674-10683.

30. Rawlings, J., Shah, V. K., Chisnell, J. R., Brill, W. J., Zimmermann, R., Münck, E. & Orme-Johnson, W. H., Novel metal cluster in the iron-molybdenum cofactor of nitrogenase. Spectroscopic evidence. *Journal of Biological Chemistry* **1978,** *253* (4), 1001-4.
31. Münck, E., Rhodes, H., Orme-Johnson, W. H., Davis, L. C., Brill, W. J. & Shah, V. K., Nitrogenase. VIII. Mössbauer and EPR spectroscopy. The MoFe protein component from *Azotobacter vinelandii* OP. *Biochimica et Biophysica Acta (BBA) - Protein Structure* **1975,** *400* (1), 32-53.
32. Zimmermann, R., Münck, E., Brill, W. J., Shah, V. K., Henzl, M. T., Rawlings, J. & Orme-Johnson, W. H., Nitrogenase X: Mössbauer and EPR studies on reversibly oxidized MoFe protein from *Azotobacter vinelandii* OP. Nature of the iron centers. *Biochimica et Biophysica Acta (BBA) - Protein Structure* **1978,** *537* (2), 185-207.
33. McLean, P. A., Papaefthymiou, V., Orme-Johnson, W. H. & Münck, E., Isotopic hybrids of nitrogenase. Mössbauer study of MoFe protein with selective ^{57}Fe enrichment of the P-cluster. *Journal of Biological Chemistry* **1987,** *262* (27), 12900-12903.
34. Lindahl, P. A., Papaefthymiou, V., Orme-Johnson, W. H. & Münck, E., Mössbauer studies of solid thionin-oxidized MoFe protein of nitrogenase. *Journal of Biological Chemistry* **1988,** *263* (36), 19412-8.
35. Surerus, K. K., Hendrich, M. P., Christie, P. D., Rottgardt, D., Orme-Johnson, W. H. & Munck, E., Moessbauer and integer-spin EPR of the oxidized P-clusters of nitrogenase: P^{OX} is a non-Kramers system with a nearly degenerate ground doublet. *Journal of the American Chemical Society* **1992,** *114* (22), 8579-8590.
36. True, A. E., Nelson, M. J., Venters, R. A., Orme-Johnson, W. H. & Hoffman, B. M., Iron-57 hyperfine coupling tensors of the FeMo cluster in *Azotobacter vinelandii* MoFe protein: determination by polycrystalline ENDOR spectroscopy. *Journal of the American Chemical Society* **1988,** *110* (6), 1935-1943.
37. Smith, B. E. & Lang, G., Mössbauer spectroscopy of the nitrogenase proteins from Klebsiella pneumoniae. Structural assignments and mechanistic conclusions. *Biochemical Journal* **1974,** *137* (2), 169-80.
38. Shah, V. K. & Brill, W. J., Isolation of an iron-molybdenum cofactor from nitrogenase. *Proceedings of the National Academy of Sciences* **1977,** *74* (8), 3249-53.
39. Christiansen, J., Goodwin, P. J., Lanzilotta, W. N., Seefeldt, L. C. & Dean, D. R., Catalytic and biophysical properties of a nitrogenase Apo-MoFe protein produced by a *nifB*-deletion mutant of *Azotobacter vinelandii*. *Biochemistry* **1998,** *37* (36), 12611-23.
40. Liu, H. I., Burgess, B. K., Natoli, C. R., Filipponi, A., Gavini, N., Hedman, B., Di Cicco, A. & Hodgson, K. O., EXAFS studies of FeMo-cofactor and MoFe protein: Direct evidence for the long-range Mo-Fe-Fe interaction and cyanide binding to the Mo in FeMo-cofactor. *Journal of the American Chemical Society* **1994,** *116* (6), 2418-2423.
41. Spatzal, T., Schlesier, J., Burger, E.-M., Sippel, D., Zhang, L., Andrade, S. L. A., Rees, D. C. & Einsle, O., Nitrogenase FeMoco investigated by spatially resolved anomalous dispersion refinement. *Nature Communications* **2016,** *7* (1), 10902.
42. Bjornsson, R., Neese, F. & DeBeer, S., Revisiting the Mössbauer Isomer Shifts of the FeMoco Cluster of Nitrogenase and the Cofactor Charge. *Inorganic Chemistry* **2017,** *56* (3), 1470-1477.

43. Benediktsson, B. & Bjornsson, R., QM/MM Study of the Nitrogenase MoFe Protein Resting State: Broken-Symmetry States, Protonation States, and QM Region Convergence in the FeMoco Active Site. *Inorganic Chemistry* **2017,** *56* (21), 13417-13429.
44. Bjornsson, R., Lima, F. A., Spatzal, T., Weyhermüller, T., Glatzel, P., Bill, E., Einsle, O., Neese, F. & DeBeer, S., Identification of a spin-coupled Mo(iii) in the nitrogenase iron–molybdenum cofactor. *Chemical Science* **2014,** *5* (8), 3096-3103.

Chapter 2: Connecting the geometric and electronic structures of FeMo-co in M^N

2.1. Addressing the challenges associated with spectroscopic studies of FeMo-co

A persistent challenge in analyzing the ENDOR and Mössbauer data acquired on FeMo-co is the inability to assign the observed spectroscopic features to specific sites in the structure. Although Yoo and coworkers[2] undertook what remains the most comprehensive Mössbauer spectroscopic analysis of FeMo-co—yielding a working set of Mössbauer parameters often used in computational studies—the authors acknowledged the difficulties in simulating the Mössbauer data due to the poor resolution of the data resulting from the overlapping signals from each of the seven Fe sites of FeMo-co. In addition to the challenges associated with modeling the Mössbauer parameters of the seven Fe sites, the authors noted another problem, "We have not yet been able to assign any of the sites identified by ENDOR and Mössbauer spectroscopy to a particular crystallographic site; even the unique tetrahedral iron coordinated by αCys275 does not provide a spectral signature that distinguishes it clearly from the trigonal iron sites." Few experiments allow for the mapping of the electronic structure of FeMo-co onto its geometric structure,[3] and this challenge remains a persistent obstacle in understanding the mechanism of biological nitrogen fixation (Fig. 2.1).

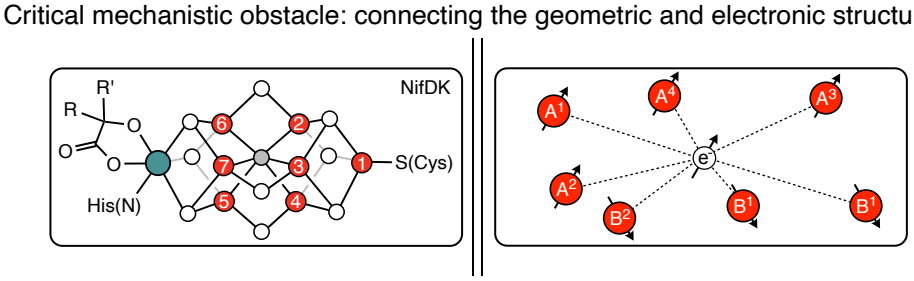

Figure 2.1. A mechanistic obstacle towards understanding biological nitrogen fixation. A major challenge in mechanistic studies of nitrogenases is the inability to correlate the spectroscopic data (right) with the geometric structure of FeMo-co (left). The numbers in red circles correspond to the crystallographically defined Fe sites (Fe1-Fe7) (left). The numbered letters in red circles correspond to the defined spectroscopic sites observed in FeMo-co (see text). The red, teal, white and grey circles represent ^{57}Fe, Mo, S and C atoms, respectively. R,-$CH_2CO_2^-$; R′, -$(CH2)_2CO_2$.

Our strategy to overcome these challenges focuses on the selective enrichment of individual Fe sites within FeMo-co with ^{57}Fe. The analysis of such samples would simultaneously overcome: (1) the issues of poor spectroscopic resolution; and (2) provide site-specific information on the chemical bonding at individual Fe centers in any state. The initial development of this methodology focused on selectively labeling the terminal Fe sites of the L-cluster, an [Fe_8S_9C] cluster that is a structural analogue and biosynthetic precursor to FeMo-co.[4] The first part of this chapter discusses adapting this procedure to FeMo-co.

2.2. The site-selective labeling of the terminal Fe site of FeMo-co

Our approach to incorporating ^{57}Fe into the Fe1 site of FeMo-co entailed (1) using reported protocols[5] for extracting FeMo-co from the MoFe protein of the Mo nitrogenase (NifDK) into *N*-methylformamide (NMF); (2) removing the Fe1 site using a chelator; (3) reconstituting the Fe1 site with ^{57}Fe; and (4) reinserting the labeled cofactor into apo-NifDK[6], a precursor to NifDK that contains the P-cluster but not FeMo-co (see Experimental and methods for details) (Fig. 2.2). Steps (2) and (3) were studied using EPR spectroscopy (Fig. 2.3). When FeMo-co is poised in the M^N state (obtained by incubation with sodium dithionite (DTH)), isolated FeMo-co exhibits a broadened $S = {}^3/_2$

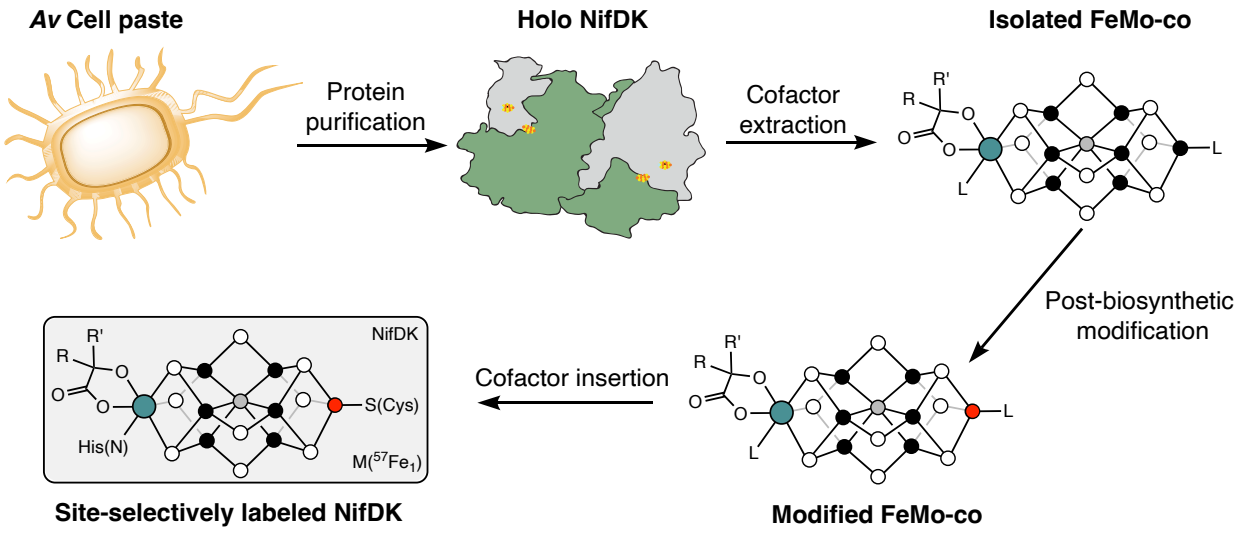

Figure 2.2. Representative scheme for the generation of site-selectively labeled NifDK. The red, black, teal, white and grey circles represent ^{57}Fe, Fe, Mo, S and C atoms, respectively. R,-$CH_2CO_2^-$; R′, -$(CH2)_2CO_2$.

signal that sharpens in the presence of thiophenol (Fig. 2.3).[7] Previous work demonstrated that treating isolated FeMo-co with ethylenediaminetetraacetate (EDTA) or *o*-phenanthroline eliminates this signal, a process that can be reversed upon incubation of Zn^{2+} or Fe^{2+}, respectively;[8] similarly, addition of $^{57}Fe^{2+}$ (35 equiv) to EDTA-treated FeMo-co (30 equiv of EDTA) recovers the EPR signal. Based on the findings with the L-cluster,[4] we hypothesized that this protocol resulting in site-selective ^{57}Fe incorporation into the Fe1 site.

Encouraged by these results, three NifDK samples were prepared with ^{57}Fe in either: (1) the Fe1 site (NifDK–M($^{57}Fe_1$); (2) the belt sites (Fe2-Fe7, (NifDK–M($^{57}Fe_6$)); and (3) in all seven sites (Fe1-Fe7, (NifDK–M($^{57}Fe_7$)). The NifDK–M($^{57}Fe_7$) sample was generated by isolating FeMo-co (M($^{57}Fe_7$)) from fully ^{57}Fe-labeled NifDK, incubating the cofactor with the crude lysate from DJ1143 cells (an *Azotobacter vinelandii* strain that

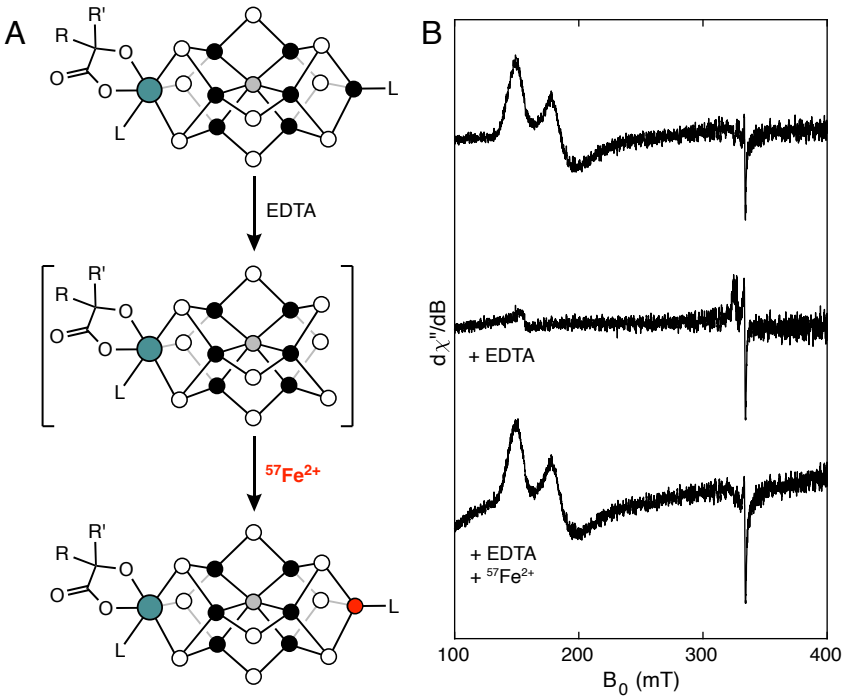

Figure 2.3. Postbiosynthetic incorporation of ^{57}Fe into FeMo-co. **A,** The chemical interconversions of isolated FeMo-co. **B,** Corresponding EPR spectra recorded at 9.37 GHz, 5 K, and 1 mW. All EPR samples have been incubated with DTH (2 mM) and PhSH (2 mM). The red, black, teal, white and grey circles represent ^{57}Fe, Fe, Mo, S and C atoms, respectively. R,-$CH_2CO_2^-$; R′, -$(CH2)_2CO_2$.

produces His-tagged apo-NifDK), and purifying the resulting holo-NifDK–M($^{57}Fe_7$) (Fig. 2.4A). The corresponding Mössbauer spectrum of NifDK–M($^{57}Fe_7$) in the M^N state is consistent with previous reports[2, 7, 9-10] and appears as a quadrupole doublet with an average isomer shift (δ_{avg}) of 0.39 mm s^{-1}, reflecting the overlapping signals from the seven Fe sites (*vide infra*).

We subsequently generated the site-selectively labeled samples: NifDK–M($^{57}Fe_6$), from treating fully ^{57}Fe-labeled FeMo-co with EDTA followed by natural-abundance Fe^{2+}, and NifDK–M($^{57}Fe_1$), from treating natural-abundance FeMo-co with EDTA followed by $^{57}Fe^{2+}$ (Fig. 2.4A). These samples, as well as NifDK–M($^{57}Fe_7$), show full C_2H_2 reduction activity (Table S2.12) and cleanly exhibit the $S = {}^3/_2$ EPR signal of native Mo-nitrogenase resting state (Fig. 2.4B), demonstrating that our postbiosynthetic EDTA/Fe^{2+} treatment affects neither FeMo-co's structure, composition, nor competency for reinsertion into apo-NifDK to generate active, holo-NifDK. ICP-MS analysis of the

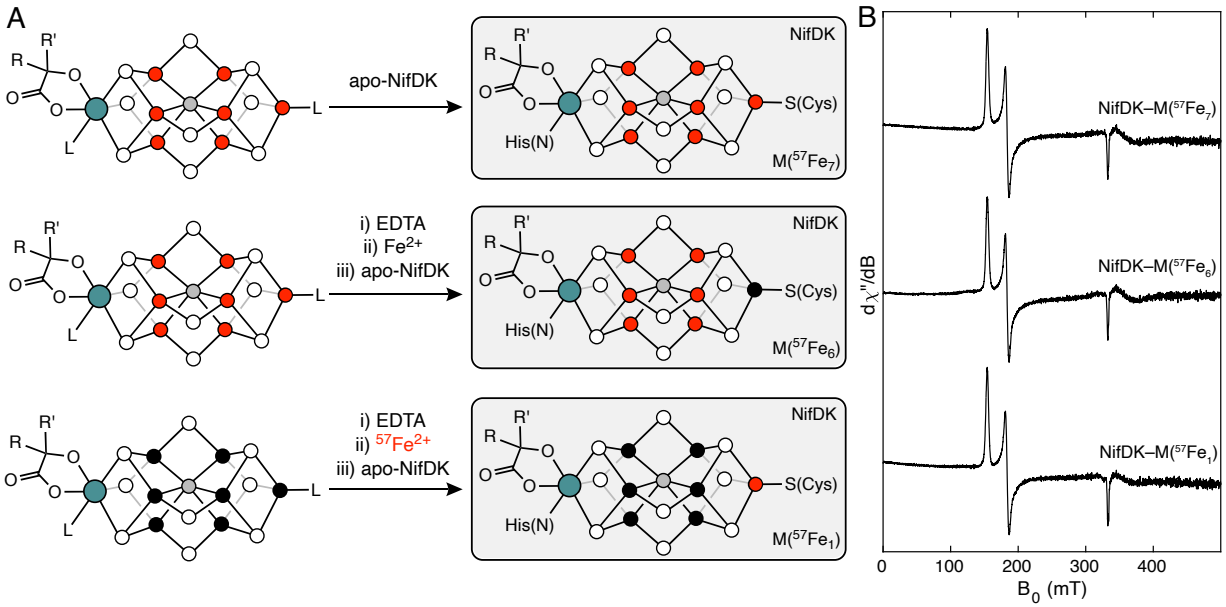

Figure 2.4. Preparation of site-selectively labeled holo-NifDK samples. A, Preparation of the NifDK isotopologues: NifDK–M($^{57}Fe_7$), NifDK–M($^{57}Fe_6$), and NifDK–M($^{57}Fe_1$). **B,** EPR spectra of the respective samples recorded at 9.37 GHz, at 5 K and 1 mW. The red, black, teal, white and grey circles represent ^{57}Fe, Fe, Mo, S and C atoms, respectively. R,-$CH_2CO_2^-$; R′, -$(CH2)_2CO_2$.

$^{56/57}$Fe content of the NifDK–M(^{57}Fe$_1$) sample indicates nearly quantitative labeling efficiency (~90% assuming complete site-selectivity for the Fe1 site; see supplementary information, section 2.7.1 for further discussion). We note that generation of different NifDK–M(^{57}Fe$_1$) samples results in essentially identical EPR and Mössbauer spectra (Fig S2.1), demonstrating the high degree of reproducibility of this procedure. As discussed next, the essentially quantitative site-selectivity of ^{57}Fe labeling is evident in both the Mössbauer and ENDOR spectra of these samples when poised in the M^N state (*vide infra*).

2.3. ENDOR spectroscopic analysis of the NifDK isotopologues

The Q-band ^{57}Fe ENDOR spectra of the three nitrogenase isotopologues in the M^N state recorded at g_3 are displayed in Fig. 2.5. The spectrum of NifDK–M(^{57}Fe$_7$) displays partially resolved signals that are consistent with the predicted [ν_-, ν_+] doublets

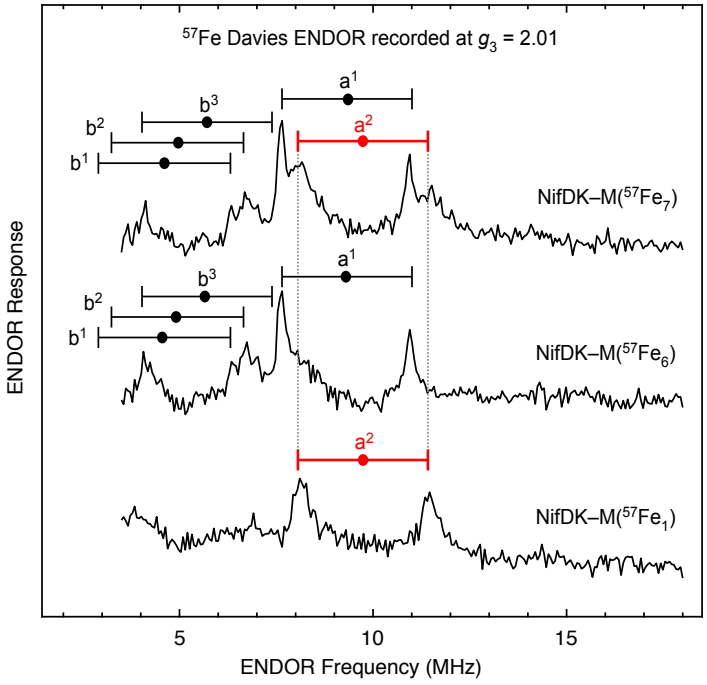

Figure 2.5. ^{57}Fe Davies ENDOR spectra of the site-selectively labeled holo NifDK samples. Recorded at g_3 = 2.01 (1235 mT), 34.745 GHz, and T = 2 K, with t(π/2) = 40 ns, τ = 600 ns, T_{RF} = 40 µs, and repetition time = 15 ms. 'Goalposts' link the [ν_-, ν_+] doublets from individual ^{57}Fe sites, as predicted from hyperfine tensors previously reported[10-11] (see text).

from five ^{57}Fe sites, each centered at half the hyperfine coupling (A/2) determined from the previous analysis of X-band ENDOR spectra, and each split by twice the ^{57}Fe Larmor frequency (3.4 MHz at 1235 mT).[11-12] Note that due to the magnitude of the zero-field splitting of FeMo-co in NifDK, its EPR spectrum at low temperature (less than 5 K) can be described in terms of a 'fictious spin', S= $^1/_2$, *with* $\boldsymbol{g}$ = [g_1, g_2, g_3] = [4.32, 3.62, 2.01].[10-11] The corresponding NifDK–M(^{57}Fe$_6$) sample, in which only Fe2–Fe7 are enriched with ^{57}Fe, retains four of the five doublets, and lacks the doubleted denoted as a^2, indicating that this doublet must arise from the Fe1 site. The assignment of this signal to Fe1 is corroborated by the spectrum of the NifDK–M(^{57}Fe$_1$), which strikingly only shows a single doublet which is consistent with the a^2 doublet centered at the expected frequency, A/2 = 9.8 MHz. The complete absence of the ν_+ peak of the a^2 doublet in the NifDK–M(^{57}Fe$_6$) spectrum indicates the high labeling efficiency of the Fe1 site with natural abundance Fe, while the observation of only the a^2 doublet in the NifDK–M(^{57}Fe$_1$) spectrum, and in particular the absence of any intensity associated from either peak of the shape and intense a^1 doublet, establishes the high selectivity of the site-selective protocol for FeMo-co.

In the original X-band study, the ^{57}Fe ENDOR spectra were well-resolved at the low fields between g_1 = 4.32 and g_2 = 3.62 and at the high-field edge of the EPR spectrum, g_3 = 2.01, but poor resolution between g_2 and g_3 prevented direct experimental correlation between the responses from individual sites at the two 'ends' of the EPR spectrum. This 'gap' was addressed with ENDOR simulations, which indicated that the low-field A^2 signal evolved into the high-field a^2 doublet.[11] The present work confirms this correspondence between the A^2 and a^2 signals as well as the hyperfine tensor derived from the analysis of the field-dependence of the X-band ENDOR signals. The Q-band ENDOR spectra of the selectively labeled NifDK–M(^{57}Fe$_1$) sample recorded at g_3 = 2.01 and g_1 = 4.30 display features centered at ~10 and ~16 MHz, respectively (Fig. 2.6), which are reproduced using the hyperfine tensor and associated Euler angles for a single ^{57}Fe site derived from the prior ENDOR simulations: hyperfine tensor principal components written in terms of the true S = $^3/_2$ spin, $^T\boldsymbol{A}$ = [$^TA_1$, $^TA_2$, $^TA_3$] = [–14.0, –18.3, –19.5] MHz ($^TA_3$ increased by 3%) and the reported Euler angles α = 10, β

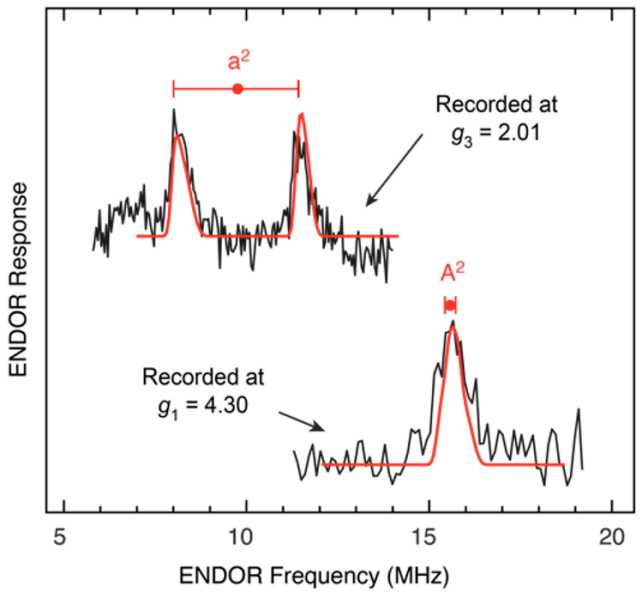

Figure 2.6. ^{57}Fe Davies ENDOR spectra of the NifDK–M(^{57}Fe$_1$) sample recorded at g_3 = 2.01 (top; reproduced from Fig. 2.5) and g_1 = 4.30 (bottom). Center of each 'goalpost' equals the observed $A/2$ at that single-crystal-like g-value; breadth of each goalpost equals twice the effective nuclear Larmor frequency. At g_1 the hyperfine coupling is strongly modified by the influence of the zero-field splitting of the true-spin $S = {}^3/_2$ resting-state FeMo-cofactor (see section 2.7.2) and the *observed* Larmor splitting of the doublet at g_1 is less than predicted for an isolated ^{57}Fe site. The significance of the latter is discussed in the text. Simulations (red) carried out as before[22] employ parameters given in the text; experimental parameters are the same as in Fig. 2.5.

= 15, γ = 0 (modified from Yoo *et al.*,[2] Fig. S2.2) defining the orientation of the hyperfine-tensor frame relative to the g-tensor frame (see supplementary information, section 2.7.2).[11] Notably, the finding that the *observed* Larmor splitting of the ^{57}Fe1 doublet at g_1 is 'nulled,' such that a single peak is observed rather than a well-resolved doublet as seen at g_3 (Fig. 2.6), directly reveals the Fe1 hyperfine coupling sign to be negative. The negative sign and the magnitude of the isotropic coupling for $^{T}\boldsymbol{A}$ of the Fe1 site, $^{T}a_{iso}$ = -17.3 MHz, together correspond to a vector-coupling coefficient for the spin of Fe1 of $K_1 \approx 0.87$, where $K_1 = 1$ implies that the Fe1 spin is exactly parallel to the cluster spin and $K_1 = 0$ implies that it is orthogonal. Thus, the spin of Fe1 is essentially collinear with the overall electron spin of the cluster.[13] This determination of the $\boldsymbol{A}$(^{57}Fe) hyperfine tensor corresponding to the Fe1 site, and thus the value of K_1, is critical for limiting the simulation space for Mössbauer experiments, delineating between the

myriad broken-symmetry configurations for FeMo-co in the M^N state, and interpreting other properties of FeMo-co, as discussed below.

2.4. Mössbauer spectroscopic analysis of M^N

The 80 K Mössbauer spectra of the three NifDK isotopologues are shown in Fig. 2.7 (see supplementary information for details on Mössbauer data collection and analysis). As expected, the NifDK–M($^{57}Fe_7$) and NifDK–M($^{57}Fe_6$) spectra are very similar, each appearing as a single broad quadrupole doublet centered at δ_{avg} = 0.39 and 0.38 mm s^{-1}, respectively, corresponding to the overlapping quadrupole doublets of all seven sites and the six belt sites, respectively. In contrast, the 80 K Mössbauer spectrum of the NifDK–M($^{57}Fe_1$) features a quadrupole doublet centered at an isomer shift, δ_{avg} = 0.49 mm s^{-1}, that is considerably higher than that of the NifDK–M($^{57}Fe_7$) and NifDK–M($^{57}Fe_6$) spectra. That the NifDK–M($^{57}Fe_1$) spectra differs from the other isotopologues

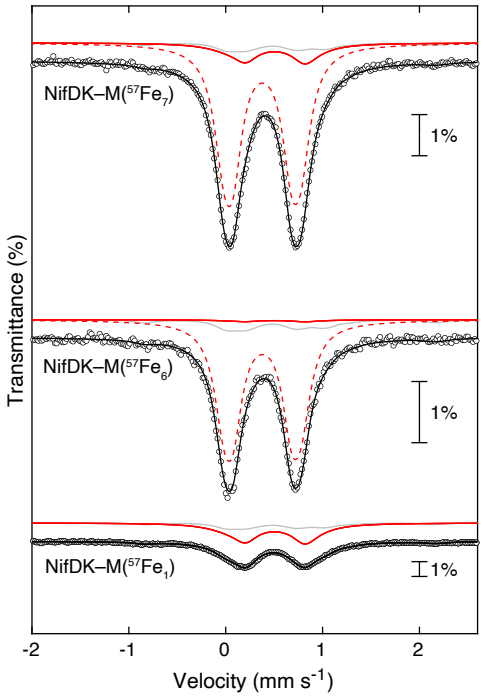

Figure 2.7. 80 K Mössbauer spectra of the NifDK isotopologues. Circles are the experimental data; black traces are the total simulations; solid red traces are simulations of the Fe1 site when labeled with ^{57}Fe; dashed red traces are simulations of the belt Fe sites when labeled with ^{57}Fe; gray traces are contributions from natural-abundance ^{57}Fe; see the SI for details on data workup and simulation. Note that a minor high-spin Fe^{2+} site has been subtracted from the NifDK–M($^{57}Fe_1$) spectrum.

further supports the site-selectivity of the labeling protocol described above. Simulations of the NifDK–M($^{57}Fe_7$), –M($^{57}Fe_6$), and –M($^{57}Fe_1$) spectra provide the 80 K Mössbauer parameters in Table 2.1 (see SI for further details). Notably, the signal arising from the Fe1 site in NifDK–M($^{57}Fe_1$) is relatively broad even at high temperatures, and its lineshape exhibits an unusual temperature dependence (Fig S2.3 and S2.4). As discussed in the Supplementary Information, such behavior could be ascribed to the thermal population and interconversion of low-lying excited states, although further analysis would be required to test this and alternative hypotheses.

Table 2.1. The weighted average 80 K Mössbauer parameters for the M($^{57}Fe_7$), belt, and Fe1 sites in the M^N state.

	M($^{57}Fe_7$)	Belt[a]	Fe1
δ (mm s^{-1})	0.39	0.38	0.49
$\lvert\Delta E_Q\rvert$ (mm s^{-1})	0.70	0.70	0.71

[a]See Supporting Information for details on the simulation of the belt Fe sites of FeMo-co.

The ENDOR data provide $\boldsymbol{A}$(^{57}Fe) for the Fe1 site and unequivocally prove that the Fe1 site corresponds to the spectroscopic A^2 site, however the Mössbauer hyperfine parameters for the A^2 site gleaned from analysis of low-temperature (4.2 K) studies on fully labeled samples[2] cannot be directly compared to our 80 K Mössbauer studies (*vide supra)*. We therefore acquired and analyzed Mössbauer spectra at low temperature (4.7 K) in the presence of an external weak magnetic field (77 mT) (Fig. 2.8). Using the $\boldsymbol{A}$(^{57}Fe1) hyperfine coupling tensor determined by ^{57}Fe ENDOR spectroscopy and taking into account the background signals associated with the natural-abundance ^{57}Fe present in the P-cluster and Fe1–Fe7 sites of FeMo-co (gray traces, Fig. 2.8; see SI for further discussion), we simulated the signal arising from the Fe1 site (Table 2.2), and thereby obtained its low-temperature Mössbauer hyperfine parameters: δ = 0.54 mm s^{-1} and $\lvert\Delta E_Q\rvert$ = 1.32 mm s^{-1}. Notably, the value of δ and the magnitude of ΔE_Q for the Fe1 site obtained from the site-selectively labeled NifDK–M($^{57}Fe_1$) sample are higher than those proposed by Yoo *et al.* for any Fe site, including the A^2 site (respectively 0.48 and –0.94 mm s^{-1} at 4.2 K), based on simulations of NifDK–M($^{57}Fe_7$).[2] This suggests that

the Fe1 site has somewhat more electron density—and, correspondingly, that the six belt Fe sites have somewhat less—than indicated by previous Mössbauer analyses. The implications of this observation are discussed next.

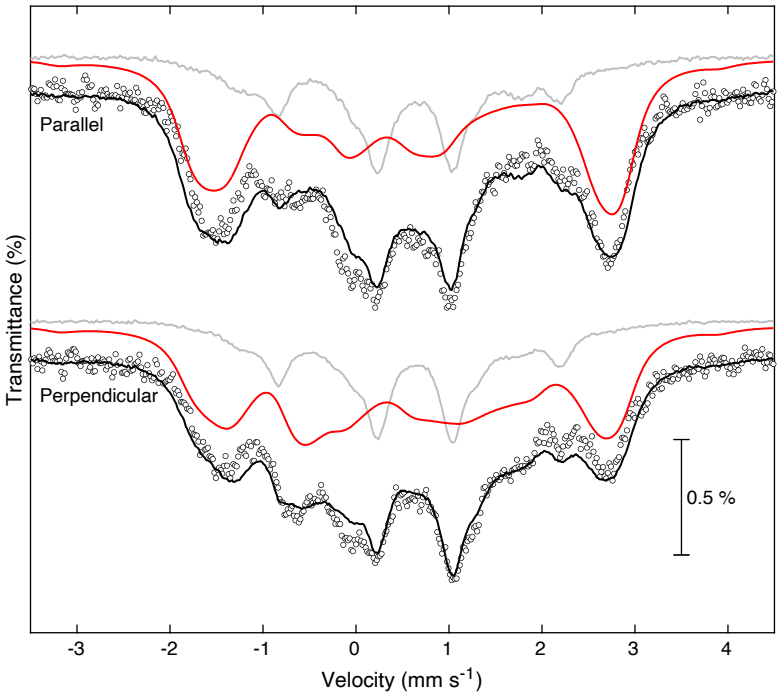

Figure 2.8. Analysis of the Mössbauer hyperfine parameters for the Fe1 site. Mössbauer spectra of the NifDK–M($^{57}Fe_1$) sample recorded at 4.7 K in the presence of a 77 mT external field oriented parallel (top) or perpendicular (bottom) to the incident radiation. Circles are the experimental data; black traces are the total simulations; red traces are the simulations for the Fe1 site; gray traces are contributions from natural-abundance ^{57}Fe. Note that a minor high-spin Fe^{2+} site has been subtracted from the NifDK–M($^{57}Fe_1$) spectrum.

Table 2.2. Mössbauer parameters for the simulation of the NifDK–M($^{57}Fe_1$) data at 4.7 K in the presence of a 77 mT external magnetic field.

	Fe1	Fe^{2+}
δ (mm s^{-1})	0.54	1.4
ΔE_Q (mm s^{-1})	1.32	3.15
Γ (mm s^{-1})	0.39	0.31
Rel. Area (%)	73	4
η	0.73	-
α_{efg}	88	-
β_{efg}	110	-
γ_{efg}	49	-
A_x (MHz)	-18.3	-
A_y (MHz)	-14	-
A_z (MHz)	-19.5	-
α_A	10	-
β_A	15	-
γ_A	0	-

2.5. Interpretation of the spectroscopic parameters of the Fe1 site in M^N

Fe–S clusters have been extensively characterized by Mössbauer spectroscopy,[1] and thiolate-ligated [Fe_4S_4] clusters are particularly useful reference compounds for this study because they have an identical primary coordination sphere to that of the Fe1 site of FeMo-co: three μ_3-sulfides and one Cys-thiolate. For [Fe_4S_4] clusters, FeMo-co, and other high-nuclearity Fe–S clusters, the Fe oxidation states are typically assigned as Fe^{2+}, Fe^{3+}, and/or $Fe^{2.5+}$; the latter corresponds to an Fe in a mixed-valent Fe^{2+}–Fe^{3+} pair in which the excess electron is delocalized via the double-exchange mechanism.[14-15] Based on comparisons to [Fe_4S_4] clusters,[1] the δ and $|\Delta E_Q|$ at 4.7 K for the Fe1 site are both too low for an Fe^{2+} and too high for an Fe^{3+} site (Table S2.13). Indeed, the δ of the Fe1 site, 0.54 mm s^{-1}, and the $|\Delta E_Q|$, 1.4 mm s−1, compare favorably with that of the $Fe^{2.5+}$ sites in $[Fe_4S_4]^+$ clusters (~0.5 and ~1.3 mm s^{-1}, respectively).[1] Furthermore,

using an empirical relationship[16] that relates the formal oxidation state and the Mössbauer isomer shifts of tetrahedral Fe sites in synthetic $FeS_n(SR)_{4-n}$ compounds, we arrive at an oxidation state of $Fe^{2.4+}$ for the Fe1 site in M^N. The assignment of an $Fe^{2.5+}$ valence is further supported by comparison to the M^{OX} state (*vide infra*), and is broadly consistent with spatially resolved anomalous dispersion (SpReAD)[3] and computational[17-18] analyses that indicate the Fe1 site is relatively reduced.

Note that the previous SpReAD analysis[3] of FeMo-co suggested that the electronic structure of FeMo-co was highly localized, including that the Fe1 site assigned as an isolated Fe^{2+} site. The data presented here supports a more delocalized picture of FeMo-co, as the identification of an $Fe^{2.5+}$ oxidation state for the Fe1 site necessitates that one of its neighbors—Fe2, Fe3, or Fe4 (Fig. 2.9)—be the other member of the mixed-valent pair. This Fe site must be spin-aligned with Fe1 to undergo electron delocalization via the double exchange mechanism, and it therefore must be one of the remaining *A* sites, which are each thought to have an $\delta \sim 0.4$ mm s^{-1}.[2] The relatively high δ for Fe1 indicates that, on the whole, the covalency of its Fe–ligand interactions (featuring bonds to three μ_3-sulfides and one Cys-thiolate) is somewhat lower than that of its double-exchange-coupled partner (featuring bonds to two μ_3-sulfides, one μ_2-sulfide, and one μ_6-carbide). This difference can be attributed at least in part to the greater Fe–S covalency involving μ_2-sulfides compared with μ_3-sulfides and thiolates[19] and may also arise from covalent Fe–C bonding. Additionally, the difference in coordination environments of the Fe sites could result in greater localization of the itinerant electron at the Fe1 site, and this effect would likewise contribute to a higher δ for Fe1.

The insights from spectroscopic analysis of the site-selectively labeled samples—in particular, that the spin of the Fe1 site is essentially coaligned with the overall electron spin of the cluster, and that the Fe1 site is part of a mixed-valent pair of $Fe^{2.5+}$ centers—impose new experimental constrains on the electronic structure of FeMo-co in the M^N state. All electronic configurations that invoke antiparallel spin alignment between the Fe1 site and the total spin can be rejected; in Noodleman's nomenclature,[20-21] this includes the BS3, BS6, BS9, and BS10 family of electronic

structures. Our results also require that at least one of the neighboring belt Fe sites (Fe2, Fe3, and Fe4) be coaligned with Fe1 in order to engage in electron sharing via the double-exchange mechanism; this further eliminates the BS2 family of electronic structures. Overall, these experimental findings are consistent with the electronic-structure picture favored in recent computational analyses:[17-18] an $[MoFe_7S_9C]^{-}$ core charge state in the BS7 configuration, particularly the three spin isomers BS7-235, BS7-247, and BS7-346, which differ in the identity of the belt Fe that is aligned with the Fe1 site (Fig. 2.9). In turn, the determination of the vector-coupling coefficient for ^{57}Fe1 plays an important role in assigning the function of the central FeMo-cofactor carbon.[22-23]

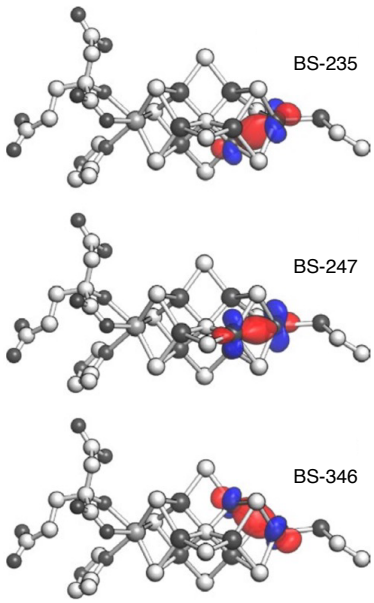

Figure 2.9. Isosurface plots (0.05 a.u.) of the localized orbital qualitatively depicting the double-exchange interaction between the Fe1 site and its three neighboring Fe sites. The plots were generated in the manner of Benediktsson and Bjornnson[17] (see the supplementary information, section 2.7.6, for further details).

2.6. Conclusions

The work above demonstrates a chemical method for site-selective incorporation of ^{57}Fe into FeMo-co and shows how analysis of such samples in the M^N state of FeMo-co informs on the distribution and coupling of FeMo-co's valence electrons. The ^{57}Fe ENDOR spectroscopic analysis of M^N links the crystallographic Fe1 site to the

spectroscopic A^2 site, and thereby experimentally connects the electronic properties of an individual site and the geometric structure of FeMo-co. Through Mössbauer analysis, it was determined that the Fe1 site is part of a mixed-valent pair of $Fe^{2.5+}$ ions, which necessitates that Fe2, Fe3, or Fe4 be its double exchange partner. Overall, these findings place new experimental constrains on the electronic structure of FeMo-co. Expanding this methodology to states beyond M^N are discussed in the next chapter.

2.7. Supplementary Information

2.7.1. Determination of the incorporation probability using ICP-MS

Analysis of the Mössbauer spectra NifDK–M($^{57}Fe_1$) samples requires several parameters (see below), one of which is the probability of incorporating ^{57}Fe into the Fe1 site (p_{Fe1}). We calculate p_{Fe1} using the equations below following a method reported previously for the L-cluster.[4]

$$R = \frac{14c_1 + p_{Fe_1}c_2 + (1 - p_{Fe_1})c_1}{14c_3 + p_{Fe_1}c_4 + (1 - p_{Fe_1})c_3} \quad (1)$$

or

$$p_{Fe_1} = \frac{15(c_1 - Rc_3)}{(Rc_4 - Rc_3 + c_1 - c_2)} \quad (2)$$

where

R = the measured ^{56}Fe/^{57}Fe ratio,

c_1 = the natural abundance of ^{56}Fe (91.7 %),

c_2 = the abundance of ^{56}Fe in the ^{57}Fe source (3.6%),

c_3 = the natural abundance of ^{57}Fe (2.12%), and

c_4 = the abundance of ^{57}Fe in the ^{57}Fe source (95.5%).

Additional discussion: Eq. (2) holds under the assumptions that (i) there are equimolar amounts of P-cluster and FeMo-co; (ii) there is 100% site selectivity for incorporating an exogenous Fe atom into the Fe1 site; (iii) samples have no mononuclear Fe contaminants. The first assumption is supported by the high activity of the reinserted samples. The second assumption is supported by the ENDOR measurements on the NifDK–M($^{57}Fe_6$) sample (see Fig. 2.5 in the main text), which show full elimination of the A^2 doublet, consistent with high labeling efficiency (see main text). The weakest assumption is (iii) because we observed in most samples a small amount (~5%) of mononuclear Fe, which may arise from occupancy at the "sixteenth" Fe site, the His tag, and/or elsewhere. (In cases where mononuclear Fe is observed, it is subtracted from the measured Fe content before calculating p_{Fe1}). Despite these assumptions, we routinely observe ~80% labeling efficiency for the Fe1 site and, most importantly, essentially identical Mössbauer spectra for different NifDK–($^{57}Fe_1$) samples (Fig. S2.2),

indicating a consistent and high degree of ^{57}Fe labeling. For the simulation of the NifDK–M(^{57}Fe$_1$) Mössbauer spectra (described further below), we note that although we fix p_{Fe_1} as calculated using eq. (2), p_{Fe_1} can be varied rather substantially (ca. ±20%) with little effect on the simulated isomer shift and quadrupole splitting.

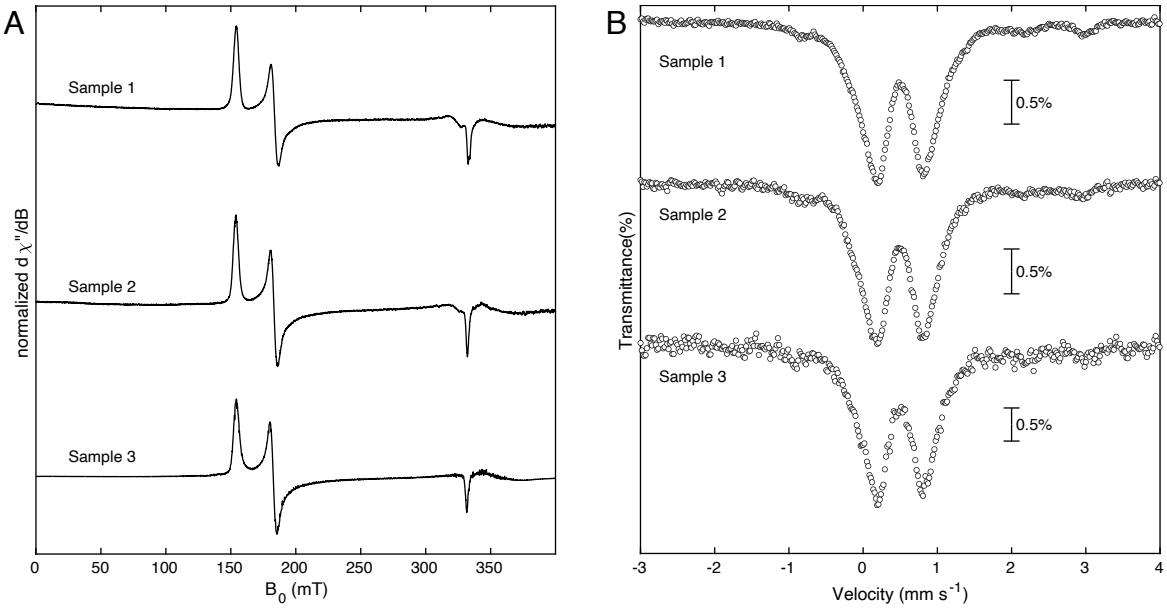

Figure S2.1. M^N Mössbauer and EPR spectra of the NifDK–M(^{57}Fe$_1$) samples used. A) Normalized EPR spectra of the three samples of NifDK–M(^{57}Fe$_1$) in the M^N state; acquired at 9.37 GHz, 5 K, and 1 mW. B) Zero-field Mössbauer spectra the three samples of NifDK–M(^{57}Fe$_1$) recorded at 80 K. Circles are the normalized experimental data.

2.7.2. Analysis of the NifDK ^{57}Fe ENDOR data

FeMo-co when poised in the M^N state has a true electron spin, $S = {}^3/_2$. As a result of its large and somewhat rhombic zero-field splitting, its low-temperature EPR spectrum arises solely from the lower Kramers doublet and is commonly discussed in terms of a fictitious spin, $S' = {}^1/_2$, with the effective g-tensor $\boldsymbol{g} = [g_1, g_2, g_3] = [4.32, 3.62, 2.01]$.[11, 24] The analysis of the ^{57}Fe ENDOR spectra of NifDK–M($^{57}Fe_1$) highlights the importance of selective ^{57}Fe labeling in ENDOR measurements carried out with the higher resolving power of Q-band pulsed ^{57}Fe ENDOR. The three ^{57}Fe tensor elements, $\boldsymbol{A} = [A_1, A_2, A_3]$ referenced to the fictitious spin originally reported[11] were directly obtained by simulation of the 2D pattern of ENDOR spectra collected across the EPR envelope, as described in terms of the fictitious spin. They are related to those for the E_0 true spin $S = {}^3/_2$, $^T\boldsymbol{A} = [{}^TA_1, {}^TA_2, {}^TA_3]$, as listed in the main text, by the relationship, $\boldsymbol{A} = [A_1, A_2, A_3] = [(g_1/g_e)\,{}^TA_1, (g_2/g_e)\,{}^TA_2, {}^TA_3]$.[11] The parameters describing $^T\boldsymbol{A}$ for Fe1 as seen in the present work include a slight revision to the value of $A_3 = {}^TA_3$ given in the original X-band CW ENDOR paper,[11] but the original values of ${}^TA_1$ and ${}^TA_2$, as well as the originally defined relative orientation of the $^T\boldsymbol{A}$ tensors with respect to the fictitious-spin g-tensor axis frame,[11] as described in terms of the Euler angles originally determined by ENDOR.[11]

The importance of using the correct Euler angles and hyperfine tensor components, rather than the apparently similar values adopted in the Mössbauer paper by Yoo *et al.*,[2] is firstly shown in Fig. S2.1, through the accuracy of the simulation of the ^{57}Fe1 signals at g_1 with the original angles, contrasted with the deviation of the simulation with the modified values. Simulations of the full 2D pattern of ^{57}Fe1 spectra (not shown) further show the importance of retaining the initially reported values of ${}^TA_1$, ${}^TA_2$, without modification. The importance of the slight modification to ${}^TA_3$ introduced here (~3%) is shown in the simulation at g_3 (Fig. S2.2).

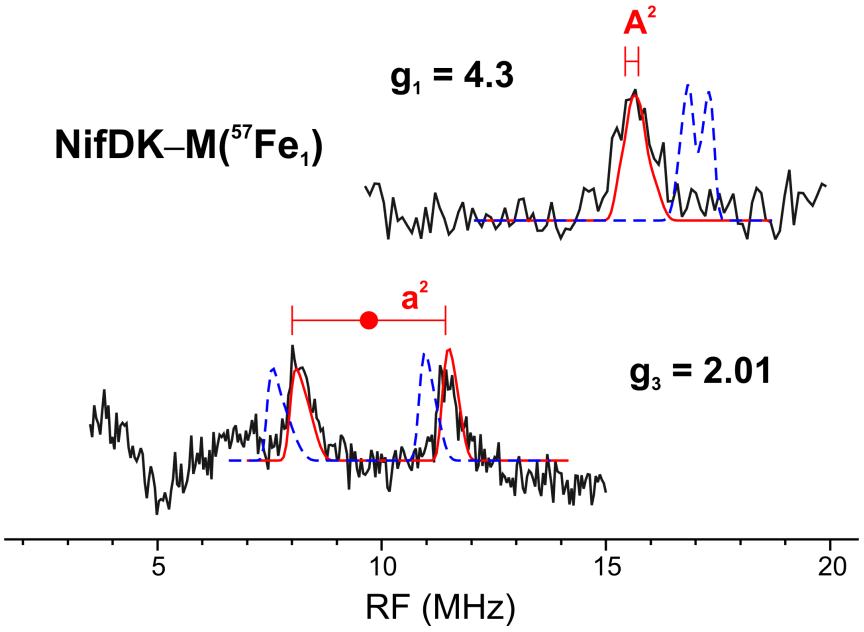

Figure S2.2. 35 GHz Davies ENDOR spectra of the NifDK–M(^{57}Fe$_1$) with parameters from Yoo *et al.* Sample taken at the g_1 and g_3 edges of EPR spectrum and their simulations obtained with parameters derived from X-band CW ENDOR spectroscopy (red solid, g = [4.32, 3.62, 2.01], ***A*** = [-14, -18.3, -19.5] MHz, Euler angles α = 10, β = 15, γ = 0) and with parameters derived from Yoo *et al.* (blue dashed, A = [-15.1, -17.3, -19] MHz, α = 13, β = 22, γ = 0). *Conditions:* as in Fig. 2.5 in the main text.

2.7.3. Estimation of ^{57}Fe enrichment of the NifDK–M($^{57}Fe_7$) and NifDK–M($^{57}Fe_6$) samples

Another parameter necessary for the Mössbauer analysis is R_{label}, which is the fractional enrichment of the ^{57}Fe in an enriched site. While the source we use has an R_{label} = 0.955, we observed deviations from this in our NifDK–M($^{57}Fe_7$) and NifDK–M($^{57}Fe_6$) samples, which could be a result of some natural abundance Fe contamination introduced during cell growth of DJ1141. To estimate the ^{57}Fe enrichment of each sample we used the following equation

$$R_{label} = \frac{^{57}Fe_{total} - (^{57}Fe_P)}{M \cdot N_{sites}} \quad (3)$$

where $^{57}Fe_{total}$ is the total concentration of ^{57}Fe in the sample, $^{57}Fe_P$ is the total concentration of ^{57}Fe from natural-abundance ^{57}Fe originating from the P-cluster, M is the total concentration of FeMo-co, and N_{sites} is the ideal number of FeMo-co sites that are enriched with ^{57}Fe in the respective sample. Under the assumption that we have a ratio of 1:1:1 P-cluster to FeMoco to αß heterodimer, and that there are 15 Fe sites per αß heterodimer, we can rewrite the equation as[25,26]

$$R_{label} = \frac{^{57}Fe_{total} - (8 \cdot Mo \cdot R_{NA})}{Mo \cdot N_{sites}} \quad (4)$$

Note: For the NifDK–M($^{57}Fe_1$) sample, R_{label} is 0.955 as the ^{57}Fe source was added *in vitro*, and therefore its value should not be perturbed.

2.7.4. Analysis of the E_0 Mössbauer data

General considerations

The simulations of all Mössbauer spectra were performed similarly to what was previously reported.[4] Each spectrum consists of several quadrupole doublets with each quadrupole doublet described as a sum of two Lorentzian functions:

$$L(x) = -\frac{A}{\pi}\left(\frac{\frac{\Gamma}{2}}{\left(x-\left(\delta+\frac{\Delta E_Q}{2}\right)\right)^2+\left(\frac{\Gamma}{2}\right)^2}+\frac{\frac{\Gamma}{2}}{\left(x-\left(\delta-\frac{\Delta E_Q}{2}\right)\right)^2+\left(\frac{\Gamma}{2}\right)^2}\right) \quad (5)$$

The area factor for each quadrupole doublet was described as

$$A = a \cdot r \cdot n \quad (6)$$

where a is a constant correlated to sample concentration, r is the enrichment of ^{57}Fe, and n is the number of Fe nuclei corresponding to a given doublet.

All Mössbauer spectra were simulated using the following steps:

(1) Subtracting the contribution from the natural abundance ^{57}Fe sites by using the corresponding NifDK–P($^{57}Fe_8$)–M($^{57}Fe_7$) spectrum in WMOSS[27] or MATLAB. Below we discuss how we determined the contribution of the 15 Fe sites for each sample.

(2) Simulation of the NifDK–M($^{57}Fe_1$) spectrum to determine the Mössbauer parameters for the Fe1 site.

(3) Simultaneous simulation of the NifDK–M($^{57}Fe_7$) and NifDK–M($^{57}Fe_6$) spectra using the Mössbauer parameters established in the simulation of the Fe1 site to obtain the average Mössbauer parameters for the belt Fe sites of FeMo-co.

All simulations used the following assumptions:

1) A 1:1 ratio of FeMo-co and P-cluster.
2) The probability of labeling the belt Fe sites in our postbiosynthetic treatment is 0. This is consistent with ENDOR data presented in the main text and by analogy to our previous work on the L-cluster.[4]

Simulation of the NifDK–M($^{57}Fe_1$) VT Data in the M^N state

The simulation of the variable-temperature NifDK–M($^{57}Fe_1$) spectra required two quadrupole doublets, as the Mössbauer spectra of the M^N state acquired above 50 K reflects multiple states (as mentioned in the main text and discussed in the next section). The sum of the area factors of these two doublets is equal to A_{Fe1}. It is important to note that the individual Mössbauer parameters for the two quadrupole doublets do not have any physical meaning, and we only discuss the average parameters of the doublets.

The total area contribution for the Fe1 site was described as

$$A_{Fe1} = a \cdot \left([(R_{label} \cdot p_{Fe1}) + \left(R_{NA} \cdot (1 - p_{Fe1})\right)] \cdot 1 - a \cdot R_{NA} \cdot 1 \right) \quad (7)$$

where R_{label} is the mole fraction of ^{57}Fe in all enriched Fe sites (in this case the Fe1 site of FeMo-co), and R_{NA} is the natural abundance of ^{57}Fe.

The total area contribution from the 15 Fe sites that was subtracted from the NifDK–M($^{57}Fe_1$) data sets was described as

$$A_{Fe15} = a \cdot R_{NA} \cdot 15 \quad (8)$$

Using eqs. (7) and (8) we determined the total area the 15 Fe sites contributed for each of the NifDK–M($^{57}Fe_1$) spectra and used following as free variables to simulate the VT data:

1) Isomer shift of quadrupole doublet 1 for the Fe1 site
2) Quadrupole splitting of quadrupole doublet 1 for Fe1 site
3) Linewidth of quadrupole doublet 1 for the Fe1 site
4) Isomer shift of quadrupole doublet 2 for the Fe1 site
5) Quadrupole splitting of quadrupole doublet 2 for Fe1 site
6) Linewidth of quadrupole doublet 2 for the Fe1 site
7) Normalizing coefficient for the area of quadrupole doublet 1 for the Fe1 site
8) Normalizing coefficient for the area of quadrupole doublet 2 for the Fe1 site
9) Area coefficient for the NifDK–M($^{57}Fe_1$) data set

The simulations for the various temperatures are presented in Fig. 2.3 and 2.4. The parameters are in Table S2.1, 2.2, 2.3 and 2.4.

Discussion of the NifDK–M($^{57}Fe_1$) VT Data in the M^N state

During our Mössbauer studies of the NifDK–M($^{57}Fe_1$) sample, we observed an unexpected temperature dependence to its signal. Although the isomer shift for the Fe1 site decreases modestly with increasing temperature, from 0.54 mm s^{-1} at 4.7 K to 0.47 mm s^{-1} at 150 K (a magnitude within the realm of a second-order Doppler shift[28]), the line shape of the signal changes substantially with temperature and is relatively broad even at high temperatures (Fig. S2.3). This temperature response is especially apparent in the average quadrupole splitting, which decreases from 1.32 mm s^{-1} at 4.7 K to 0.86, 0.71, and 0.67 mm s^{-1} at 50, 80, and 150 K, respectively (see Table S2.4). The M^N

Mössbauer signal has been shown to be in the fast-relaxation regime at 20 K and above,[10] and we therefore do not attribute such behavior to magnetic relaxation effects (unless the holo-NifDK samples exist as a mixture of states, some of which have much slower electronic relaxation).

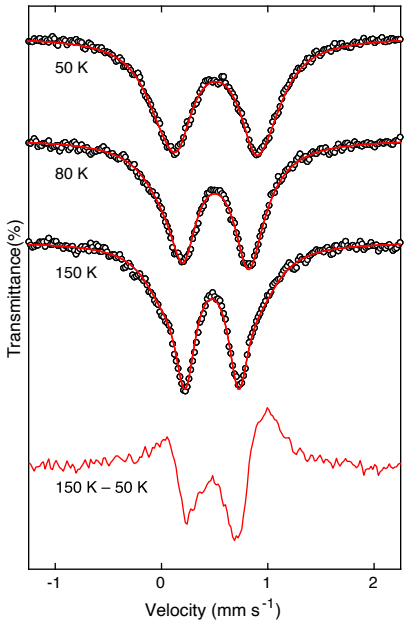

Figure S2.3. Mössbauer spectra (black circles) of the NifDK–M($^{57}Fe_1$) sample recorded at various temperatures. All natural-abundance and high spin Fe^{2+} contributions have been subtracted (see Fig. S2.4 for the raw data). Each spectrum was fit (red traces) to two quadrupole doublets as described in the SI; the overlays of the fits are presented at the bottom, showing the change in spectral shape and breadth as a function of temperature through a difference spectrum of the 150 and 50 K data sets.

The observed temperature dependence could alternatively be ascribed to the thermal population of low-lying excited states with differing quadrupole splitting but essentially invariant isomer shift. Related high-spin, four-coordinate Fe^{2+} complexes have been observed to exhibit a temperature dependence to their quadrupole splitting.[29-31] For these complexes, it has been noted that upon introducing a tetragonal distortion to tetrahedral Fe^{2+}, the degeneracy of the two orbitals of *e* parentage (d_{z^2} and $d_{x^2-y^2}$) is lifted; if the splitting of these orbitals is sufficiently small and the temperature

is sufficiently high, the β-spin electron can occupy either orbital. Because the two electronic configurations have different electric field gradients, the observed quadrupole splitting changes as the population of these states varies with temperature. This phenomenon has also been used to explain the temperature dependence of the quadrupole splitting for $Fe^{2.5+}$ sites in Fe–S clusters in which the delocalized electron occupies the orbitals of *e* parentage.[31] We suggest that the same phenomenon could be occurring at the Fe1 site in M^N.

Additionally, for the Fe1 site in FeMo-co, changing the orientation of the delocalized electron-bearing orbital necessarily changes the identity of its partner spin-aligned Fe site (Fe2, Fe3, or Fe4) with which the electron is delocalized (see Fig. 2.9 in the main text), which in turn could cause a rearrangement of the spins throughout the cofactor. Indeed, multiple spin isomers have been predicted to be nearly isoenergetic in several computational studies (*vide infra)*.[17-18, 20, 32-33] The temperature dependence on the effective quadrupole splitting and its line shape may arise from the thermal population of and interconversion of these spin isomers, as well as other electronic states.

Additional notes: (1) Although we propose that the high-temperature spectra (≥ 50 K) represent several states, we simulate each spectrum as only two quadrupole doublets in arbitrary ratios and with arbitrary linewidths because that is the minimum simulation space required to satisfactorily fit the data. And although the parameters for the individual quadrupole doublets are not physically meaningful, this approach allows for abstraction of the average isomer and quadrupole splitting. The broad and variable linewidths can be attributed to interconversion between states occurring on the Mössbauer timescale. (2) Observing the temperature dependence for the Fe1 site necessitates that this behavior occurs reciprocally in the belt sites (Fig. 2.9). Although we do observe a minor temperature dependence on the aggregate quadrupole splitting of the six belt sites (Fig. S2.5 and Table S2.8), the differences are similar to the experimental noise and we therefore do not offer further interpretation.

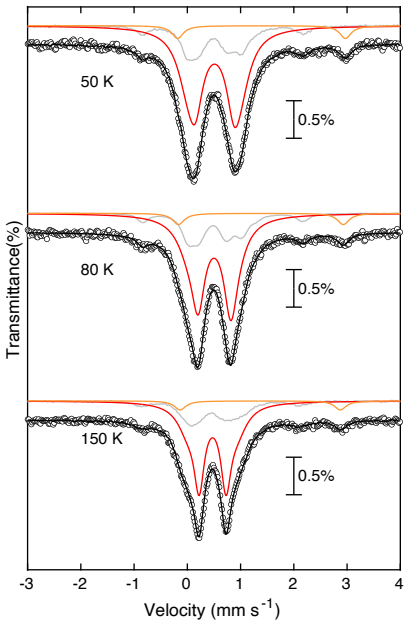

Figure S2.4. Zero-field, variable temperature Mössbauer spectra of the NifDK–M(^{57}Fe$_1$) sample in the M^N state. Top to bottom: 50 K, 80 K, and 150 K. Circles are the experimental data; black traces are the total simulations; red traces are the simulations for the Fe1 site; gray traces are the corresponding NifDK–P(^{57}Fe$_8$)–M(^{57}Fe$_7$) spectra scaled to account for the natural-abundance ^{57}Fe contribution from the 15 Fe sites; orange traces are the simulations for the high spin Fe^{2+} site.

Table S2.1. Mössbauer parameters for the simulation of the NifDK–M(^{57}Fe$_1$) 50 K data shown in Fig. S2.3 and Fig. S2.4.

	Fe1[a]		Fe^{2+}
	Doublet 1	**Doublet 2**	**-**
δ (mm s^{-1})	0.51	0.50	1.38
$\lvert\Delta E_Q\rvert$ (mm s^{-1})	0.72	0.98	3.15
Γ (mm s^{-1})	0.33	0.49	0.26
Rel. Area (%)	31.9	40.4	5.5

[a]The weighted average of the Mössbauer parameters for the Fe1 site are reported in Table S2.4.

Table S2.2. Mössbauer Parameters for the simulation of the NifDK–M($^{57}Fe_1$) 80 K data shown in the main text Fig. 2.7, Fig. S2.3 and S2.4.

	Fe1[a]		Fe^{2+}
	Doublet 1	**Doublet 2**	**-**
δ (mm s^{-1})	0.51	0.46	1.38
$\lvert\Delta E_Q\rvert$ (mm s^{-1})	0.61	0.85	3.10
Γ (mm s^{-1})	0.30	0.54	0.27
Rel. Area (%)	39.5	28.1	5.5

[a]The weighted average of the Mössbauer parameters for the Fe1 site are reported in Table S2.4.

Table S2.3. Mössbauer parameters for the simulation of the NifDK–M($^{57}Fe_1$) 150 K data shown in Fig. S2.3 and S2.4.

	Fe1[a]		Fe^{2+}
	Doublet 1	**Doublet 2**	**-**
δ (mm s^{-1})	0.47	0.47	1.37
$\lvert\Delta E_Q\rvert$ (mm s^{-1})	0.93	0.50	3.01
Γ (mm s^{-1})	0.47	0.23	0.26
Rel. Area (%)	26.6	41.5	5.5

[a]The weighted average of the Mössbauer parameters for the Fe1 site are reported in Table S2.4.

Table S2.4. The weighted average of the isomer shift and quadrupole splitting for the Fe1 site in the M^N state.

	50 K	**80 K**	**150 K**
δ (mm s^{-1})	0.51	0.49	0.47
$\lvert\Delta E_Q\rvert$ (mm s^{-1})	0.86	0.71	0.67

Simultaneous simulation of the NifDK–M($^{57}Fe_7$) and NifDK–M($^{57}Fe_6$) Mössbauer spectra in the M^N state at 80 K

The simultaneous simulation of the NifDK–M($^{57}Fe_7$) and NifDK–M($^{57}Fe_6$) spectra used the following assumptions:

1) All Fe sites in FeMo-co have the same Lamb-Mössbauer factor at 80 K—*i.e.* the area ratio between the belt Fe sites and the Fe1 site in the NifDK–M($^{57}Fe_7$) sample is 6:1.
2) The p_{Fe1} for the NifDK–M($^{57}Fe_6$) sample is identical to that of the NifDK–M($^{57}Fe_1$) sample.

The total area contribution for the belt sites for the NifDK–M($^{57}Fe_7$) data can be described as

$$A_{Fe6} = a \cdot (R_{label} \cdot 6 - R_{NA} \cdot 6) \quad (9)$$

The total area contribution for the Fe1 site was restricted to be one-sixth of A_{Fe6}.

The total area contribution from the 15 Fe sites can be described as

$$A_{Fe15} = a \cdot R_{NA} \cdot 15 \quad (10)$$

For the NifDK–M($^{57}Fe_6$) data, the total area contribution for the belt sites can be described as

$$A_{Fe6} = a \cdot (R_{label} \cdot 6 - R_{NA} \cdot 6) \quad (11)$$

The total area contribution for the Fe1 site can be described as

$$A_{Fe1} = a \cdot ([(1 - p_{Fe1}) \cdot R_{label} + p_{Fe1} \cdot R_{NA}] \cdot 1 - R_{NA} \cdot 1) \quad (12)$$

The total area contribution from the 15 Fe sites can be described as

$$A_{Fe15} = a \cdot R_{NA} \cdot 15 \quad (13)$$

Note that the belt Fe sites were modeled as two symmetric quadrupole doublets and thus their individual Mössbauer parameters have no physical meaning; we therefore focus only on the average parameters of these two doublets to learn about the average properties of the six belt Fe sites of FeMo-co.

With the relative contribution for each set of Fe sites determined and the parameters for the Fe1 site fixed, we carried out the simultaneous simulation of the NifDK–M($^{57}Fe_7$) and NifDK–M($^{57}Fe_6$) setting the following as free variables:

1) Isomer shift of quadrupole doublet 1 for the belt sites

2) Quadrupole splitting of doublet 1 for the belt sites
3) Linewidths of quadrupole doublet 1 for the belt sites
4) Isomer shift of quadrupole doublet 2 for the belt sites
5) Quadrupole splitting of doublet 2 for the belt sites
6) Linewidths of quadrupole doublet 2 for the belt sites
7) Normalizing coefficient for the area of quadrupole doublet 1 for the belt sites
8) Normalizing coefficient for the area of quadrupole doublet 2 for the belt sites
9) Area coefficient for NifDK–M($^{57}Fe_7$) data set
10) Area coefficient for NifDK–M($^{57}Fe_6$) data set

The simulations are presented in the main text (Fig. 2.7) and the parameters are in Table S2.5 and S2.6.

Note: The variable temperature NifDK–M($^{57}Fe_6$) spectra (Fig. S2.5) were not simulated simultaneously with the corresponding NifDK–M($^{57}Fe_7$) data, but rather just as a single data set with the corresponding NifDK–M($^{57}Fe_1$) parameters fixed.

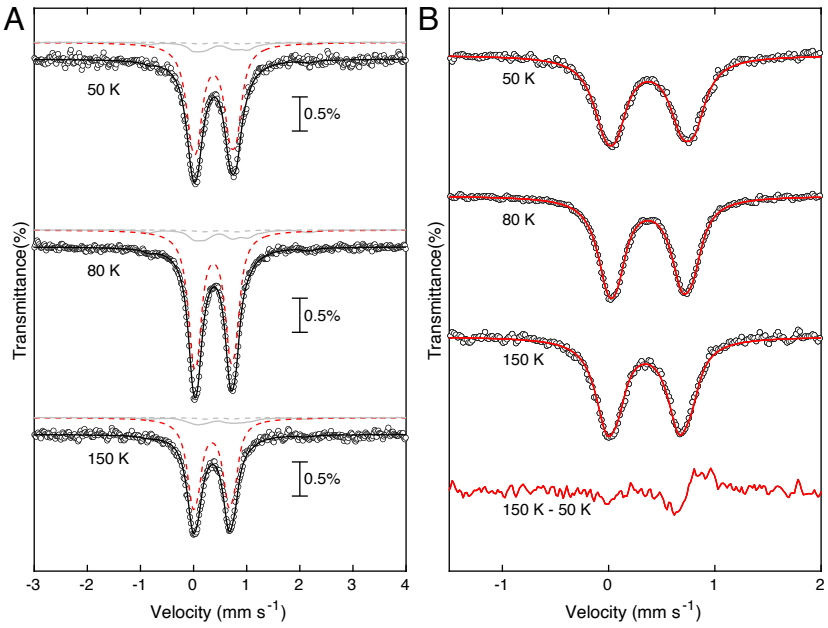

Figure S2.5. Zero-field, variable temperature Mössbauer spectra of the NifDK–M($^{57}Fe_6$) in the M^N state. Top to bottom: 50 K, 80 K, and 150 K. A) The simulation of the variable temperature of the NifDK–M($^{57}Fe_6$) Mössbauer spectra. Circles are the experimental data; black traces are the total simulations; dotted red traces are the simulations for the belt sites; dotted gray traces are the simulations for the Fe1 site enriched with natural abundance ^{57}Fe; gray traces are the corresponding NifDK–P($^{57}Fe_8$)–M($^{57}Fe_7$) spectra scaled to account for the natural-abundance contribution from the 15 Fe sites. B) Mössbauer spectra (black circles) of the NifDK–M($^{57}Fe_6$) sample recorded at various temperatures with all natural-abundance ^{57}Fe contributions subtracted. The difference spectra of the 150 K and 50 K data sets is presented at the bottom.

Table S2.5. The 80 K Mössbauer parameters for the two quadrupole doublets representing the belt Fe sites in the M^N state.

	Doublet 1	Doublet 2
δ (mm s^{-1})	0.38	0.38
$\lvert\Delta E_Q\rvert$ (mm s^{-1})	0.80	0.60
Γ (mm s^{-1})	0.25	0.23
Rel. Area (%)	52.4	47.6

Table S2.6. The 50 K Mössbauer parameters for the two quadrupole doublets representing the belt Fe sites in the M^N state.

	Doublet 1	Doublet 2
δ (mm s^{-1})	0.33	0.45
$\lvert\Delta E_Q\rvert$ (mm s^{-1})	0.72	0.74
Γ (mm s^{-1})	0.29	0.25
Rel. Area (%)	59.7	40.3

Table S2.7. The 150 K Mössbauer parameters for the two quadrupole doublets representing the belt Fe sites in the M^N state.

	Doublet 1	Doublet 2
δ (mm s^{-1})	0.33	0.44
$\lvert\Delta E_Q\rvert$ (mm s^{-1})	0.68	0.69
Γ (mm s^{-1})	0.27	0.17
Rel. Area (%)	84.1	15.9

Table S2.8. The weighted average of the isomer shift and quadrupole splitting for the belt sites in the M^N state.

	50 K	80 K	150 K
δ (mm s^{-1})	0.38	0.38	0.34
$\lvert\Delta E_Q\rvert$ (mm s^{-1})	0.73	0.70	0.68

Simulation of the NifDK–M($^{57}Fe_1$) Mössbauer spectra in the M^N state at 4.7 K, 77 mT

The analysis of magnetic Mössbauer spectra of NifDK in its $S = {}^3/_2$ resting state (the M^N state) has been previously reported.[2, 10] Simulations were generated using the WMOSS software package.[27]

In short, the magnetic Mössbauer spectra can be described with the following spin Hamiltonian:

$$\mathcal{H} = S \cdot D \cdot S + \beta S \cdot g \cdot B + \sum_{i=1}^{n} [S \cdot A(i) \cdot I(i) - g_N \beta_N B \cdot I(i) + \mathcal{H}_Q(i)] \quad (14)$$

The first term describes the zero-field splitting (ZFS) interaction and is parametrized by the axial and rhombic ZFS parameters, *D* and *E/D* respectively; various studies[10, 12] have determined that $D = 6\ cm^{-1}$ and $E/D = 0.05$. The second term describes the electron Zeeman interaction, where the *g*-tensor for FeMo-co is [2.00 2.00 2.03].[10] The third term describes the magnetic hyperfine interaction of the ^{57}Fe nucleus with the total spin of the cluster. The magnetic hyperfine tensors, *A(i),* are rotated with respect to the zero-field splitting tensor by Euler angles following the ZYZ convention. The fourth term describes the nuclear Zeeman interaction for each ^{57}Fe nucleus. The last term describes the interaction between the nuclear moment of the ^{57}Fe nucleus in its excited state and the electric field gradient:

$$\mathcal{H}_Q = \frac{eQV_{ZZ}}{12} [3{I_Z}^2 - I(I+1) + \eta({I_x}^2 - {I_y}^2)] \quad (15)$$

Here, *e* is the elementary charge, *Q* is the quadrupole moment of the excited state of the ^{57}Fe nucleus, *I* is the nuclear spin of the ^{57}Fe nucleus in its excited state ($I = {}^3/_2$), and η is the asymmetry parameter defined by $\eta = (V_{xx} - V_{yy})/V_{zz}$; this parameter can be constrained such that $0 < \eta < 1$. Another set of Euler angles are used to rotate the EFG tensor with respect to the ZFS tensor.

Our simulation (shown in Fig. S2.6, Table S2.9, and in the main text Fig. 2.8) of the NifDK–M($^{57}Fe_1$) of the magnetic Mössbauer data fixed the $\boldsymbol{A}(Fe1)$-tensor and its orientation relative to the D-tensor frame, as these values were determined through our ENDOR experiments. Note that both g_1 and g_2 as well as ${}^TA_1$ and ${}^TA_2$ as determined in

the ENDOR analysis are permuted in Yoo *et al*.[2] and in the WMOSS input. The relative contributions from the Fe1 site and the fifteen sites containing natural abundance ^{57}Fe were determined as discussed in the simulation of the variable temperature data of the NifDK–M($^{57}Fe_1$) sample.

The following variables were allowed to float:

1) Isomer shift for the Fe1 site
2) Quadrupole splitting for the Fe1 site
3) Asymmetry parameter, η, for the Fe1 site
4) Euler angles for the EFG tensor
5) Linewidths for the Fe1 site
6) Area coefficient for the NifDK–M($^{57}Fe_1$) data set

Note that variations in some parameters, particularly the Euler angles of the electric field gradient and the sign of the quadrupole splitting, can yield multiple, nearly identical simulations for the NifDK–M($^{57}Fe_1$) spectra. However, these simulations feature nearly identical values for the two parameters that are central to our analysis: the isomer shift and the magnitude of the quadrupole splitting for the Fe1 site (with variations of only ~0.01 mm s^{-1} between different simulations). As such, uncertainty in the electric field gradient Euler angles and the magnitude of the quadrupole splitting do not affect our conclusions. Illustrative simulations are presented below. Simulation 1 (Fig. S2.6, Table S2.9, and in the main text Fig. 2.8) is our preferred simulation and uses a positive quadrupole splitting. Simulation 2 (Fig. S2.7 and Table S2.10) is an alternative simulation with a positive quadrupole splitting with different Euler angles for the electric field gradient. Simulation 3 (Fig. S2.8 and Table S2.11) is an alternative simulation that utilizes a negative quadrupole splitting.

Table S2.9. Mössbauer parameters for the simulation of the NifDK–M($^{57}Fe_1$) data shown in Fig. S2.6 and Fig. 2.8.

	Fe1	**Fe^{2+}**
δ (mm s^{-1})	0.54	1.4
ΔE_Q (mm s^{-1})	1.32	3.15
Γ (mm s^{-1})	0.39	0.31
Rel. Area (%)	73	4
η	0.73	-
α_{efg}	88	-
β_{efg}	110	-
γ_{efg}	49	-
A_x (MHz)	-18.3	-
A_y (MHz)	-14	-
A_z (MHz)	-19.5	-
α_A	10	-
β_A	15	-
γ_A	0	-

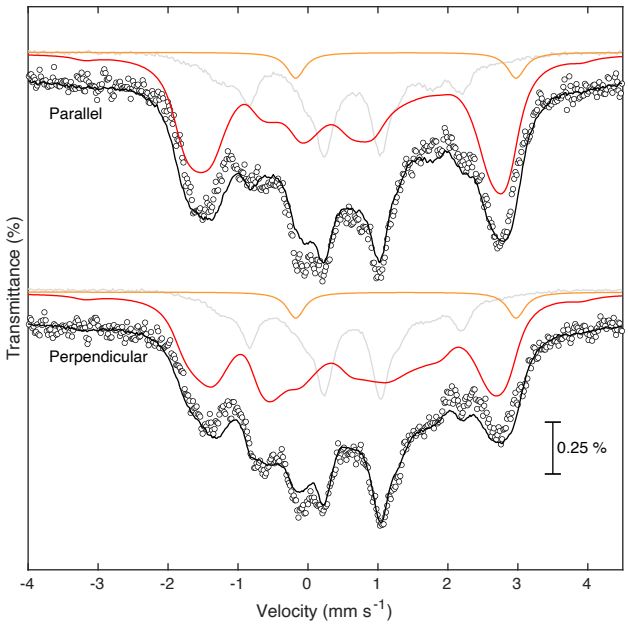

Figure S2.6. Mössbauer spectra of the NifDK–M($^{57}Fe_1$) sample in the M^N state recorded at 4.7 K in the presence of a 77 mT external field oriented parallel (top) or perpendicular (bottom) to the incident radiation. Mössbauer parameters are shown in Table 13. Circles are the experimental data; black traces are the total simulations; red traces are the simulations for the Fe1 site; gray traces are the corresponding NifDK–P($^{57}Fe_8$)–M($^{57}Fe_7$) spectra scaled to account for the natural-abundance contribution from the 15 Fe sites; orange traces are the simulations for the high spin Fe^{2+} site.

Table S2.10. Mössbauer Parameters for the simulation of the NifDK–M($^{57}Fe_1$) data shown in Fig. S2.7.

	Fe1	**Fe^{2+}**
δ (mm s^{-1})	0.54	1.4
ΔE_Q (mm s^{-1})	1.32	3.15
Γ (mm s^{-1})	0.42	0.31
Rel. Area (%)	73	4
η	0.71	-
α_{efg}	97	-
β_{efg}	67	-
γ_{efg}	57	-
A_x (MHz)	-18.3	-
A_y (MHz)	-14	-
A_z (MHz)	-19.5	-
α_A	10	-
β_A	15	-
γ_A	0	-

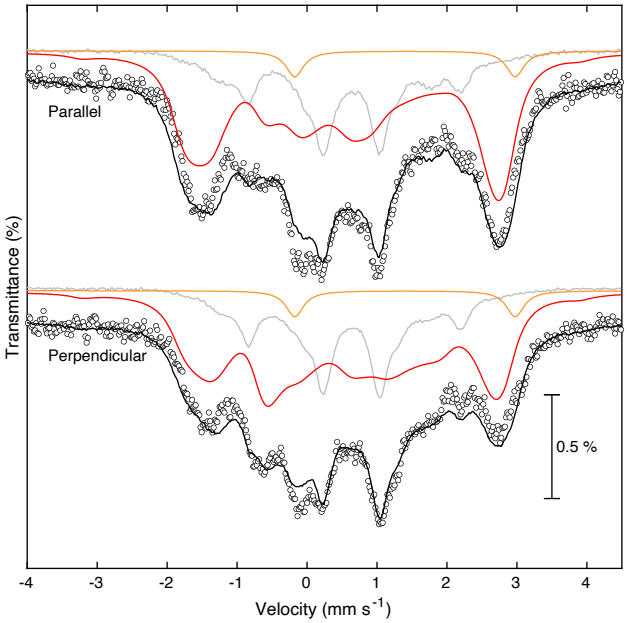

Figure S2.7. Alternative simulation of the Mössbauer spectra of the NifDK–M($^{57}Fe_1$) sample in the M^N state recorded at 4.7 K in the presence of a 77 mT external field oriented parallel (top) or perpendicular (bottom) to the incident radiation. Mössbauer parameters are shown in Table S2.10. Circles are the experimental data; red traces are the simulations for the Fe1 site, gray traces are the corresponding NifDK–P($^{57}Fe_8$)–M($^{57}Fe_7$) spectra scaled to account for the natural-abundance contribution from the 15 Fe sites; orange traces are the simulations for the high spin Fe^{2+} site.

Table S2.11. Mössbauer Parameters for the simulation of the NifDK–M($^{57}Fe_1$) data shown in Fig. S2.8.

	Fe1	**Fe^{2+}**
δ (mm s^{-1})	0.53	1.38
ΔE_Q (mm s^{-1})	-1.32	3.20
Γ (mm s^{-1})	0.38	0.26
Rel. Area (%)	75	5.2
η	1	-
α_{efg}	158	-
β_{efg}	48	-
γ_{efg}	25	-
A_x (MHz)	-18.3	-
A_y (MHz)	-14	-
A_z (MHz)	-19.5	-
α_A	10	-
β_A	15	-
γ_A	0	-

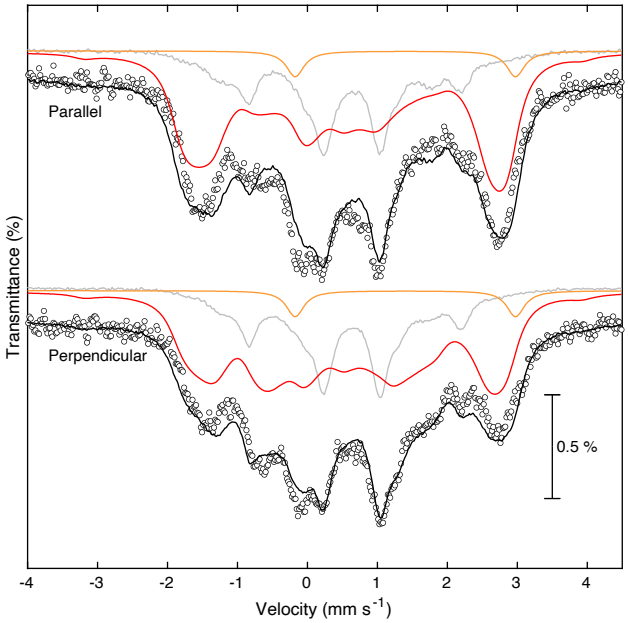

Figure S2.8. Simulation of the Mössbauer spectra of the NifDK–M($^{57}Fe_1$) sample using a negative ΔE_Q in the M^N state recorded at 4.7 K in the presence of a 77 mT external field oriented parallel (top) or perpendicular (bottom) to the incident radiation. Mössbauer parameters are shown in in Table S2.11. Circles are the experimental data; red traces are the simulations for the Fe1 site, gray traces are the corresponding NifDK–P($^{57}Fe_8$)–M($^{57}Fe_7$) spectra scaled to account for the natural-abundance contribution from the 15 Fe sites; orange traces are the simulations for the high spin Fe^{2+} site.

2.7.5. Additional data

Table S2.12. The specific C_2H_2 reduction activity of as-isolated NifDK, NifDK generated from FeMo-co insertion, NifDK generated from insertion of postbiosynthetically modified FeMo-co, and the latter two that have been further treated with EDTA to remove Co-containing impurities, which results in modestly lower activity.

Activity (nmol of ethylene formed per min per mg of NifDK)	As-isolated	EDTA-treated
As-isolated His-NifDK	1530 ± 70	-
His-NifDK (inserted)	1600 ± 100	900 ± 100
His-NifDK (inserted + treatment)	1580 ± 80	1100 ± 200

Table S2.13. The 4.2 K Mössbauer isomer shifts for Fe sites in different protein-bound Fe–S clusters as compiled by Pandelia *et al.*[1]

	$[Fe_4S_4]^{3+}$		$[Fe_4S_4]^{2+}$	$[Fe_4S_4]^{1+}$	
	Fe^{3+}	$Fe^{2.5+}$	$Fe^{2.5+}$	$Fe^{2.5+}$	Fe^{2+}
δ (mm s^{-1})	0.29	0.40	0.42	0.49	0.58
$\lvert\Delta E_Q\rvert$ (mm s^{-1})	0.88	1.03	1.12 (avg.)	1.32	1.89

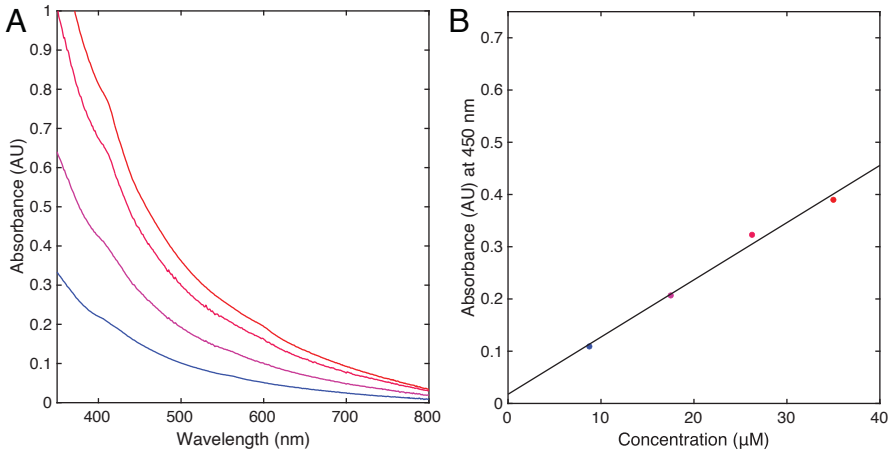

Figure S2.9. Determining the extinction coefficient of PhS-bound FeMo-co. A, UV-vis data of isolated FeMo-co in the presence of excess PhSH. **B,** Absorbance at 450 nm plotted vs. concentration of FeMo-co. Red to blue: 35 μM, 26, 18, 8.8 μM FeMo-co as determined by analyzing the Mo concentration via ICP-MS.

2.7.6. Computational Details

All calculations were carried out using version 4.1.2 of the ORCA program package.[34] Single-point calculations were performed assuming a total electron count of 41 electrons for the metal core of FeMo-co, with the arrangement of spins described by the broken-symmetry solutions from the BS7 family, which has been proposed[17-18, 20-21] to be lowest in energy. This class of solutions contains three unique spin isomers: BS7-235, BS7-247, and BS7-346. The coordinates were obtained from optimized geometries for these spin isomers as previously reported.[17] For simplicity, we simplified the model to include only the atoms of FeMo-co and those that approximate the primary coordination sphere of the cofactor; His442 was approximated as 4-methylimidazole, and Cys275 was approximated as (*R*)-*N*-(1-mercapto-3-oxopropan-2-yl)formamide. Following the methodology employed by Björnnson and coworkers,[17-18] these calculations used the GGA exchange-correlation functional BP86 in conjunction with the second-order Douglas-Kroll-Hess (DKH2) Hamiltonian to account for scalar relativistic effects. The basis set for all atoms used def2-TVSP with the RIJCOSX approximation and the very fine auxiliary integration grid (GridX7) to speed up calculations. All atoms used the auxiliary basis SARC/J. The broken-symmetry solutions for each spin-isomer

were first converged to the high-spin solution (M_s = 35/2) and then the spin of the respective Fe sites for a particular isomer were flipped, followed by converging to the M_s = $^3/_2$ solution.

2.8. Experimental and methods

Cell growth

The *Azotobacter vinelandii* strains DJ1141 (produces His-tagged NifDK), DJ1143 (produces His-tagged apo-NifDK), and wild-type (WT) *A. vinelandii* were cultured in 18 L batches in a 20 L B. Braun Biostat C bioreactor using Burk's minimal medium (6 mM sucrose, 0.9 mM $MgSO_4 \cdot 7H_2O$, 0.6 mM $CaCl_2 \cdot 2H_2O$, 18 μM $FeSO_4 \cdot 7H_2O$, 2 mM KH_2PO_4, 2 mM KH_2PO_4, 5 mM KH_2PO_4) supplemented with 1 μM $Na_2MoO_4 \cdot 2H_2O$.

For overproducing holo-NifDK, growths were supplemented with 6 mM ammonium acetate. Derepression was initiated upon ammonium depletion, and cells were harvested after 3 hours.[35] Cell paste was flash-frozen in LN_2 and stored at –80 °C until purification.

For the culturing of DJ1143, the Burk's minimal medium was supplemented with 10 mM urea. Once the cell density reached an OD_{600} of approximately 4.0, derepression was initiated by resuspending pelleted cells in Burk's minimum medium containing no urea. After 3 hours, the cells were harvested by centrifugation and the cell paste was flash-frozen in LN_2 and stored at –80 °C until needed.

^{57}Fe-enriched NifDK protein was generated using identical protocols to what was described above except that the Fe source was generated by dissolving ^{57}Fe powder (Trace Science International, 95.5% enrichment) with stoichiometric H_2SO_4.

NifDK purification

All NifDK purification procedures were carried out in a Coy Labs glove box (<5 ppm O_2). All aqueous solutions used were sparged with N_2 overnight. Cells were lysed using the osmotic shock method as followed: DJ1141 cell paste was resuspended with 3 mL of 25 mM HEPES pH 7.5, 50% glycerol, and 2 mM sodium dithionite (DTH) for every gram of cell paste. After stirring at room temperature for 15 minutes, the cells were pelleted at 25,000 × g for 15 minutes. The supernatant was poured off and the pelleted cells were resuspended with 3 mL buffer containing 25 mM HEPES pH 7.5, 2 mM (DTH), 3 mM phenylmethylsulfonyl fluoride (PMSF), 1 mg/mL lysozyme, and 100 μg/mL DNase I for every gram of cell paste. After 15 minutes of stirring, the lysate was

pelleted at 100,000 × g for 1 hour and loaded onto a Co-NTA column equilibrated with buffer containing 500 mM NaCl, 25 mM HEPES pH 7.5, 20% glycerol, and 2 mM DTH. The immobilized protein was washed with 10 column volumes of equilibration buffer and eluted with equilibration buffer containing 200 mM imidazole. NifDK was further purified using anion exchange chromatography: the protein solution was diluted 4-fold with buffer containing 25 mM HEPES pH 7.5, 20% glycerol, and 2 mM DTH and then loaded onto a DEAE-sepharose column charged with NaCl and equilibrated with the dilution buffer. The column was washed with 10 column volumes of 160 mM NaCl, 25 mM HEPES pH 7.5, 2 mM DTH, and 20% glycerol. The immobilized protein was then eluted with buffer containing 500 mM NaCl, 25 mM HEPES pH 7.5, 2 mM DTH, and 20% glycerol. Purified NifDK was concentrated using an AMICON stirred cell equipped with a 30 kDa filter, flash-frozen, and stored in LN_2. The concentration of NifDK was estimated by determining the Mo content using inductively coupled plasma mass spectrometry (ICP-MS).

Note: In our study, the reported concentration of NifDK is based on the αß heterodimer concentration (with one FeMo-co per heterodimer in holo-NifDK) rather than the $\alpha_2ß_2$ heterotetramer concentration (with two FeMo-co per heterotetramer in holo-NifDK).

NifH purification

The purification of NifH was carried out in an MBRAUN glove box (<5 ppm O_2) and was performed similarly to what has been previously reported.[36] WT *A. vinelandii* cell paste was lysed as described above. Lysate was loaded onto a DE-52 column charged with NaCl and equilibrated in 25 mM HEPES pH 7.5 and 2 mM DTH. The column was washed with a stepwise gradient with buffer containing 125 mM, 200 mM, 300 mM, and 500 mM NaCl. Fractions were analyzed by EPR spectroscopy; those determined to have NifH were pooled and concentrated using a DE-52 cellulose column and AMICON spin filters equipped with a 10 kDa filter. NifH was then purified further using an Superdex 200 column equilibrated with buffer containing 200 mM NaCl, 25 mM HEPES pH 7.5, and 2 mM DTH. Purified NifH was subsequently concentrated and

flash-frozen in LN_2. The concentration of NifH was estimated by UV-vis spectroscopy (6600 M^{-1} cm^{-1} at 400 nm).[36]

Isolation of FeMo-co

The protocol for FeMo-co isolation was adapted from a previously reported procedure.[5] Protein manipulation was performed in a Coy Labs glove box (<5 ppm O_2) and FeMo-co manipulation was carried out in an MBRAUN or Vacuum Atmospheres glove box (<5 ppm O_2). NifDK (typical protein concentrations ranging from 100 to 400 μM αß dimer) was diluted 10-fold with aqueous 2 mM DTH. The protein was denatured by the addition of 100 mM citric acid (1.67 mL per 10 mL of diluted protein) added dropwise at 0 ˚C with stirring. After incubating the mixture for 30 s the protein was precipitated by addition of 200 mM Na_2HPO_4 (1.7 mL per 10 mL of diluted protein). The precipitated protein was transferred to a 15 mL conical tube and moved to the Mbraun box where the protein was pelleted at 120 × g for 5 min using a Labnet Z100A centrifuge. The supernatant was removed and the pellet was washed with *N,N*-dimethylformamide (DMF) (5 mL) and pelleted. This DMF wash step was performed once more. FeMo-co was then extracted by resuspending and vortexing the pellet with 1 to 2 mL of *N*-methylformamide (NMF) containing 2 mM Na_2HPO_4 (from a 200 mM aqueous stock solution). After a 5-minute incubation at room temperature, the extract was centrifuged at 500 × g for 5 minutes, and the brown supernatant was poured off and collected. The process was repeated until the solution was colorless, and the extracts were combined. The concentration of FeMo-co was estimated by UV-vis spectroscopy using an extinction coefficient of PhS-bound FeMo-co in NMF: 14,800 M^{-1} cm^{-1} at 450 nm (Fig. S2.9).

Postbiosynthetic isotope editing of FeMo-co

Isolated FeMo-co (either ^{57}Fe-enriched or natural-abundance) was treated with 30 equiv ethylenediaminetetraacetic acid (EDTA) (added as a 100 mM aqueous stock solution) and stirred at room temperature for 5 minutes. Then 35 equiv $FeCl_2$ (either natural-abundance or ^{57}Fe-enriched) was added (as a 100 mM stock solution in 50% v/v NMF/H_2O), and the solution was stirred for 3 minutes at room temperature. Prolonged

incubation of EDTA-treated FeMo-co with $FeCl_2$ can lead to the appearance of an unidentified $S = {}^5/_2$ EPR signal (g_{eff} = 4.3). However, samples with this signal are competent for insertion of FeMo-co into apo-NifDK, and as such the reaction with excess $FeCl_2$ appears to be reversible.

Insertion of FeMo-co into apo-NifDK protein

The procedure for inserting FeMo-co onto apo-NifDK protein was adapted from previous reports.[6, 37] Excess as-isolated or postbiosynthetically modified FeMo-co (up to 1.5 equiv) was added dropwise to freshly prepared crude lysate of DJ1143 (lysed using osmotic shock), stirred at room temperature. The final concentration of NMF was approximately 1% v/v. Once FeMo-co addition was complete, the now holo-NifDK protein was purified as described above with an additional step. Following anion exchange chromatography, the NifDK protein was applied to a Superdex 200 column equilibrated in 500 mM NaCl, 25 mM HEPES pH 7.5, 20% glycerol, and 2 mM DTH. Fractions containing NifDK protein were pooled and concentrated. Note: We estimate that 1 g of DJ1143 cell paste grown by the method described above contains ~10 nmol of apo-NifDK; this value was determined by measuring the yield of apo-NifDK isolated over several purifications from a fixed amount of DJ1143 cell paste.

Acetylene reduction activity assays

The specific activity of NifDK was assessed using the acetylene reduction activity assay. Assays were performed in 10-ml crimped vials under an atmosphere of 90:10 argon/acetylene in a water bath at 30 °C. Each assay contained 800 µL ATP mix (25 mM Tris buffer (pH 7.9), 30 mM creatine phosphate disodium salt, 5 mM ATP disodium salt, 5 mM $MgCl_2$, 25 units ml^{-1} phosphocreatine kinase and 20 mM DTH), 100 µg NifDK and 435 µg NifH. Assays were initiated with the addition of NifH and quenched after 6 min with 100 µL of 4 M NaOH. Ethylene production was measured by injecting 50 µL of headspace into an Agilent 6890N gas chromatograph equipped with a flame ionization detector and an HP-PLOT/Q 30 m × 0.319 mm × 20.00 µm column. Ethylene standards were prepared by injecting 1 mL ethylene into gravimetrically calibrated round-bottomed flasks containing 1 atm air.

Mössbauer sample preparation

Samples were poised in the M^N state by incubation with DTH and then were subsequently flash frozen in a Mössbauer cup.

Spectroscopy and spectrometry

Zero-field ^{57}Fe-Mössbauer spectra were recorded with a constant acceleration spectrometer equipped with a JANIS closed cycle He gas refrigerator cryostat. Isomer shifts were quoted relative to α-Fe foil at room temperature. EPR samples were prepared in an anaerobic glove box with an N_2 atmosphere and an O_2 level of <5 ppm. X-band EPR spectra were recorded on a Bruker EMX spectrometer at 9.37 GHz. Q-band ENDOR data were collected using a locally constructed spectrometer.[38] Inductively coupled plasma mass spectrometer (ICP-MS) data were recorded on an Agilent 7900 ICP-MS instrument. Protein samples were digested with concentrated nitric acid (TraceMetal Grade, Fischer) at 70 °C and were diluted with Milli-Q water to final concentration of 2% nitric acid. Standards for Mo were prepared from a 1000 ppm standard solution (VWR BDH Chemicals). Standards for Fe and ^{56}Fe were prepared from a 1000 ppm standard solution (SPEX Certiprep). Standards for ^{57}Fe were prepared as described previously.[4] The concentrations of ^{56}Fe and ^{57}Fe in the standard solutions were based on the natural abundance of each isotope in the unenriched standard (91.7% ^{56}Fe, 2.12% ^{57}Fe) and the isotope enrichment in ^{57}Fe powder (95.5% ^{57}Fe, 3.6% ^{56}Fe).

2.9. References

1. Pandelia, M.-E., Lanz, N. D., Booker, S. J. & Krebs, C., Mössbauer spectroscopy of Fe/S proteins. *Biochimica et Biophysica Acta (BBA) - Molecular Cell Research* **2015,** *1853* (6), 1395-1405.
2. Yoo, S. J., Angove, H. C., Papaefthymiou, V., Burgess, B. K. & Münck, E., Mössbauer Study of the MoFe Protein of Nitrogenase from *Azotobacter vinelandii* Using Selective ^{57}Fe Enrichment of the M-Centers. *Journal of the American Chemical Society* **2000,** *122* (20), 4926-4936.
3. Spatzal, T., Schlesier, J., Burger, E.-M., Sippel, D., Zhang, L., Andrade, S. L. A., Rees, D. C. & Einsle, O., Nitrogenase FeMoco investigated by spatially resolved anomalous dispersion refinement. *Nature Communications* **2016,** *7* (1), 10902.
4. Srisantitham, S., Badding, E. D. & Suess, D. L. M., Postbiosynthetic modification of a precursor to the nitrogenase iron–molybdenum cofactor. *Proceedings of the National Academy of Sciences* **2021,** *118* (11), e2015361118.
5. Shah, V. K. & Brill, W. J., Isolation of an iron-molybdenum cofactor from nitrogenase. *Proceedings of the National Academy of Sciences* **1977,** *74* (8), 3249-53.
6. Christiansen, J., Goodwin, P. J., Lanzilotta, W. N., Seefeldt, L. C. & Dean, D. R., Catalytic and biophysical properties of a nitrogenase Apo-MoFe protein produced by a *nifB*-deletion mutant of *Azotobacter vinelandii*. *Biochemistry* **1998,** *37* (36), 12611-23.
7. Rawlings, J., Shah, V. K., Chisnell, J. R., Brill, W. J., Zimmermann, R., Münck, E. & Orme-Johnson, W. H., Novel metal cluster in the iron-molybdenum cofactor of nitrogenase. Spectroscopic evidence. *Journal of Biological Chemistry* **1978,** *253* (4), 1001-4.
8. Yang, S. S., Pan, W. H., Friesen, G. D., Burgess, B. K., Corbin, J. L., Stiefel, E. I. & Newton, W. E., Iron-molybdenum cofactor from nitrogenase. Modified extraction methods as probes for composition. *Journal of Biological Chemistry* **1982,** *257* (14), 8042-8048.
9. Van Stappen, C., Davydov, R., Yang, Z.-Y., Fan, R., Guo, Y., Bill, E., Seefeldt, L. C., Hoffman, B. M. & DeBeer, S., Spectroscopic Description of the E_1 State of Mo Nitrogenase Based on Mo and Fe X-ray Absorption and Mössbauer Studies. *Inorganic Chemistry* **2019,** *58* (18), 12365-12376.
10. Münck, E., Rhodes, H., Orme-Johnson, W. H., Davis, L. C., Brill, W. J. & Shah, V. K., Nitrogenase. VIII. Mössbauer and EPR spectroscopy. The MoFe protein component from *Azotobacter vinelandii* OP. *Biochimica et Biophysica Acta (BBA) - Protein Structure* **1975,** *400* (1), 32-53.
11. True, A. E., Nelson, M. J., Venters, R. A., Orme-Johnson, W. H. & Hoffman, B. M., Iron-57 hyperfine coupling tensors of the FeMo cluster in *Azotobacter vinelandii* MoFe protein: determination by polycrystalline ENDOR spectroscopy. *Journal of the American Chemical Society* **1988,** *110* (6), 1935-1943.
12. Venters, R. A., Nelson, M. J., McLean, P. A., True, A. E., Levy, M. A., Hoffman, B. M. & Orme-Johnson, W. H., ENDOR of the resting state of nitrogenase molybdenum-iron proteins from *Azotobacter vinelandii*, *Klebsiella pneumoniae*, and *Clostridium*

pasteurianum. Proton, iron-57, molybdenum-95, and sulfur-33 studies. *Journal of the American Chemical Society* **1986,** *108* (12), 3487-3498.
13. Mouesca, J. M., Noodleman, L., Case, D. A. & Lamotte, B., Spin Densities and Spin Coupling in Iron-Sulfur Clusters: A New Analysis of Hyperfine Coupling Constants. *Inorganic Chemistry* **1995,** *34* (17), 4347-4359.
14. Papaefthymiou, V., Girerd, J. J., Moura, I., Moura, J. J. G. & Muenck, E., Moessbauer study of *D. gigas* ferredoxin II and spin-coupling model for Fe_3S_4 cluster with valence delocalization. *Journal of the American Chemical Society* **1987,** *109* (15), 4703-4710.
15. Noodleman, L., Exchange coupling and resonance delocalization in reduced iron-sulfur $[Fe_4S_4]^+$ and iron-selenium $[Fe_4Se_4]^+$ clusters. 1. Basic theory of spin-state energies and EPR and hyperfine properties. *Inorganic Chemistry* **1991,** *30* (2), 246-256.
16. Venkateswara Rao, P. & Holm, R. H., Synthetic Analogues of the Active Sites of Iron–Sulfur Proteins. *Chemical Reviews* **2004,** *104* (2), 527-560.
17. Benediktsson, B. & Bjornsson, R., QM/MM Study of the Nitrogenase MoFe Protein Resting State: Broken-Symmetry States, Protonation States, and QM Region Convergence in the FeMoco Active Site. *Inorganic Chemistry* **2017,** *56* (21), 13417-13429.
18. Bjornsson, R., Neese, F. & DeBeer, S., Revisiting the Mössbauer Isomer Shifts of the FeMoco Cluster of Nitrogenase and the Cofactor Charge. *Inorganic Chemistry* **2017,** *56* (3), 1470-1477.
19. Solomon, E. I., Gorelsky, S. I. & Dey, A., Metal–thiolate bonds in bioinorganic chemistry. *Journal of Computational Chemistry* **2006,** *27* (12), 1415-1428.
20. Lovell, T., Li, J., Liu, T., Case, D. A. & Noodleman, L., FeMo Cofactor of Nitrogenase: A Density Functional Study of States M^N, M^{OX}, M^R, and M^I. *Journal of the American Chemical Society* **2001,** *123* (49), 12392-12410.
21. Lukoyanov, D., Pelmenschikov, V., Maeser, N., Laryukhin, M., Yang, T. C., Noodleman, L., Dean, D. R., Case, D. A., Seefeldt, L. C. & Hoffman, B. M., Testing if the Interstitial Atom, X, of the Nitrogenase Molybdenum–Iron Cofactor Is N or C: ENDOR, ESEEM, and DFT Studies of the *S* = 3/2 Resting State in Multiple Environments. *Inorganic Chemistry* **2007,** *46* (26), 11437-11449.
22. Lukoyanov, D. A., Yang, Z.-Y., Perez-Gonzalez, A., Raugei, S., Dean, D. R., Seefeldt, L. C. & Hoffman, B. M., ^{13}C ENDOR Characterization of the Central Carbon Within the Nitrogenase Catalytic Cofactor Indicates the CFe_6 Core is a Stabilizing Heart of Steel. *Journal of the American Chemical Society* **2022,** *In Press*.
23. Pérez-González, A., Yang, Z.-Y., Lukoyanov, D. A., Dean, D. R., Seefeldt, L. C. & Hoffman, B. M., Exploring the Role of the Central Carbide of the Nitrogenase Active-Site FeMo-cofactor through Targeted ^{13}C Labeling and ENDOR Spectroscopy. *Journal of the American Chemical Society* **2021,** *143* (24), 9183-9190.
24. DeRose, V. J. & Hoffman, B. M., [23] Protein structure and mechanism studied by electron nuclear double resonance spectroscopy. In *Methods in Enzymology*, Academic Press: 1995; Vol. 246, pp 554-589.
25. We believe based on our Mössbauer data on the fully enriched MoFeP that our samples do not contain the 16th Fe site.

26. Zhang, L., Kaiser, J. T., Meloni, G., Yang, K.-Y., Spatzal, T., Andrade, S. L. A., Einsle, O., Howard, J. B. & Rees, D. C., The sixteenth iron in the nitrogenase MoFe protein. *Angewandte Chemie International Edition* **2013,** *52* (40), 10529-10532.
27. Prisecaru, I. *WMOSS4 Mössbauer Spectral Analysis Software*, www.wmoss.org, 2009-2016.
28. Gütlich, P., Bill, E. & Trautwein, A. X., *Mössbauer spectroscopy and transition metal chemistry: fundamentals and applications*. Springer-Verlag: 2011.
29. Edwards, P. R., Johnson, C. E. & Williams, R. J. P., Mössbauer Spectra of Some Tetrahedral Iron (II) Compounds. *The Journal of Chemical Physics* **1967,** *47* (6), 2074-2082.
30. Dunham, W. R., Bearden, A. J., Salmeen, I. T., Palmer, G., Sands, R. H., Orme-Johnson, W. H. & Beinert, H., The two-iron ferredoxins in spinach, parsley, pig adrenal cortex, *Azotobacter vinelandii*, and *Clostridium pasteurianum*: Studies by magnetic field Mössbauer spectroscopy. *Biochimica et Biophysica Acta (BBA) - Bioenergetics* **1971,** *253* (1), 134-152.
31. Silver, J., Fern, G. R., Miller, J. R., McCammon, C. A., Evans, D. J. & Leigh, G. J., Effects of Temperature and Pressure on the Mössbauer Spectra of Models for the $[4Fe\text{-}4S]^{2+}$ Clusters of Iron–Sulfur Proteins and the Structure of $[PPh_4]_2[Fe_4S_4(SCH_2CO_2C_2H_5)_4]$. *Inorganic Chemistry* **1999,** *38* (19), 4256-4261.
32. Lovell, T., Torres, R. A., Han, W.-G., Liu, T., Case, D. A. & Noodleman, L., Metal Substitution in the Active Site of Nitrogenase MFe7S9 (M = Mo^{4+}, V^{3+}, Fe^{3+}). *Inorganic Chemistry* **2002,** *41* (22), 5744-5753.
33. Lovell, T., Li, J., Case, D. A. & Noodleman, L., FeMo cofactor of nitrogenase: energetics and local interactions in the protein environment. *Journal of Biological Inorganic Chemistry* **2002,** *7* (7-8), 735-49.
34. Neese, F., The ORCA program system. *WIREs Computational Molecular Science* **2012,** *2* (1), 73-78.
35. Lee, C.-C., Ribbe, M. W. & Hu, Y., Purification of Nitrogenase Proteins. In *Metalloproteins: Methods and Protocols*, Hu, Y., Ed. Springer New York: New York, NY, 2019; pp 111-124.
36. Burgess, B. K., Jacobs, D. B. & Stiefel, E. I., Large-scale purification of high activity *Azotobacter vinelandII* nitrogenase. *Biochimica et Biophysica Acta (BBA) - Enzymology* **1980,** *614* (1), 196-209.
37. McLean, P. A., Papaefthymiou, V., Orme-Johnson, W. H. & Münck, E., Isotopic hybrids of nitrogenase. Mössbauer study of MoFe protein with selective ^{57}Fe enrichment of the P-cluster. *Journal of Biological Chemistry* **1987,** *262* (27), 12900-12903.
38. Davoust, C. E., Doan, P. E. & Hoffman, B. M., Q-Band Pulsed Electron Spin-Echo Spectrometer and Its Application to ENDOR and ESEEM. *Journal of Magnetic Resonance, Series A* **1996,** *119* (1), 38-44.

Chapter 3. Insights into the mechanism of biological N_2 fixation through ^{57}Fe site-selective labeling

3.1. Characterizing FeMo-co in states beyond E_0

The mechanism of biological N_2 fixation—particularly the chemistry that occurs at FeMo-co, the catalytic cofactor of the Mo nitrogenase—has been intensively studied for decades.[1-6] Foundational to this inquiry is an understanding of FeMo-co's electronic structure: the distribution and coupling of the valence electrons in the resting state, and how the electronic structure changes throughout the catalytic cycle. However, the sheer number of open-shell metal ions in FeMo-co (seven structurally unique Fe sites and one Mo center[8]) pushes the limits of computational analysis[9-15] and, as described in Chapter 2, presents a number of challenges in its experimental characterization. Herein, I discuss the application of the site-selective isotopic labeling to provide insight into the redox chemistry of FeMo-co, as well as my work to use site-selective labeling to study the Janus intermediate (E_4(4H)).

3.2. Mössbauer studies of the oxidized resting state

The previous chapter discussed the characterization of the Fe1 site of FeMo-co through site-selective ^{57}Fe labeling. We discovered that the Fe1 site has an oxidation state of $Fe^{2.5+}$, and that it must be undergoing double exchange with one of the belt Fe sites. Having the ability to distinguish between the oxidation states of the Fe1 and belt Fe sites, we sought to gain insights on the relative distribution of electron density about the cofactor in M^N by oxidizing it by one electron and determining where the electron is being removed (*i.e.* which site has the highest energy electron). Previous Mössbauer studies[16] of oxidized NifDK–P($^{57}Fe_8$)–M($^{57}Fe_7$) showed that the δ_{avg} of FeMo-co at 5 K decreased to 0.35 mm s^{-1} from 0.41 mm s^{-1}. A decrease of 0.06 mm s^{-1} between M^{OX} and M^N indicated that the one electron oxidation of FeMo-co is Fe-centered;[16-17] however, it was not clear which Fe sites were participating in the redox chemistry. To address this question, we studied the oxidation of FeMo-co using the NifDK–M($^{57}Fe_1$)

sample. The reversible oxidation of M^N to M^{OX} has been reported,[16] and we adapted this procedure to poise the NifDK–M($^{57}Fe_7$), NifDK–M($^{57}Fe_6$), and NifDK–M($^{57}Fe_1$) samples in the M^{OX} state (see Fig. 3.1 and S3.11; see Table S3.1, S3.2, and S3.3 for Mössbauer parameters). The ground spin state of M^{OX} is $S = 0$,[16, 18] and its Mössbauer spectra do not exhibit magnetic splitting even at low temperature (Fig. 3.1, S3.1, and S3.2).[16, 19-21]

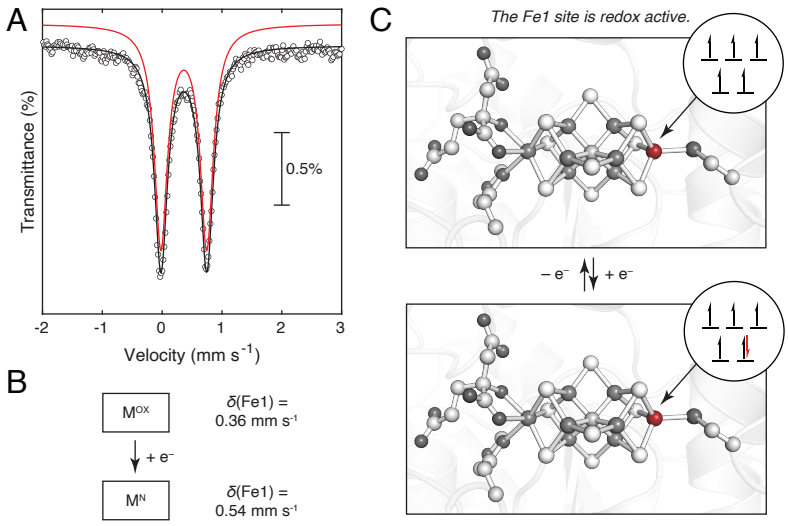

Figure 3.1. Redox changes at the Fe1 site of FeMo-co. A, Mössbauer spectrum of the oxidized NifDK–M($^{57}Fe_1$) sample recorded at 4.7 K. Circles are the experimental data; red trace is the simulation for the Fe1 site; contributions from natural-abundance ^{57}Fe have been subtracted (see Fig. S3.2). **B,** Change in isomer shift (4.7 K) for the Fe1 site upon reduction of M^{OX} to M^N. **C,** Oxidation state of the Fe1 site in M^{OX} (top) and M^N (bottom), where the red electron in the latter represents the electron shared with Fe2, Fe3, or Fe4 via the double exchange mechanism. PDB accession code: 3U7Q[8].

Comparison of the 4.7 K Mössbauer parameters for the Fe1 site in the M^N and M^{OX} states (Fig. 3.1B) reveals a striking shift in hyperfine parameters: δ decreases from 0.54 mm s^{-1} to 0.36 mm s^{-1} upon oxidation, and $|\Delta E_Q|$ likewise decreases from 1.32 to 0.77 mm s^{-1}. Though substantial, the magnitude of the decrease in δ (0.18 mm s^{-1}) is smaller than what would be expected for a localized, Fe^{2+} to Fe^{3+} redox event (~0.4 mm s^{-1}) and is instead consistent with conversion of an ~$Fe^{2.5+}$ site to an Fe^{3+} site (Table S3.9).[7] The value of δ_{avg} (80 K) for the belt sites decreases modestly upon oxidation from 0.38 mm s^{-1} in M^N to 0.33 mm s^{-1} in M^{OX}. The magnitude of this change (~0.05

mm s^{-1} over six sites, or 0.30 mm s^{-1} in total) is likewise consistent with the removal of approximately half an electron from the six belt sites (c.f. the Mössbauer spectra for $[Fe_4S_4]^{2+/+}$ clusters, whose isomer shifts differ by ~0.48 mm s^{-1} per electron when normalized to one site). We therefore conclude that the Fe1 site and its double-exchange-coupled partner are redox-active in the interconversion of M^N and M^{OX}, and it follows that these metal centers are the most reducing in M^N.

The finding that Fe1 is redox-active, even though it is not thought to be involved in substrate binding,[3-4, 22-24] may indicate a role for this site as a redox reservoir during catalysis. In such a scenario, an electron stored at Fe1 could be deployed in multi-electron steps occurring at other metal sites (*e.g.*, protonation at an Fe site to generate an Fe–hydride, which is formally a two-electron oxidation).[22, 25-29] Belt Fe sites directly involved in bond-making or -breaking steps would therefore only need to supply a single electron in a two-electron reaction because the additional electron can be derived from the Fe1 site (and its double-exchange-coupled partner). Additionally, the ability to observe redox changes in the M^N and M^{OX} states using site-selectively labeled samples demonstrates the promise of site-selective isotope editing in characterizing other intermediates and providing new insights into the mechanism of biological nitrogen fixation. This will be expanded on in the next section of this chapter.

3.3. Assessing ^{57}Fe scrambling under turnover conditions

Using our site-selectively labeled samples to characterize intermediates under turnover conditions—for example for N_2 reduction—requires that the ^{57}Fe label at the Fe1 site is not lost and does not scramble into other sites during turnover. The latter possibility is raised by recent studies[30-33] demonstrating that FeMo-co is structurally dynamic under turnover conditions. The plasticity of FeMo-co was first demonstrated[31] by Spatzal and coworkers, in which a crystal structure of carbon monoxide (CO) inhibited NifDK showed that CO had displaced one of the belt sulfides. Subsequent crystallographic studies[30] further corroborated the lability of the belt sulfides by monitoring the structural conversion of NifDK after turnover in the presence of KSeCN. The authors reported that the selenium from the KSeCN was incorporated selectively

into a single belt sulfide, and that it migrates into the other belt sulfide positions under turnover conditions, implying that FeMo-co is rather dynamic during catalysis.

To test whether site-selective labeling is maintained during turnover, we subjected the NifDK–M($^{57}Fe_1$) sample to high-flux turnover conditions under N_2 for 30 min (see Experimental and methods), reisolated NifDK from the reaction mixture, and reanalyzed its metal content and spectroscopic properties (Fig. 3.2 and S3.3). The ^{57}Fe:^{56}Fe ratio determined by ICP-MS analysis is the same pre- and post-turnover (see supplementary information, section 3.9.2), and the low-temperature Mössbauer spectrum of the post-turnover sample features the same characteristic pattern of the Fe1 site as found in the pre-turnover sample, particularly at the high- and low-energy edges (the "wings") of the spectrum (ca. 2.8 and –1.7 mm s^{-1}). The foregoing results demonstrate that little to no loss or scrambling of the ^{57}Fe label occurs during turnover and that intermediates generated using NifDK–M($^{57}Fe_1$) samples will retain their ^{57}Fe label with high site-selectivity.

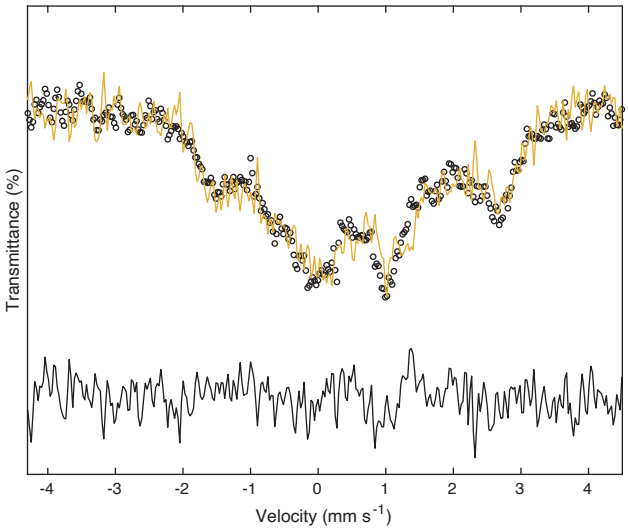

Figure 3.2. Comparison of the 5.0 K Mössbauer spectra before (black circles) and after high-flux turnover (solid yellow line). Spectra were recorded in the presence of a 77 mT magnetic field (perpendicular) and normalized to the same integrated intensity. The difference spectrum is provided in the solid black line. Note the contributions from mononuclear high spin Fe^{2+} in the pre-turnover sample are removed. See Fig. S3.3 for the raw data.

3.4. Mössbauer studies of the first intermediate of N_2 reduction, E_1

The reduction of N_2 to NH_3 by the Mo nitrogenase is believed to occur in eight steps, each related by the addition of a proton and an electron. Historically, insights into the mechanism of the Mo nitrogenase have relied heavily on the use of EPR and ENDOR spectroscopy to characterize various freeze-quenched intermediate states of FeMo-co. The use of EPR-based techniques, however, is limited to intermediates that are related to E_0 by the addition of an even number of proton and electrons. Given that there are eight predicted intermediates, this leaves half of them, such as E_1, invisible to these techniques. Instead, studies on these EPR silent, odd integer states of FeMo-co have heavy relied on techniques such as Mössbauer and Fe X-ray absorption spectroscopy.[17, 34-35] Because the resolution of these techniques is inherently low, it is difficult to resolve any responses and correlate them to a single Fe site within FeMo-co. Moreover, no experiments have elucidated the properties of a crystallographically defined Fe site in any intermediate of N_2 reduction. As an ongoing problem in the field, we therefore sought to apply the site-selective labeling protocol to overcome these challenges and study the first intermediate, E_1, where FeMo-co is in the M^R state.

Following reported protocols,[17, 34-36] we subjected the NifDK–M($^{57}Fe_1$) sample to low-flux turnover conditions (*i.e.*, turnover conditions in which NifDK is in vast excess to the FeP). Under low-flux conditions a mixture of E_0 and E_1 is generated with FeMo-co in M^N or M^R for E_0 and E_1, respectively. This mixture of states arises because under these conditions the rate of electron and proton addition to FeMo-co is slower than hydride protonation which results in relaxation from a higher E state (such as E_2 or E_3) back to E_1 and E_0, respectively. EPR spectroscopy is used to quantify the relative populations of E_0 and E_1 (Fig. S3.4 and S3.5) by comparing the strength of the $S = {}^3/_2$ EPR signal of E_0 under low flux turnover *vs.* prior to the addition of FeP. Note the assumption here is that only E_0 and E_1 are populated under low-flux conditions, and therefore the disappearance of E_0 is due to the population of E_1. EPR analysis of the NifDK–M($^{57}Fe_1$) sample under low-flux turnover generated a mixture of E_1 and E_0 in a ~60:40 ratio (Fig. S3.4 and S3.5).

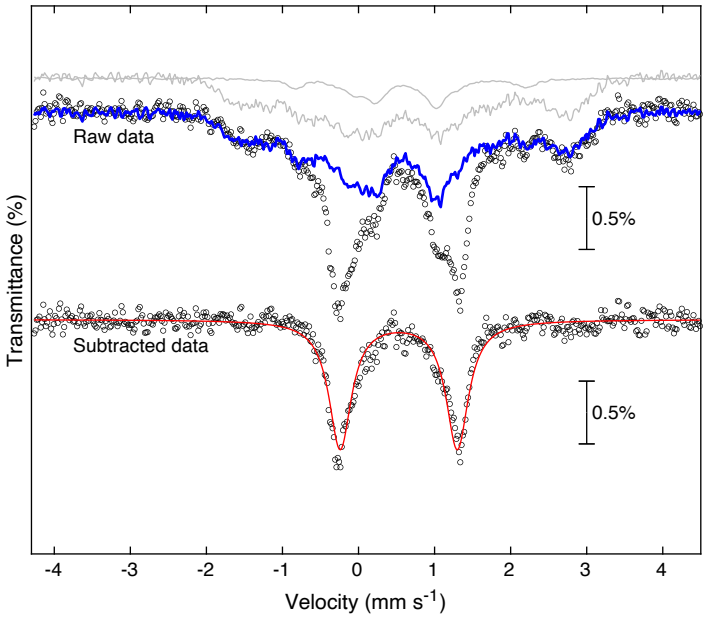

Figure 3.3. 5.0 K Mössbauer spectrum of the NifDK–M(^{57}Fe$_1$) under low-flux turnover. Gray traces represent background signals from E_1 (in natural abundance; dashed) and E_0 (both enriched at Fe1 and in natural abundance). Blue trace is the sum of the gray traces. The bottom spectrum represents the difference spectrum simulated with a single quadrupole doublet corresponding to the Fe1 site in M^R.

The resulting 5.0 K Mössbauer spectrum (Fig. 3.3) contains contributions from the signal of interest—the enriched Fe1 site in the E_1 state—as well as background signals from (i) the enriched Fe1 site in the E_0 (M^N) state, (ii) the Fe2–Fe6 centers in both states (M^N and M^R) at natural abundance, and (iii) the P-cluster (in the P^N state in both E_0 and E_1) at natural abundance. While the FeMo-co is in two distinct states in E_0 and E_1, the P-cluster remains in the P^N state as re-reduction of the P-cluster from the P^{+1} to P^N is fast. Subtracting these background signals (see supplementary information, section 3.9.3 for details and Fig. S3.6 and S3.7) leaves a clean, single quadrupole doublet (Fig. 3.3, bottom; see Tables S3.4 and S3.5 for Mössbauer parameters) that corresponds to the Fe1 site in E_1. The resulting quadrupole doublet can be simulated with the following parameters: δ = 0.53 and $|\Delta E_Q|$ = 1.54 mm s^{-1}. The similarity in Mössbauer hyperfine parameters for the Fe1 site in E_0 and E_1 therefore reveal that the proton and electron loaded into FeMo-co in the transition from E_0 to E_1 are localized at

sites other than Fe1, either in a metal–hydride bond (in the case of metal-based protonation, as has been suggested by analogy to the all-Fe nitrogenase)[37] or in a metal-based orbital (in the case of S-based protonation, as has been suggested based on spectroscopic and computational studies);[34, 38] the Fe1 site remains part of a spin-aligned pair of $Fe^{2.5+}$ sites with an unchanged primary coordination sphere.

3.5. Conclusions on the redox chemistry of the Fe1 site

This section of the chapter discusses the application of the site-selective labeling to characterize the redox chemistry of FeMo-co with respect to its resting state, M^N. First, M^{OX} was characterized using Mössbauer spectroscopy, and it was discovered that the Fe1 site and its double exchange partner are a redox active. This indicates that in M^N, these two Fe sites are the most reduced Fe sites. Next, characterization of the first intermediate of N_2 reduction, E_1, showed that the valence and primary coordination sphere is maintained for the Fe1 site in E_1, demonstrating that the changes within the cofactor upon addition of an electron and proton to FeMo-co is largely localized to the belt Fe sites and/or the Mo.

3.6 Targeting the Janus intermediate

E_4(4H) is one of the most well-studied intermediates of nitrogen fixation.[14, 22, 25-26, 28, 39-41] Its initial observation relied on using a particular variant of the Mo nitrogenase, αV70I.[42] This variant was first reported to have significantly reduced N_2 reduction activity, and therefore the authors hypothesized that position α70 acts as a gatekeeper for substrates such as N_2. Later freeze quench studies[22] of V70I NifDK under turnover conditions led to the discovery of a new $S = {}^3/_2$ EPR signal with g = [2.15, 2.00, 1.97]. ^{1}H ENDOR studies identified that two near-equivalent ^{1}Hs were present, related by some degree of rotation about FeMo-co. Based on the magnitude of the hyperfine coupling, it was proposed that these two ^{1}H were bridging hydrides with each having two Fe sites as their anchors. While at the time it was unclear what "E_N" state this new EPR signal was, by virtue of being EPR active, it was assigned to either E_2 or E_4. Subsequent cryoannealing studies[25] showed that the $S = {}^1/_2$ EPR species relaxes back to E_0 in two discrete steps, liberating H_2 in each step. The authors concluded that four protons and

electrons have accumulated onto FeMo-co, as two bridging hydrides, and therefore assigned it as $E_4(4H)$. Critical to connecting these discoveries to the mechanism of the Mo nitrogenase was demonstrating that $E_4(4H)$ can also be generated with WT NifDK, and can undergo reductive elimination in the presence of N_2 to afford an N_2-derived bound state of FeMo-co.[28] This observation in turn suggests that $E_4(4H)$ precedes the activation of N_2.

The conundrum, however, is in its resting state, FeMo-co is comprised of high-spin Fe^{2+} and Fe^{3+};[17] both of which are poor at binding and activating N_2. To date, we still do not understand what changes occur in both the chemical and electronic structure of FeMo-co that enables N_2 activation. Central to understanding this is gaining insight into the spin state, coordination sphere, and oxidation state of the Fe sites in $E_4(4H)$. So far, the studies aimed at addressing these questions have been limited to ^{57}Fe ENDOR spectroscopy because it can selectively probe the EPR-active $E_4(4H)$ state;[26] other techniques, such as Mössbauer and Fe X-ray absorption spectroscopy, probe all the Fe sites in all the populated states FeMo-co is in. Although the $\boldsymbol{A}(^{57}Fe)$ for the Fe sites have been determined for this intermediate,[26] correlating the spectroscopic information onto the geometric structure has been challenging. A recent study[39] attempted to address this challenge by comparing the $\boldsymbol{A}(^{57}Fe)$ of $E_4(4H)$ before and after photoexcitation, and led to the proposal that the spectroscopic site, A^2, is one of the anchors for one of the hydrides in $E_4(4H)$. We can directly test this hypothesis by studying the Janus intermediate with site-selectively labeled NifDK. The next section is focused on the genetics and biochemistry required for generating this sample.

3.7. Generation of ΔB DJ1373, TD1

Historically, ENDOR studies[22, 26] of $E_4(4H)$ have utilized a mutant of NifDK isolated from the DJ1373 *Av* strain: α70 Val is substituted for an Ile. Usage of V70I NifDK enables the generation $E_4(4H)$ in moderate yield which is critical for studies by ENDOR spectroscopy. A prerequisite for using the site-selective labeling methodology is the insertion of the post-biosynthetically modified cofactor, $M(^{57}Fe_1)$, into apo-NifDK. Therefore, to carry out the site-specific studies of $E_4(4H)$ using the methodology

developed in Chapter 2, the Δ*nifB* variant of the DJ1373 strain (analogous to DJ1143 for apo His-NifDK) must be generated, and the resulting apo-NifDK must be tested for its competence for cofactor reconstitution.

The microbiology and manipulation of the *Azotobacter vinelandii (Av)* genome is well established,[43] largely due to the contributions from the Dean lab at Virginia Tech. Generation of the ΔB DJ1373 *Av* strain (TD1, for "Thanks Dennis, strain 1") followed three steps adapted from the creation of DJ1143:[44] (1) producing competent *Av* cells; (2) knock out *nifB*, the gene responsible for the generation of the L-cluster, a precursor to FeMo-co;[45] and (3) selection for the desired strain. It is well-established that to make *Av* cells competent for uptake of foreign plasmids they must be cultured under Fe-deficient conditions.[46-47] The lack of Fe causes the cells to secrete a fluorescent, green siderophore used as a rough indicator for cell competency (Fig. 3.4)—note the exact link between the two has not been well studied. To knock out *nifB*, the competent cells were incubated with a plasmid, pDB218; this plasmid contains a portion of the *Av nifB* gene and a kanamycin-resistance gene cartridge.[44] Upon incubation and uptake of the plasmid, a double reciprocation event can occur in which the kanamycin-resistance gene cartridge is inserted into the *nifB* gene. Once the genome is modified, the resulting strain of *Av* will be resistant to kanamycin (which is critical for selection) and will over-produce V70I apo-NifDK. Colonies that exhibited kanamycin resistance were

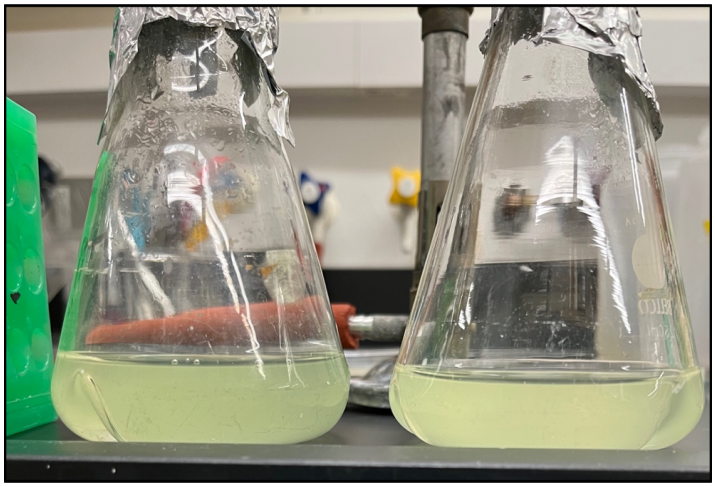

Figure 3.4. *Av* cells cultured in the absence of an Fe source.

consecutively tested for kanamycin resistance and their inability to fix N_2. After selection, the colonies that exhibited the desire phenotype were cultured and stored as glycerol stocks.

Once TD1 was generated, it was cultured as previously reported for DJ1143 (in Chapters 2 and 3) and the now FeMo-co deficient V70I NifDK was tested for its competence for cofactor insertion. Following the protocols previously reported[48] (and discussed in Chapter 2), isolated FeMo-co was incubated with the freshly prepared crude lysate of TD1 and subsequently the resulting NifDK was purified by metal affinity, anion exchange, and size exclusion chromatography. The EPR spectrum for as-isolated V70I NifDK (purified from DJ1373) is shown in Fig. 3.5, top. Consistent with previous reports,[22] in the DTH reduced state, V70I NifDK exhibits two overlapping $S = {}^3/_2$ EPR signals from FeMo-co; the two EPR signals are due to differences in the rhombicity (E/D) of the two species and are believed to arise due to different conformations of the Ile side chain.[49] The 5 K EPR spectrum of the cofactor-inserted V70I apo-NifDK is shown in the middle spectrum in Fig. 3.5 and displays two signals: (1) an $S = {}^3/_2$ EPR signal with a similar rhombicity to wt His NifDK and the dominant EPR signal in V70I; and (2) a saturated $S = {}^3/_2$ EPR signal consistent with the presence of a small amount of

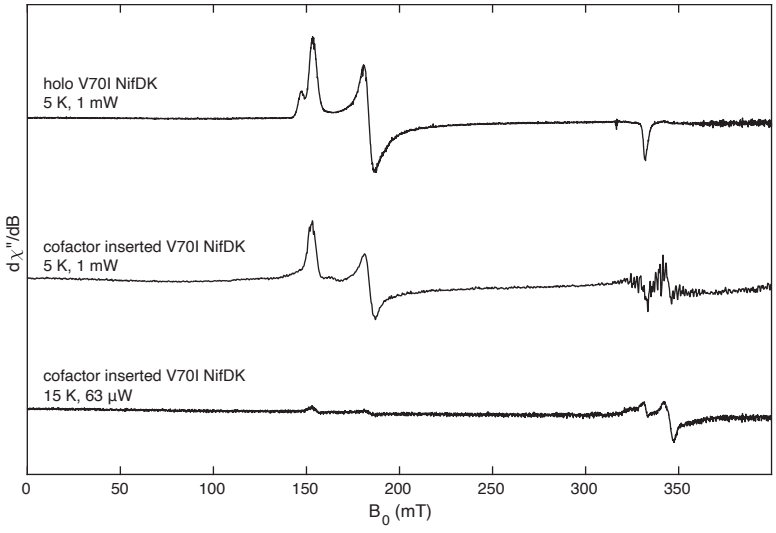

Figure 3.5. EPR spectra of V70I NifDK and cofactor inserted V70I NifDK. The corresponding EPR spectra for as-isolated V70I NifDK isolated from DJ 1373 (top) and cofactor-inserted V70I NifDK (middle) at 5 K, 1 mW. EPR spectra for cofactor inserted V70I NifDK (bottom) at 15 K, 63 µW. Both samples were recorded at 9.37 GHz.

degraded P-cluster (Fig. 3.5, bottom, shows this species under non-saturated conditions).[44] The 5 K EPR spectrum of the inserted V70I NifDK indicates that the V70I apo-NifDK is competent for cofactor insertion; however it's intriguing that the EPR spectrum only exhibits one $S = {}^{3}/_{2}$ species, which is distinct from NifDK isolated from DJ1373. It is likely that the difference in the *in vitro* vs. *in vivo* maturation of V70I apo-NifDK could result in different populations of the Ile70 side chain, with *in vitro* maturation producing only a single conformation. Whereas it has been demonstrated that V70I apo-NifDK is competent for cofactor insertion, future studies will assess if E_4(4H) can be generated in high yield, and if so, enable site-specific ^{57}Fe ENDOR studies of this state.

3.8. Outlook of site-selective labeling

This chapter discussed the application of site-selective labeling to study M^{OX}, E_1, and E_4(4H). However, in principle any intermediate (like the ones discussed in Chapter 1) can be studied using site-selective labeling; and in doing so determine the valence and spin orientation of the labeled Fe site. Furthermore, its utilization does not have to be limited to intermediates of biological N_2 fixation, but also catalytically related states such as the protonated,[50] cyroreduced,[17, 34-35] and π-acid bound states of FeMo-co.[31, 51-52] These states may not be catalytically relevant intermediates, but they can provide insights into various aspects of the mechanism of biological N_2 fixation.

3.9. Supplementary information

3.9.1. Analysis of the zero-field M^{OX} Mössbauer data

Simulation of the NifDK–M($^{57}Fe_1$), NifDK–M($^{57}Fe_7$), and NifDK–M($^{57}Fe_6$) spectra in the M^{ox} state at 4.7 K and 80 K.

The simulation of the Mössbauer spectra of the NifDK–M($^{57}Fe_1$), NifDK–M($^{57}Fe_7$), and NifDK–M($^{57}Fe_6$) spectra in the M^{OX} state were conducted almost identically to the simulations of the analogous spectra in the M^{N} state discussed in Chapter 2, section 2.7.4. The only difference is that the Fe1 site was modeled as a single quadrupole doublet at 80 K.

The relative area contributions for each group of Fe sites for each data set are described in the simulation of the variable temperature NifDK–M($^{57}Fe_1$) spectra and the simultaneous simulation of the NifDK–M($^{57}Fe_7$), and NifDK–M($^{57}Fe_6$) spectra in the M^{N} state as discussed in Chapter 2, section 2.7.4.

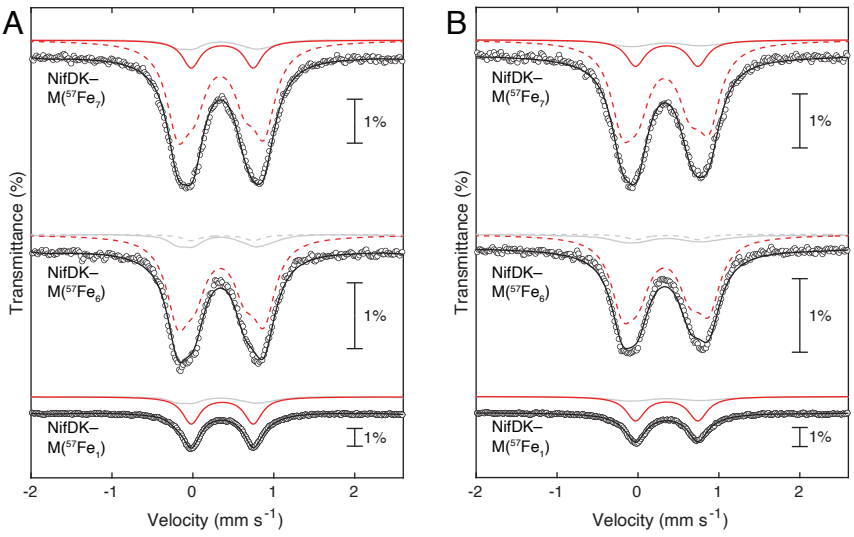

Figure S3.1. Zero-field Mössbauer spectra of the NifDK–M($^{57}Fe_7$), NifDK–M($^{57}Fe_6$), and NifDK–M($^{57}Fe_1$) in the M^{OX} state. A, 4.7 K data and **B,** 80 K data. Circles are the experimental data; black traces are the total simulations; solid red traces are the simulations for the Fe1 site enriched with ^{57}Fe; dotted red traces are the simulations for the belt Fe sites enriched with ^{57}Fe; dotted gray traces are the simulations for the Fe1 site enriched with natural abundance ^{57}Fe; solid gray traces are the corresponding NifDK–P($^{57}Fe_8$)–M($^{57}Fe_7$) spectra scaled to account for the natural-abundance ^{57}Fe contribution from the 15 Fe sites. Note that a minor high-spin Fe^{2+} site has been subtracted from the NifDK–M($^{57}Fe_1$) spectra.

Table S3.1. The individual Mössbauer parameters for the belt sites in the M^{ox} state at 4.7 K and 80 K.

	4.7 K		80 K	
	Doublet 1	Doublet 2	Doublet 1	Doublet 2
δ (mm s^{-1})	0.34	0.33	0.34	0.32
$\lvert\Delta E_Q\rvert$ (mm s^{-1})	1.06	0.61	1.07	0.64
Γ (mm s^{-1})	0.34	0.33	0.34	0.36
Rel. Area (%)	64.0	36.0	55.2	44.8

Table S3.2. The 4.7 K and 80 K Mössbauer parameters for the M($^{57}Fe_7$), belt, and Fe1 sites in the M^{ox} state.

	4.7 K			80 K		
	M($^{57}Fe_7$)[a]	Belt[a]	Fe1	M($^{57}Fe_7$)[a]	Belt[a]	Fe1
δ (mm s^{-1})	0.34	0.34	0.36	0.34	0.33	0.36
$\lvert\Delta E_Q\rvert$ (mm s^{-1})	0.88	0.90	0.77	0.87	0.88	0.77
Γ (mm s^{-1})	-	-	0.26	-	-	0.28

[a]Reported as a weighted average.

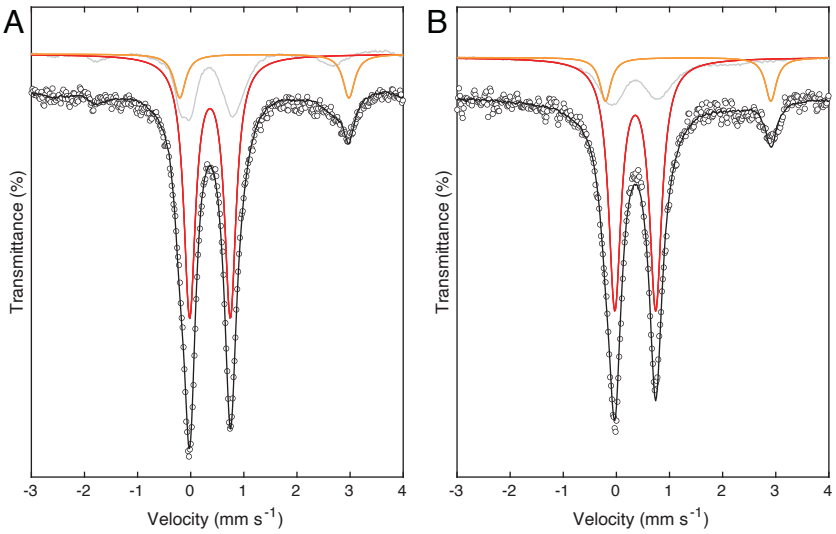

Figure S3.2. Zero-field Mössbauer spectra of NifDK–M(^{57}Fe$_1$) in the M^{OX} state. A, 4.7 K data **B,** 80 K data. Circles are the experimental data; black traces are the total simulations; solid red traces are the simulations for the Fe1 site enriched with ^{57}Fe; gray traces are the corresponding NifDK–P(^{57}Fe$_8$)–M(^{57}Fe$_7$) spectra scaled to account for the natural-abundance contribution from the 15 Fe sites; orange traces are the simulations for mononuclear Fe^{2+}.

Table S3.3. Zero-field Mössbauer parameters for the NifDK–M(^{57}Fe$_1$) sample in the M^{OX} state.

	4.7 K		**80 K**	
	Fe1	Fe^{2+}	Fe1	Fe^{2+}
δ (mm s^{-1})	0.36	1.38	0.36	1.36
$\lvert\Delta E_Q\rvert$ (mm s^{-1})	0.77	3.18	0.77	3.12
Γ (mm s^{-1})	0.26	0.27	0.28	0.25
Rel. Area (%)	63.7	8.1	63.0	8.1

3.9.2. Metal analysis of the pre- and post-turnover (high-flux) NifDK–M($^{57}Fe_1$) samples

To assess if the ^{57}Fe label is lost during turnover, we compared the ratio of ^{57}Fe:^{56}Fe between the pre- and post-turnover samples as assessed by ICP-MS analysis (Eq. (16)). A value of r that is lower than 1 indicates that the label from the Fe1 site is lost during turnover.

$$r = \frac{\frac{^{57}Fe_{Post}}{^{56}Fe_{Post}}}{\frac{^{57}Fe_{Pre}}{^{56}Fe_{Pre}}} \quad (16)$$

For our high-flux turnover sample, we calculate r = 0.96 ± 0.05, and we therefore conclude that exogenous Fe is not scrambling into the Fe1 site during turnover.

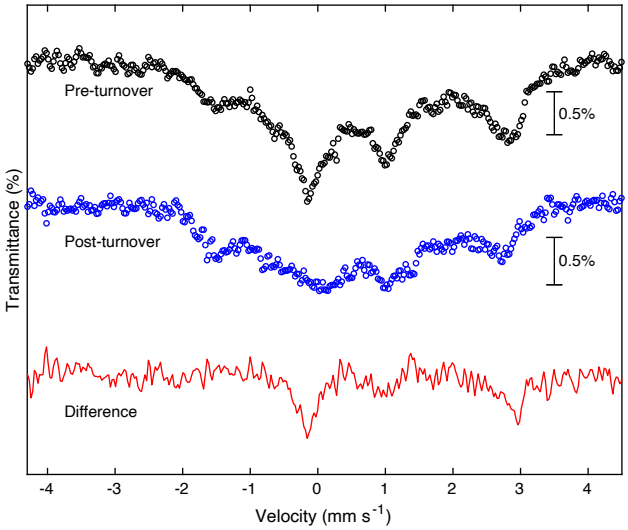

Figure S3.3. Mössbauer spectra of the NifDK–M($^{57}Fe_1$) sample pre- and post-turnover (high-flux) at 5 K in the presence of a 77 mT external field oriented parallel perpendicular to the incident radiation. Circles are the experimental data. Note the features from mononuclear Fe^{2+} present in the pre-turnover sample (at approximately –0.2 and 3 mm s^{-1}) are absent in the post-turnover sample, as is clear in the difference spectrum.

3.9.3 Analysis of NifDK Mössbauer spectra under low-flux turnover

Analysis of the NifDK Mössbauer spectra under low-flux turnover at 5 K, 77 mT

General Considerations

The analysis of Mössbauer spectra of the Mo nitrogenase in the E_1 state has been previously reported.[17, 35] The E_1 state was generated under low-flux turnover conditions as a mixture of E_0 and E_1 (see Experimental and Methods). The yield of E_1 was determined using a previously reported method:[17, 35] by measuring the loss of intensity of the M^N EPR signal at g_1. Fig. S3.4 and S3.5 show the EPR spectra of the NifDK–M($^{57}Fe_7$) and NifDK–M($^{57}Fe_1$) before and during low-flux turnover. Based on this analysis, the yields of E_1 for the NifDK–M($^{57}Fe_7$) and NifDK–M($^{57}Fe_1$) samples were 43 and 44%, respectively (~40% for both, given the uncertainty in the spin quantification). Because FeMo-co in the M^R state is an integer spin system,[17] the Fe sites in this state appear as sharp quadrupole doublets at low temperatures, while the doublets arising from FeMo-co in M^N are magnetically split. Thus, the signals arising from the two states are readily distinguishable.

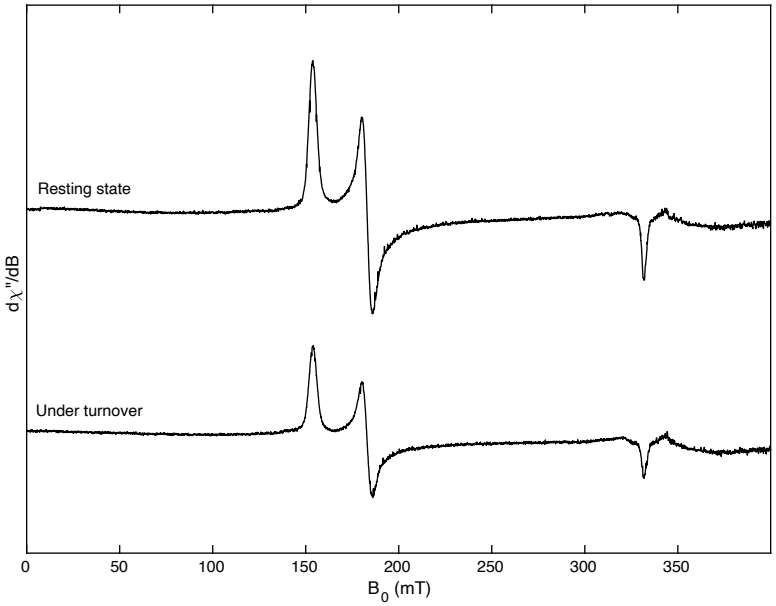

Figure S3.4. EPR spectra of the NifDK–M($^{57}Fe_7$) Mössbauer sample before and under turnover. Recorded at 9.37 GHz, 5 K, and 1 mW.

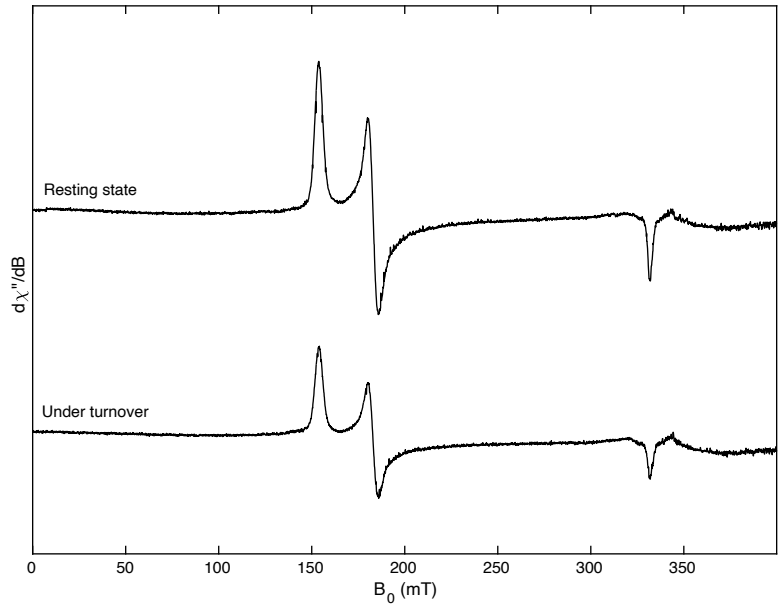

Figure S3.5. EPR spectra of the NifDK–M($^{57}Fe_1$) Mössbauer sample before and under turnover. Recorded at 9.37 GHz, 5 K, and 1 mW.

Analysis of the NifDK–M($^{57}Fe_7$) Mössbauer spectra in the M^R state at 5 K, 77 mT

To analyze the Mössbauer spectrum of the NifDK–M($^{57}Fe_7$) in M^R, the following assumptions were made in addition to the ones discussed in Chapter 2, section 2.7.4 to simulate FeMo-co in M^N:

(1) The spectrum only contains contributions from the two states of FeMo-co: M^N and M^R. While the FeP is present and contains natural abundance ^{57}Fe, its concentration is sufficiently low enough to assume it contributes negligibly to the total spectrum (~0.02 % of the total spectrum).

(2) E_0 accounts for 57% of the total spectrum, based on the EPR analysis.

(3) In E_1, the P-cluster is in the P^N state.[53]

The contributions from E_0 can be removed by subtracting the corresponding NifDK–M($^{57}Fe_7$) E_0 spectrum, normalizing its contribution to 57% of the total spectrum. The contribution from the P-cluster in E_1 can be determined using the following ratio

$$\frac{A_{Fe7}}{A_{Pclu}} = \frac{R_{label} \cdot 7}{R_{NA} \cdot 8} \quad (16)$$

where A_{Fe7} and A_{Pclu} represent the spectral area contributed by FeMo-co and the P-cluster in E_1, R_{label} is the mole fraction of ^{57}Fe in all enriched Fe sites (in this case all the Fe sites of FeMo-co), and R_{NA} is the natural abundance of ^{57}Fe. The spectrum of the P-cluster used in this analysis was prepared by subtracting the corresponding NifDK–M($^{57}Fe_7$) spectrum in the M^N state from the NifDK–P($^{57}Fe_8$)–M($^{57}Fe_7$) spectrum (Fig. S3.6). Removing the contributions from the Fe sites in E_0 and the natural abundance Fe from the P-cluster in E_1 leaves only the quadrupole doublets from FeMo-co in the M^R state (Fig. S3.7, bottom). The use and simulation of this data will be discussed in later sections.

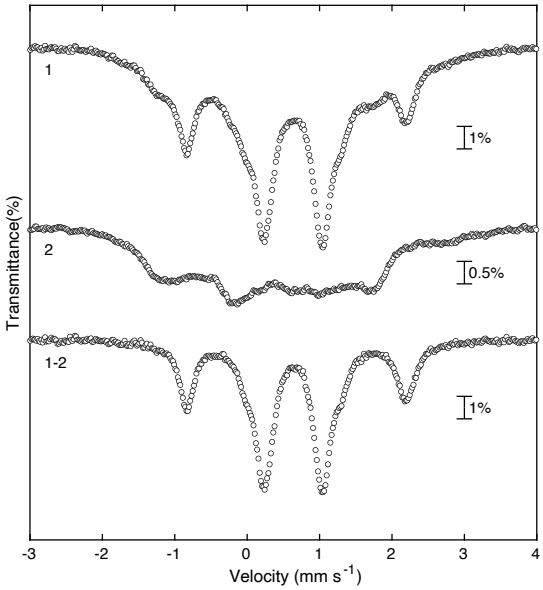

Figure S3.6. Spectral deconvolution of the NifDK–P($^{57}Fe_8$)–M($^{57}Fe_7$) in the spectrum in M^N at 4.7 K in the presence of a 77 mT external magnetic field (perpendicular). Top: NifDK–P($^{57}Fe_8$)–M($^{57}Fe_7$) spectrum; Middle: NifDK–M($^{57}Fe_7$) spectrum; Bottom: Subtraction of middle spectrum from the top. The bottom spectrum represents the quadrupole doublets arising from the P-cluster in the P^N state. Circles are the experimental data.

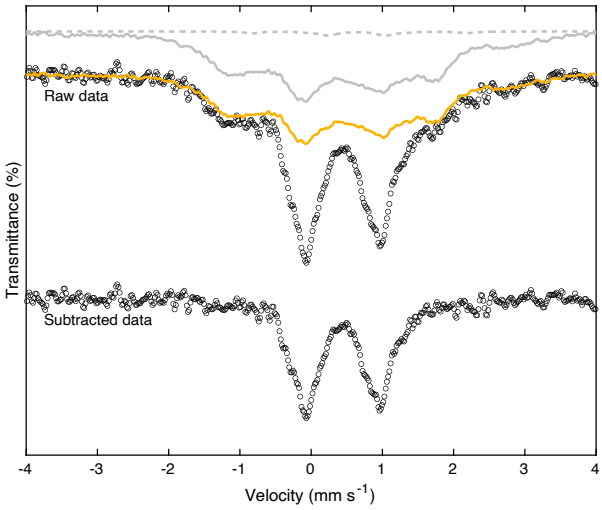

Figure S3.7. Mössbauer spectra of the NifDK–M($^{57}Fe_7$) sample under low-flux turnover conditions at 5 K in the presence of a 77 mT external magnetic field oriented perpendicular to the incident radiation. The top spectrum is the raw Mössbauer spectrum along with contributions from E_0 (solid gray line), and the P-cluster in the P^N state (dotted gray line). The yellow solid line is the sum of the latter two contributions. Circles are the experimental data. The bottom spectrum represents FeMo-co in the M^R state—all contributions from E_0 and natural abundance P-cluster have been removed.

Analysis of the NifDK–M($^{57}Fe_1$) Mössbauer spectra in the M^R state at 5 K, 77 mT

To simulate the Mössbauer spectrum of the NifDK–M($^{57}Fe_1$) under low-flux turnover, the following assumptions were made in addition to the ones discussed in the previous section:

(1) The contributions from the FeP are negligible (~0.1 % of the total spectrum).

(2) E_0 accounts for 56% of the total Mössbauer spectrum, based on the EPR analysis (Fig. S3.4).

(3) The Fe sites of FeMo-co do not scramble under turnover (see prior experiments) and therefore the labeling efficiency can be used to fix the relative contributions between the Fe1 site and the natural abundance contributions from all other sites in the E_1 state.

Like the analysis of the NifDK–M($^{57}Fe_7$) spectrum, the NifDK–M($^{57}Fe_1$) low-flux turnover sample contains contributions from Fe sites that are in the E_0 and E_1 states. The contributions from E_0 were removed by subtracting the corresponding NifDK–M($^{57}Fe_1$) spectrum normalized to 56% of the total spectrum. The contribution from natural abundance Fe sites in the E_1 state were removed by subtracting the Mössbauer spectra of the P-cluster and FeMo-co derived in the previous section (note that the addition of these two spectra effectively creates the NifDK–P($^{57}Fe_8$)–M($^{57}Fe_7$) Mössbauer spectrum in E_1). The total area contribution of the Fe1 site in the M^R state and the natural abundance Fe sites were determined as previously discussed for simulations of M^{OX} and M^N.

Once all the contributions from E_0 and the natural abundance ^{57}Fe sites from E_1 were removed, the NifDK–M($^{57}Fe_1$) spectrum was simulated using a single quadrupole doublet with the following free variables

1) Isomer shift of quadrupole doublet for the Fe1 site
2) Quadrupole splitting of quadrupole doublet for Fe1 site
3) Linewidth of quadrupole doublet for the Fe1 site

The simulations and parameters are presented in the main text (Fig. 3.3).

Table S3.4. The 5 K Mössbauer parameters for the Fe1 site in the M^R state.

	Fe1
δ (mm s^{-1})	0.53
$\lvert\Delta E_Q\rvert$ (mm s^{-1})	1.54
Γ (mm s^{-1})	0.36

[a]Reported as a weighted average.

3.9.4 Additional data

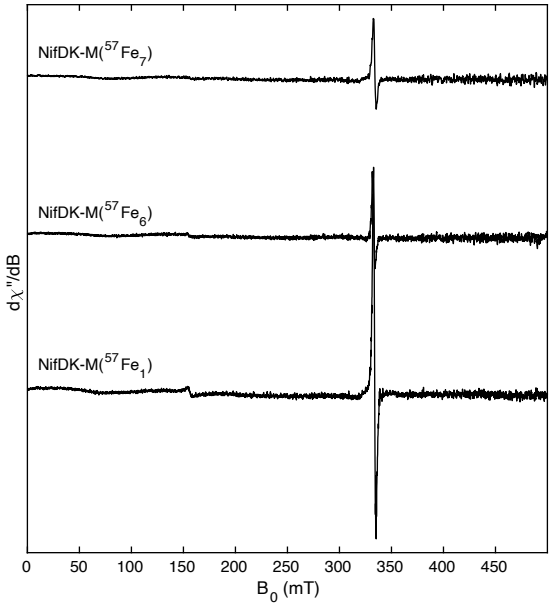

Figure S3.8. EPR spectra of PMS-oxidized NifDK–M($^{57}Fe_7$), NifDK–M($^{57}Fe_6$), and NifDK–M($^{57}Fe_1$). EPR spectra were acquired at 9.37 GHz, 5 K, and 1 mW. The sharp isotropic signal arises from the oxidant, PMS.

Table S3.5. The 4.2 K Mössbauer isomer shifts for Fe sites in different protein-bound Fe–S clusters as compiled by Pandelia *et al*.[7]

	$[Fe_4S_4]^{3+}$		$[Fe_4S_4]^{2+}$	$[Fe_4S_4]^{1+}$	
	Fe^{3+}	$Fe^{2.5+}$	$Fe^{2.5+}$	$Fe^{2.5+}$	Fe^{2+}
δ (mm s^{-1})	0.29	0.40	0.42	0.49	0.58

Table S3.6. The differences in Mössbauer isomer shifts for Fe sites at 4.2 K for various protein-bound Fe–S clusters in different redox states.[7]

	$[Fe_4S_4]^{3+} \rightarrow [Fe_4S_4]^{2+}$	$[Fe_4S_4]^{2+} \rightarrow [Fe_4S_4]^{1+}$	$[Fe_4S_4]^{1+} \rightarrow [Fe_4S_4]^{0}$
$\Delta\delta$ for Fe^{2+} and $Fe^{2.5+}$ (mm s^{-1})	-	0.16	0.16
$\Delta\delta$ for $Fe^{2.5+}$ and Fe^{3+} (mm s^{-1})	0.13	-	-

3.10. Experimental and Methods

TD1 Generation

The generation of the *Azotobacter vinelandii* strain that produces V70I apo-NifDK was adapted from previous reports. DJ1373 (produces His-tagged V70I NifDK) was streaked on a Burk's minimal medium (–Mo) plate; this step was repeated once more. Then, a 250 mL flask containing 50 mL of Burk's minimal medium (–Fe/Mo) media was inoculated. The culture was incubated at 30 °C, 180 RPM, until it exhibited a distinct flourescent green color—this typically takes about a day. After about a day, 200 µL of the culture, 200 µL of buffer (20 mM MOPS pH 7.2 and 20 mM $MgSO_4$), and 5 µL of an aqueous stock solution of the plasmid containing the comprimised *nifB* sequence (pdb218 at 1 µg/µL)[44] was incubated together for 20 minutes before plated on multiple BN (+KAN) at different dilutions (1:10, 1:100, and 1:1000). Plates were incubated at 30 °C until single colonies were visible (typically after 48 hours). Single colonies were tested for kanamycin resistance and their ability to test for nitrogen fixation.

Cell growth

The *Azotobacter vinelandii* strains DJ1141 (produces His-tagged NifDK), DJ1143 (produces His-tagged apo-NifDK), TD1, and wild-type (WT) *A. vinelandii* were cultured in 18 L batches in a 20 L B. Braun Biostat C bioreactor using Burk's minimal medium (6 mM sucrose, 0.9 mM $MgSO_4 \cdot 7H_2O$, 0.6 mM $CaCl_2 \cdot 2H_2O$, 18 µM $FeSO_4 \cdot 7H_2O$, 2 mM KH_2PO_4, 2 mM KH_2PO_4, 5 mM KH_2PO_4) supplemented with 1 µM $Na_2MoO_4 \cdot 2H_2O$.

For overproducing holo-NifDK and apo-NifDK, growths were supplemented with 6 mM ammonium acetate (BN media). Derepression was initiated upon ammonium depletion, and cells were harvested after 3 hours.[54] Cell paste was flash-frozen in LN_2 and stored at –80 °C until purification.

^{57}Fe-enriched NifDK protein was generated using identical protocols to what was described above except that the Fe source was generated by dissolving ^{57}Fe powder (Trace Science International, 95.5% enrichment) with stoichiometric H_2SO_4.

NifDK purification

All NifDK purification procedures were carried out in a Coy Labs glove box (<5 ppm O_2). All aqueous solutions used were sparged with N_2 overnight. Cells were lysed using the osmotic shock method as followed: DJ1141 cell paste was resuspended with 3 mL of 25 mM HEPES pH 7.5, 50% glycerol, and 2 mM sodium dithionite (DTH) for every gram of cell paste. After stirring at room temperature for 15 minutes, the cells were pelleted at 25,000 × g for 15 minutes. The supernatant was poured off and the pelleted cells were resuspended with 3 mL buffer containing 25 mM HEPES pH 7.5, 2 mM sodium dithionite, 3 mM phenylmethylsulfonyl fluoride (PMSF), 1 mg/mL lysozyme, and 100 µg/mL DNase I for every gram of cell paste. After 15 minutes of stirring, the lysate was pelleted at 100,000 × g for 1 hr and loaded onto a Co-NTA column equilibrated with buffer containing 500 mM NaCl, 25 mM HEPES pH 7.5, 20% glycerol, and 2 mM DTH. The immobilized protein was washed with 10 column volumes of equilibration buffer and eluted with equilibration buffer containing 200 mM imidazole. NifDK was further purified using anion exchange chromatography: the protein solution was diluted 4-fold with buffer containing 25 mM HEPES pH 7.5, 20% glycerol, and 2 mM DTH and then loaded onto a DEAE-sepharose column charged with NaCl and equilibrated with the dilution buffer. The column was washed with 10 column volumes of 160 mM NaCl, 25 mM HEPES pH 7.5, 2 mM DTH, and 20% glycerol. The immobilized protein was then eluted with buffer containing 500 mM NaCl, 25 mM HEPES pH 7.5, 2 mM DTH, and 20% glycerol. Purified NifDK was concentrated using an AMICON stirred cell equipped with a 30 kDa filter, flash-frozen, and stored in LN_2. The concentration of NifDK was estimated by determining the Mo content using inductively coupled plasma mass spectrometry (ICP-MS).

Note: In our study, the reported concentration of NifDK is based on the αß heterodimer concentration (with one FeMo-co per heterodimer in holo-NifDK) rather than the $\alpha_2ß_2$ heterotetramer concentration (with two FeMo-co per heterotetramer in holo-NifDK).

NifH purification

The purification of NifH was carried out in an MBRAUN glove box (<5 ppm O_2) and was performed similarly to what has been previously reported.[55] WT *A. vinelandii* cell paste was lysed as described above. Lysate was loaded onto a DE-52 column charged with NaCl and equilibrated in 25 mM HEPES pH 7.5 and 2 mM DTH. The column was washed with a stepwise gradient with buffer containing 125 mM, 200 mM, 300 mM, and 500 mM NaCl. Fractions were analyzed by EPR spectroscopy; those determined to have NifH were pooled and concentrated using a DE-52 cellulose column and AMICON spin filters equipped with a 10 kDa filter. NifH was then purified further using an Superdex 200 column equilibrated with buffer containing 200 mM NaCl, 25 mM HEPES pH 7.5, and 2 mM DTH. Purified NifH was subsequently concentrated and flash-frozen in LN_2. The concentration of NifH was estimated by UV-vis spectroscopy.[55]

Isolation of FeMo-co

The protocol for FeMo-co isolation was adapted from a previously reported procedure.[56] Protein manipulation was performed in a Coy Labs glove box (<5 ppm O_2) and FeMo-co manipulation was carried out in an MBRAUN or Vacuum Atmospheres glove box (<5 ppm O_2). NifDK (typical protein concentrations ranging from 100 to 400 μM αß dimer) was diluted 10-fold with aqueous 2 mM DTH. The protein was denatured by the addition of 100 mM citric acid (1.67 mL per 10 mL of diluted protein) added dropwise at 0 ˚C with stirring. After incubating the mixture for 30 s the protein was precipitated by addition of 200 mM Na_2HPO_4 (1.7 mL per 10 mL of diluted protein). The precipitated protein was transferred to a 15 mL conical tube and moved to the Mbraun box where the protein was pelleted at 120 × g for 5 min using a Labnet Z100A centrifuge. The supernatant was removed and the pellet was washed with *N,N*-dimethylformamide (DMF) (5 mL) and pelleted. This DMF wash step was performed once more. FeMo-co was then extracted by resuspending and vortexing the pellet with 1 to 2 mL of *N*-methylformamide (NMF) containing 2 mM Na_2HPO_4 (from a 200 mM aqueous stock solution). After a 5-minute incubation at room temperature, the extract

was centrifuged at 500 × g for 5 minutes, and the brown supernatant was poured off and collected. The process was repeated until the solution was colorless, and the extracts were combined. The concentration of FeMo-co was estimated by UV-vis spectroscopy using an extinction coefficient of PhS-bound FeMo-co in NMF: 14,800 M^{-1} cm^{-1} at 450 nm (See Chapter 2).

Post-biosynthetic isotope editing of FeMo-co

Isolated FeMo-co (either ^{57}Fe-enriched or natural-abundance) was treated with 30 equiv ethylenediaminetetraacetic acid (EDTA) (added as a 100 mM aqueous stock solution) and stirred at room temperature for 5 minutes. Then 35 equiv $FeCl_2$ (either natural-abundance or ^{57}Fe-enriched) was added (as a 100 mM stock solution in 50% v/v NMF/H_2O), and the solution was stirred for 3 minutes at room temperature. Prolonged incubation of EDTA-treated FeMo-co with $FeCl_2$ can lead to the appearance of an unidentified $S = {}^5/_2$ EPR signal (g_{eff} = 4.3). However, samples with this signal are competent for insertion of FeMo-co into apo-NifDK, and as such the reaction with excess $FeCl_2$ appears to be reversible.

Insertion of FeMoco into apo-NifDK protein

The procedure for inserting FeMo-co onto apo-NifDK protein was adapted from previous reports.[44, 57] Excess as-isolated or postbiosynthetically modified FeMo-co (up to 1.5 equiv) was added dropwise to freshly prepared crude lysate of DJ1143 (lysed using osmotic shock), stirred at room temperature. The final concentration of NMF was approximately 1% v/v. Once FeMo-co addition was complete, the now holo-NifDK protein was purified as described above with an additional step. Following anion exchange chromatography, the NifDK protein was applied to a Superdex 200 column equilibrated in 500 mM NaCl, 25 mM HEPES pH 7.5, 20% glycerol, and 2 mM DTH. Fractions containing NifDK protein were pooled and concentrated. We estimated the yield of apo-NifDK isolated from fixed amount of DJ1143 cell paste or ΔB DJ1373 cell paste.

Mössbauer sample preparation

Samples were poised in the M^{OX} state by initial treatment with 500 μM indigodisulfonate (IDS) and gel filtration into 500 mM NaCl, 25 mM HEPES pH 7.5, and 20% glycerol using a PD-10 column (GE Healthcare). Following gel-filtration, the NifDK sample was fully oxidized by incubating with at least 7 equiv phenazine methosulfate (PMS) (based on Mo concentration) for 3 minutes before freezing in LN_2. Samples containing the turnover state E_1 were generated under low electron flux using a ratio of 100:1 NifDK:NifH. The Mössbauer samples were prepared under an atmosphere of N_2 in the presence of 5 mM ATP, 5 mM $MgCl_2$, 20 mM phosphocreatine, 30 mM sodium dithionite, and 25 U per mL of creatine kinase. NifH was added to initiate turnover and the sample was freeze-quenched in LN_2 after approximately 5 minutes. The yield of E_1 was determined by the loss of the resting state EPR signal of NifDK as determined by CW EPR spectroscopy (Fig. S12 and S13).

The post-turnover (high-flux) sample was prepared by subjecting the NifDK–M($^{57}Fe_1$) Mössbauer to turnover conditions for 30 min. under N_2. The sample was diluted to 20 μM with storage buffer that contained 5 mM $MgCl_2$, 5 mM ATP, 20 mM phosphocreatine, 30 mM sodium dithionite, and 25 U per mL creatine kinase. Turnover was initiated by addition NifH to a final concentration of 20 μM; this ratio of components corresponds to high-flux turnover conditions.[40] After 30 minutes, the sample was purified using IMAC and gel-filtered into storage buffer before being flash-frozen in LN_2.

Spectroscopy and spectrometry

Zero-field ^{57}Fe-Mössbauer spectra were recorded with a constant acceleration spectrometer equipped with a JANIS closed cycle He gas refrigerator cryostat. Isomer shifts were quoted relative to α-Fe foil at room temperature. EPR samples were prepared in an anaerobic glove box with an N_2 atmosphere and an O_2 level of <5 ppm. X-band EPR spectra were recorded on a Bruker EMX spectrometer at 9.37 GHz. Q-band ENDOR data were collected using a locally constructed spectrometer.[58] Inductively coupled plasma mass spectrometer (ICP-MS) data were recorded on an Agilent 7900 ICP-MS instrument. Protein samples were digested with concentrated

nitric acid (TraceMetal Grade, Fischer) at 70 °C and were diluted with Milli-Q water to final concentration of 2% nitric acid. Standards for Mo were prepared from a 1000 ppm standard solution (VWR BDH Chemicals). Standards for Fe and ^{56}Fe were prepared from a 1000 ppm standard solution (SPEX Certiprep). Standards for ^{57}Fe were prepared as described previously.[59] The concentrations of ^{56}Fe and ^{57}Fe in the standard solutions were based on the natural abundance of each isotope in the unenriched standard (91.7% ^{56}Fe, 2.12% ^{57}Fe) and the isotope enrichment in ^{57}Fe powder (95.5% ^{57}Fe, 3.6% ^{56}Fe).

3.10. References

1. Winter, H. C. & Burris, R. H., Nitrogenase. *Annual Review of Biochemistry* **1976,** *45* (1), 409-426.
2. Burgess, B. K. & Lowe, D. J., Mechanism of Molybdenum Nitrogenase. *Chemical Reviews* **1996,** *96* (7), 2983-3012.
3. Hoffman, B. M., Lukoyanov, D., Yang, Z.-Y., Dean, D. R. & Seefeldt, L. C., Mechanism of Nitrogen Fixation by Nitrogenase: The Next Stage. *Chemical Reviews* **2014,** *114* (8), 4041-4062.
4. Van Stappen, C., et al., The Spectroscopy of Nitrogenases. *Chemical Reviews* **2020,** *120* (12), 5005-5081.
5. Einsle, O. & Rees, D. C., Structural Enzymology of Nitrogenase Enzymes. *Chemical Reviews* **2020,** *120* (12), 4969-5004.
6. Seefeldt, L. C., et al., Reduction of Substrates by Nitrogenases. *Chemical Reviews* **2020,** *120* (12), 5082-5106.
7. Pandelia, M.-E., Lanz, N. D., Booker, S. J. & Krebs, C., Mössbauer spectroscopy of Fe/S proteins. *Biochimica et Biophysica Acta (BBA) - Molecular Cell Research* **2015,** *1853* (6), 1395-1405.
8. Spatzal, T., et al., Evidence for Interstitial Carbon in Nitrogenase FeMo Cofactor. *Science* **2011,** *334* (6058), 940.
9. Lovell, T., Li, J., Liu, T., Case, D. A. & Noodleman, L., FeMo Cofactor of Nitrogenase: A Density Functional Study of States M^N, M^{OX}, M^R, and M^I. *Journal of the American Chemical Society* **2001,** *123* (49), 12392-12410.
10. Harris, T. V. & Szilagyi, R. K., Comparative Assessment of the Composition and Charge State of Nitrogenase FeMo-Cofactor. *Inorganic Chemistry* **2011,** *50* (11), 4811-4824.
11. Siegbahn, P. E. M., Model Calculations Suggest that the Central Carbon in the FeMo-Cofactor of Nitrogenase Becomes Protonated in the Process of Nitrogen Fixation. *Journal of the American Chemical Society* **2016,** *138* (33), 10485-10495.
12. Bjornsson, R., Neese, F. & DeBeer, S., Revisiting the Mössbauer Isomer Shifts of the FeMoco Cluster of Nitrogenase and the Cofactor Charge. *Inorganic Chemistry* **2017,** *56* (3), 1470-1477.
13. Benediktsson, B. & Bjornsson, R., QM/MM Study of the Nitrogenase MoFe Protein Resting State: Broken-Symmetry States, Protonation States, and QM Region Convergence in the FeMoco Active Site. *Inorganic Chemistry* **2017,** *56* (21), 13417-13429.
14. Raugei, S., Seefeldt, L. C. & Hoffman, B. M., Critical computational analysis illuminates the reductive-elimination mechanism that activates nitrogenase for N_2 reduction. *Proceedings of the National Academy of Sciences* **2018,** *115* (45), E10521.
15. Li, Z., Li, J., Dattani, N. S., Umrigar, C. J. & Chan, G. K.-L., The electronic complexity of the ground-state of the FeMo cofactor of nitrogenase as relevant to quantum simulations. *The Journal of Chemical Physics* **2019,** *150* (2), 024302.
16. Zimmermann, R., et al., Nitrogenase X: Mössbauer and EPR studies on reversibly oxidized MoFe protein from *Azotobacter vinelandii* OP. Nature of the iron

centers. *Biochimica et Biophysica Acta (BBA) - Protein Structure* **1978,** *537* (2), 185-207.
17. Yoo, S. J., Angove, H. C., Papaefthymiou, V., Burgess, B. K. & Münck, E., Mössbauer Study of the MoFe Protein of Nitrogenase from *Azotobacter vinelandii* Using Selective ^{57}Fe Enrichment of the M-Centers. *Journal of the American Chemical Society* **2000,** *122* (20), 4926-4936.
18. Johnson, M. K., Thomson, A. J., Robinson, A. E. & Smith, B. E., Characterization of the paramagnetic centres of the molybdenum-iron protein of nitrogenase from *Klebsiella pneumoniae* using low temperature magnetic circular dichroism spectroscopy. *Biochimica et Biophysica Acta (BBA) - Protein Structure* **1981,** *671* (1), 61-70.
19. Smith, B. E. & Lang, G., Mössbauer spectroscopy of the nitrogenase proteins from Klebsiella pneumoniae. Structural assignments and mechanistic conclusions. *Biochemistry Journal* **1974,** *137* (2), 169-80.
20. Lindahl, P. A., Papaefthymiou, V., Orme-Johnson, W. H. & Münck, E., Mössbauer studies of solid thionin-oxidized MoFe protein of nitrogenase. *Journal of Biological Chemistry* **1988,** *263* (36), 19412-8.
21. Surerus, K. K., et al., Moessbauer and integer-spin EPR of the oxidized P-clusters of nitrogenase: P^{OX} is a non-Kramers system with a nearly degenerate ground doublet. *Journal of the American Chemical Society* **1992,** *114* (22), 8579-8590.
22. Igarashi, R. Y., et al., Trapping H- Bound to the Nitrogenase FeMo-Cofactor Active Site during H2 Evolution: Characterization by ENDOR Spectroscopy. *Journal of the American Chemical Society* **2005,** *127* (17), 6231-6241.
23. Seefeldt, L. C., Hoffman, B. M. & Dean, D. R., Mechanism of Mo-dependent nitrogenase. *Annual Review of Biochemistry* **2009,** *78*, 701-22.
24. Spatzal, T., Perez, K. A., Einsle, O., Howard, J. B. & Rees, D. C., Ligand binding to the FeMo-cofactor: structures of CO-bound and reactivated nitrogenase. *Science* **2014,** *345* (6204), 1620-3.
25. Lukoyanov, D., Barney, B. M., Dean, D. R., Seefeldt, L. C. & Hoffman, B. M., Connecting Nitrogenase Intermediates with the Kinetic Scheme for N_2 Reduction by a Relaxation Protocol and Identification of the N_2 Binding State. *Proceedings of the National Academy of Sciences* **2007,** *104* (5), 1451.
26. Doan, P. E., et al., ^{57}Fe ENDOR spectroscopy and 'electron inventory' analysis of the nitrogenase E_4 intermediate suggest the metal-ion core of FeMo-cofactor cycles through only one redox couple. *Journal of the American Chemical Society* **2011,** *133* (43), 17329-40.
27. Lukoyanov, D., et al., Identification of a Key Catalytic Intermediate Demonstrates That Nitrogenase Is Activated by the Reversible Exchange of N_2 for H_2. *Journal of the American Chemical Society* **2015,** *137* (10), 3610-3615.
28. Lukoyanov, D., et al., Reductive Elimination of H2 Activates Nitrogenase to Reduce the N≡N Triple Bond: Characterization of the E4(4H) Janus Intermediate in Wild-Type Enzyme. *Journal of the American Chemical Society* **2016,** *138* (33), 10674-10683.

29. Harris, D. F., et al., Mechanism of N_2 Reduction Catalyzed by Fe-Nitrogenase Involves Reductive Elimination of H_2. *Biochemistry* **2018,** *57* (5), 701-710.
30. Spatzal, T., Perez, K. A., Howard, J. B. & Rees, D. C., Catalysis-dependent selenium incorporation and migration in the nitrogenase active site iron-molybdenum cofactor. *Elife* **2015,** *4*, e11620.
31. Spatzal, T., Perez, K. A., Einsle, O., Howard, J. B. & Rees, D. C., Ligand binding to the FeMo-cofactor: Structures of CO-bound and reactivated nitrogenase. *Science* **2014,** *345* (6204), 1620-1623.
32. Lee, C. C., et al., Evidence of substrate binding and product release via belt-sulfur mobilization of the nitrogenase cofactor. *Nature Catalysis* **2022,** *5* (5), 443-454.
33. Sippel, D., et al., A bound reaction intermediate sheds light on the mechanism of nitrogenase. *Science* **2018,** *359* (6383), 1484-1489.
34. Van Stappen, C., Thorhallsson, A. T., Decamps, L., Bjornsson, R. & DeBeer, S., Resolving the structure of the E_1 state of Mo nitrogenase through Mo and Fe K-edge EXAFS and QM/MM calculations. *Chemical Science* **2019,** *10* (42), 9807-9821.
35. Van Stappen, C., et al., Spectroscopic Description of the E_1 State of Mo Nitrogenase Based on Mo and Fe X-ray Absorption and Mössbauer Studies. *Inorganic Chemistry* **2019,** *58* (18), 12365-12376.
36. Christiansen, J., Tittsworth, R. C., Hales, B. J. & Cramer, S. P., Fe and Mo EXAFS of Azotobacter vinelandii Nitrogenase in Partially Oxidized and Singly Reduced Forms. *Journal of the American Chemical Society* **1995,** *117* (40), 10017-10024.
37. Lukoyanov, D. A., et al., The One-Electron Reduced Active-Site FeFe-Cofactor of Fe-Nitrogenase Contains a Hydride Bound to a Formally Oxidized Metal-Ion Core. *Inorganic Chemistry* **2022,** *61* (14), 5459-5464.
38. Cao, L., Caldararu, O. & Ryde, U., Protonation and Reduction of the FeMo Cluster in Nitrogenase Studied by Quantum Mechanics/Molecular Mechanics (QM/MM) Calculations. *Journal of Chemical Theory and Computation* **2018,** *14* (12), 6653-6678.
39. Lukoyanov, D. A., et al., Electron Redistribution within the Nitrogenase Active Site FeMo-Cofactor During Reductive Elimination of H_2 to Achieve N≡N Triple-Bond Activation. *Journal of the American Chemical Society* **2020,** *142* (52), 21679-21690.
40. Harris, D. F., Yang, Z.-Y., Dean, D. R., Seefeldt, L. C. & Hoffman, B. M., Kinetic Understanding of N_2 Reduction versus H_2 Evolution at the E_4(4H) Janus State in the Three Nitrogenases. *Biochemistry* **2018,** *57* (39), 5706-5714.
41. Lukoyanov, D., Yang, Z.-Y., Dean, D. R., Seefeldt, L. C. & Hoffman, B. M., Is Mo involved in hydride binding by the four-electron reduced (E_4) intermediate of the nitrogenase MoFe protein? *Journal of the American Chemical Society* **2010,** *132* (8), 2526-2527.
42. Barney, B. M., Igarashi, R. Y., Dos Santos, P. C., Dean, D. R. & Seefeldt, L. C., Substrate Interaction at an Iron-Sulfur Face of the FeMo-cofactor during Nitrogenase Catalysis *. *Journal of Biological Chemistry* **2004,** *279* (51), 53621-53624.
43. Dos Santos, P. C., Molecular biology and genetic engineering in nitrogen fixation. *Methods in Molecular Biology* **2011,** *766*, 81-92.

44. Christiansen, J., Goodwin, P. J., Lanzilotta, W. N., Seefeldt, L. C. & Dean, D. R., Catalytic and biophysical properties of a nitrogenase Apo-MoFe protein produced by a *nifB*-deletion mutant of *Azotobacter vinelandii*. *Biochemistry* **1998,** *37* (36), 12611-23.
45. Burén, S., Jiménez-Vicente, E., Echavarri-Erasun, C. & Rubio, L. M., Biosynthesis of Nitrogenase Cofactors. *Chemical Reviews* **2020,** *120* (12), 4921-4968.
46. Page, W. J. & von Tigerstrom, M., Optimal conditions for transformation of Azotobacter vinelandii. *Journal of Bacteriology* **1979,** *139* (3), 1058-61.
47. Page, W. J. & von Tigerstrom, M., Induction of transformation competence in Azotobacter vinelandii iron-limited cultures. *Canadian Journal of Microbiology* **1978,** *24* (12), 1590-4.
48. Badding, E. D., Srisantitham, S., Lukoyanov, D. A., Hoffman, B. M. & Suess, D. L. M., Connecting the geometric and electronic structures of the nitrogenase iron–molybdenum cofactor through site-selective 57Fe labelling. *Nature Chemistry* **2023**.
49. Lukoyanov, D. A., et al., A Conformational Equilibrium in the Nitrogenase MoFe Protein with an α-V70I Amino Acid Substitution Illuminates the Mechanism of H2 Formation. *Faraday Discussions* **2023**.
50. Morrison, C. N., Spatzal, T. & Rees, D. C., Reversible Protonated Resting State of the Nitrogenase Active Site. *Journal of the American Chemical Society* **2017,** *139* (31), 10856-10862.
51. Cameron, L. M. & Hales, B. J., Investigation of CO Binding and Release from Mo-Nitrogenase during Catalytic Turnover. *Biochemistry* **1998,** *37* (26), 9449-9456.
52. Buscagan, T. M., Perez, K. A., Maggiolo, A. O., Rees, D. C. & Spatzal, T., Structural Characterization of Two CO Molecules Bound to the Nitrogenase Active Site. *Angewandte Chemie International Edition* **2021,** *60* (11), 5704-5707.
53. Seefeldt, L. C., et al., Energy Transduction in Nitrogenase. *Accounts of Chemical Research* **2018,** *51* (9), 2179-2186.
54. Lee, C.-C., Ribbe, M. W. & Hu, Y., Purification of Nitrogenase Proteins. In *Metalloproteins: Methods and Protocols*, Hu, Y., Ed. Springer New York: New York, NY, 2019; pp 111-124.
55. Burgess, B. K., Jacobs, D. B. & Stiefel, E. I., Large-scale purification of high activity *Azotobacter vinelandii* nitrogenase. *Biochimica et Biophysica Acta (BBA) - Enzymology* **1980,** *614* (1), 196-209.
56. Shah, V. K. & Brill, W. J., Isolation of an iron-molybdenum cofactor from nitrogenase. *Proceedings of the National Academy of Sciences* **1977,** *74* (8), 3249-53.
57. McLean, P. A., Papaefthymiou, V., Orme-Johnson, W. H. & Münck, E., Isotopic hybrids of nitrogenase. Mössbauer study of MoFe protein with selective ^{57}Fe enrichment of the P-cluster. *Journal of Biological Chemistry* **1987,** *262* (27), 12900-12903.
58. Davoust, C. E., Doan, P. E. & Hoffman, B. M., Q-Band Pulsed Electron Spin-Echo Spectrometer and Its Application to ENDOR and ESEEM. *Journal of Magnetic Resonance, Series A* **1996,** *119* (1), 38-44.
59. Srisantitham, S., Badding, E. D. & Suess, D. L. M., Postbiosynthetic modification of a precursor to the nitrogenase iron–molybdenum cofactor. *Proceedings of the National Academy of Sciences* **2021,** *118* (11), e2015361118.

Chapter 4: Site-selective incorporation of Co into FeMo-co

4.1. Insights to metalloprotein function using non-native metals

Organisms have evolved to use metallocofactors to execute a variety of functions such as the binding or sensing of small molecules (O_2, NO),[1-2] the activation of inert C–H bonds (P450s, radical SAM enzymes),[3-4] and reduction of inert gasses (N_2, CO_2, CO).[5-6] The reactivity of the metallocofactor within the protein active site is precisely tuned by modulating the metal's primary and secondary coordination sphere, or even the identity of the metal itself. This concept is beautifully demonstrated with the heme cofactor; the reactivity of the Fe center within the porphyrin can vary from binding and transporting O_2 to participation in inert C–H activation.[2, 4] In addition to tuning the environment of the active site, there are reports of introducing new reactivity through metal substitution of the Fe with alternative transition metals, such as Co[7-8] or Ir[9-10], which has enabled the development of biocatalysts that are chemo-, stereo-, and substrate-selective. Beyond introducing different reactivity, changes to the active site of these proteins can also provide significant mechanistic insights, such as Co substitution for heme-containing proteins,[11-17] or V substitution for non-heme α-ketoglutarate (α-KG) dependent oxygenases.[18-19] Due to the similarities between Fe and Co, Co substitution has been used to characterize various heme containing proteins through EPR and UV-vis spectroscopy, providing direct insight into the primary coordination sphere of the metal site, such as the identity of the axial ligand or the chemistry of O_2 binding.[11-17] For non-heme α-KG dependent oxygenases, substitution of Fe for the stable vanadyl ion[18-19] has enabled EPR and crystallographic studies that have provided insight into the selectivity of the active Fe(IV)-oxo intermediate.

Inspired by these ideas, we set out to develop a strategy for manipulating the chemical composition of nitrogenase cofactors in an atomically precise manner to expand the toolbox for studying these complex enzymes (Fig. 4.1A). Our previous studies[20-21] focused on isotopically enriching a single site with ^{57}Fe within nitrogenase cofactors by

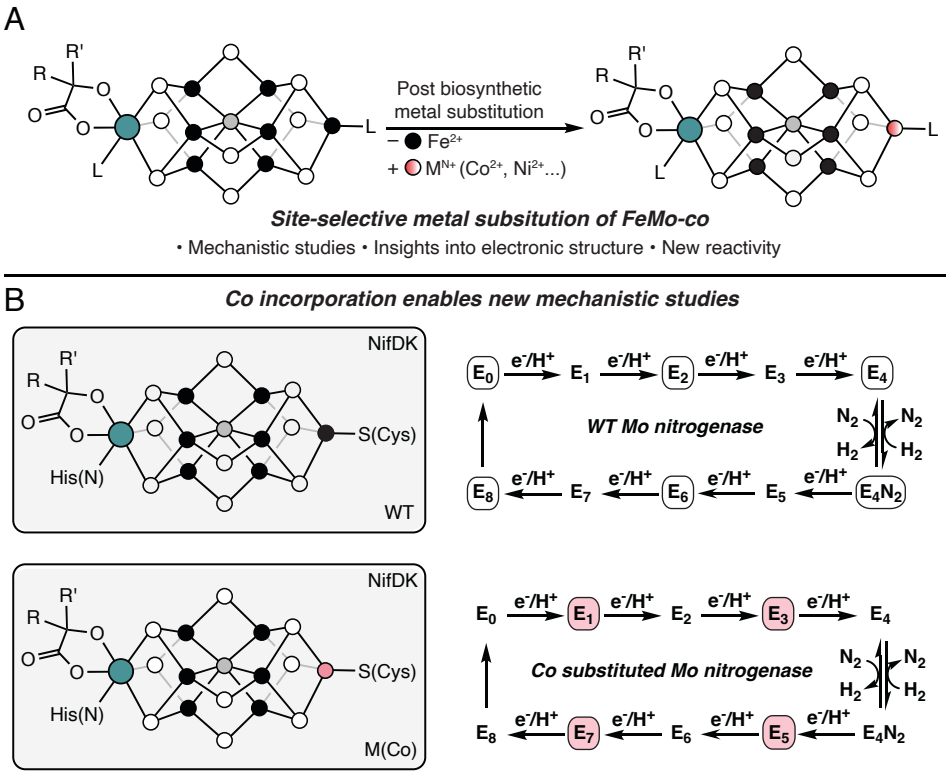

Figure 4.1. Applications of site-selective metal substitution of FeMo-co. A, The development of site-selective metal substitution of the Fe1 site of FeMo-co enables new mechanistic studies, insights into the electronic structure of FeMo-co and other nitrogenase cofactors, and introduce new reactivity. **B,** Site-selective substitution of Fe with Co enables new mechanistic studies of the Mo nitrogenase; E_n (n = odd integer) intermediates of nitrogen fixation would be EPR active in the Co substituted Mo nitrogenase. Highlighted states are EPR active. Black, white, gray, teal, and pink circles represent Fe, S, C, Mo, and Co, respectively. R,-$CH_2CO_2^-$; R′, -$(CH2)_2CO_2$.

leveraging the lability of their terminal Fe sites in their respective isolated state, particularly in the presence of a metal chelator such as ethylenediaminetetraacetic acid (EDTA). We envisioned applying this idea to incorporate various transition metals that behave similarly to Fe (*e.g.*, adopt a tetrahedral geometry and are roughly similar in size). Because of its previous use as spectroscopic probe in Fe containing enzymes, we first sought to substitute the terminal Fe site of FeMo-co with Co. When in the same charge state, Co has one more electron than Fe, and thus we rationalized that its incorporation into FeMo-co would enable new spectroscopic studies of the Mo nitrogenase. Upon Co substitution, states of FeMo-co that contain an even number of electrons would now

contain an odd number of electrons, and therefore these states would be amenable to characterization using EPR-based techniques. (Fig. 4.1B).

This chapter will discuss the development of the post-biosynthetic modification strategy of FeMo-co to enable the incorporation of various heterometals, the substitution of Fe for Co in the terminal metal site of FeMo-co, and the incorporation of the Co-substituted cofactor (CoFeMo-co) into NafY (a nitrogenase cofactor carrier protein) and apo-NifDK.

4.2. Purification of the Fe1-deficient FeMo-co

Generation of CoFeMo-co largely follows the same workflow outlined in Chapter 2: (1) the isolation of FeMo-co using reported protocols;[22] (2) the post-biosynthetic modification of FeMo-co to incorporate Co into the terminal metal site; and (3) insertion of CoFeMo-co into a protein scaffold. The post-biosynthetic modification of FeMo-co to incorporate ^{57}Fe site-selectively (described in Chapter 2) entails incubation of the cofactor with excess EDTA and $^{57}Fe^{2+}$, generating the site-selectively labeled FeMo-co *in situ*. However, this procedure cannot be used for installing Co^{2+} or other mid-to-late, first-row, divalent transition-metal ions because the EDTA binding affinity for Fe^{2+} is relatively lower.[23] As a consequence, the addition of Co^{2+}, Ni^{2+}, Cu^{2+}, or Zn^{2+} into the FeMo-co + EDTA mixture would result in release of Fe^{2+} from the EDTA complex and afford a thermodynamic mixture of FeMo-co and the respective heterometal substituted cofactor. In fact, a previous study by Burgess had demonstrated this concept with Zn^{2+};[24] addition of Zn^{2+} to EDTA treated FeMo-co results in the generation of FeMo-co, not ZnFeMo-co. To generate any heterometal substituted cofactor cleanly, we had to develop a strategy for separating the Fe1-deficient FeMo-co (M(–Fe1)) from any Fe-bound chelator.

Our approach to purifying the M(–Fe1)) was to utilize its overall charge state in solution. Previous research[24] has established that FeMo-co is an anion; therefore, M(–Fe1) must be more anionic. We envisioned that we could immobilize M(–Fe1) onto an anion exchange column and separate it from other byproducts that likely are less anionic than M(–Fe1). Note that previous work from the Orme-Johnson[25-26] and Burgess[24] research groups have demonstrated the feasibility of applying ion-based chromatography

for purifying the isolated FeMo-co from exogenous Fe. Here we discuss our procedure to isolate and purify M(–Fe1) using diethylaminoethyl (DEAE) sepharose resin and demonstrate that it can be reconstituted with either Fe or Co.

As reported previously,[21] M(–Fe1) was generated by the addition of 30 equiv EDTA (Fig. 4.2). We have since discovered that in the presence of sodium dithionite (DTH) and thiophenol (PhSH), the EDTA treated cofactor exhibits an $S = ½$ EPR signal at 40 K with

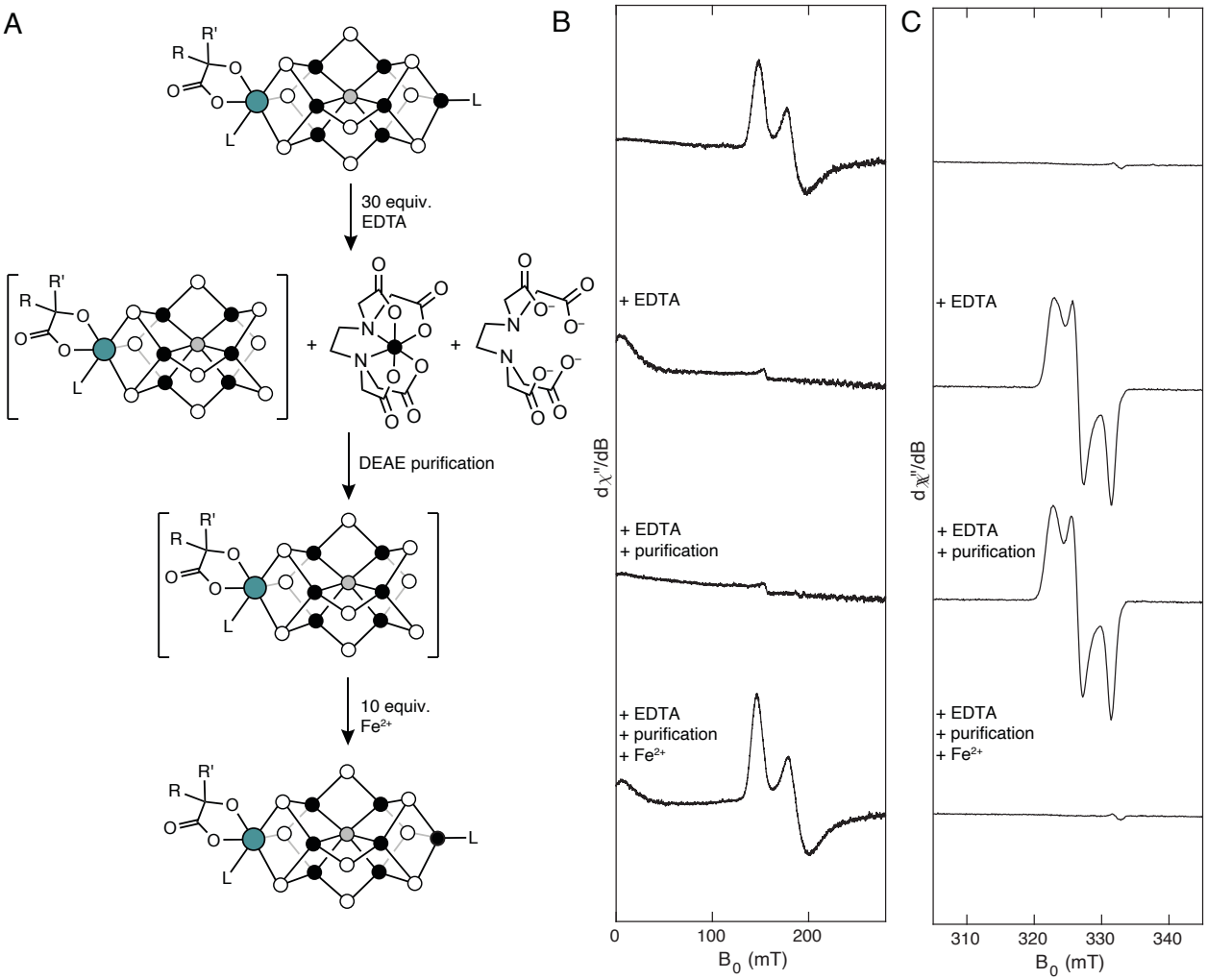

Figure 4.2. Generation and purification of M(–Fe1). A, The general strategy for isolating M(–Fe1) and its subsequent regeneration with excess Fe^{2+}. **B,** Corresponding EPR spectra recorded at 9.37 GHz, 5 K, and 1 mW. **C,** Corresponding EPR spectra recorded at 9.37 GHz, 40 K, and 250 μW. Full spectra of panels B and C are provided in Fig. S4.1. Black, white, gray, and teal circles represent Fe, S, C, and Mo, respectively. R,-$CH_2CO_2^-$; R′, -$(CH2)_2CO_2$.

$\boldsymbol{g} = [g_1, g_2, g_3] = [2.07, 2.05, 2.02]$ (Fig. 4.2C). The continuous-wave (CW) EPR spectrum of M(–Fe1), poised in the DTH reduced state with PhSH, before and after purification demonstrates (Fig. 4.2B) that the Fe-EDTA complex that is present in the EDTA treated sample (Fig. 4.2B, 2nd row) has been removed after purification (Fig. 4.2B, 3rd row); this is evident based on the disappearance of the low-field intensity that corresponds to high-spin octahedral Fe^{2+} ($S = 2$). We tentatively assign this new $S = ½$ species to M(–Fe1), as it is generated upon addition of EDTA, and is consumed upon addition of Fe^{2+} to quantitatively regenerate FeMo-co (Fig. 4.2B). Metal analysis of M(–Fe1) indicates that the Mo recovery from the starting isolated FeMo-co is about 80 to 90%; and more importantly it supports that the purification by anion exchange chromatography removes the chelated Fe, as the ratio of Mo:Fe decreases to approximately 6:1 (Table 4.1). With a protocol established to isolate M(–Fe1)), we next moved to its reconstitution with Co^{2+}.

Table 4.1. Metal analysis of FeMo-co and Fe1-deficient FeMo-co.

	Fe (μM)	Mo (μM)	Metal Ratio
FeMo-co	113 ± 1	15 ± 0.2	7.5 : 1
Fe1-deficient FeMo-co	221 ± 4	37 ± 1	6.0 : 1

4.3. Fe1-deficient cofactor reconstitution with Co^{2+}

EPR spectroscopy can be used to study the regeneration of FeMo-co as the EPR signal for mononuclear Fe^{2+} ($S = 2$) only contributes intensity at low field (0-50 mT). Because mononuclear Co^{2+} is $S = {}^3/_2$, its EPR spectrum contributes intensity to almost the entire breadth of the spectrum. This prohibits the assignment of any new EPR signals (associated with the generation of CoFeMo-co) and the assessment of FeMo-co regeneration as the Co^{2+} signal would dominate the spectrum. To assess the reconstitution of M(–Fe1) with Co^{2+}, we inserted the treated cofactor into NafY—a nitrogenase carrier protein thought to natively bind FeMo-co[27-28]—and purified the now holo-protein away from any mononuclear Co^{2+} (see Experimental and methods). Isolation of NafY–M(Co) (NafY loaded with CoFeMo-co) afforded a dark-brown solution, like that of NafY–M (NafY loaded with FeMo-co), indicating qualitatively that incubation with Co^{2+} did not destroy the cofactor. Metal analysis revealed that the NafY–M(Co) sample

contained a ratio of Fe:Co:Mo of approximately 6:1:1, suggesting a high incorporation of Co into FeMo-co (Table 4.2), as the proposed chemical composition of CoFeMo-co is [Fe_6CoMoC].

Table 4.2. Metal analysis of NafY–M(Co) and NifDK–M(Co)

	Fe (μM)	Co (μM)	Mo (μM)	Metal Ratio[a]
NafY–M(Co)	2030 ± 59	324 ± 3	361 ± 1	6 : 0.96 : 1.07
NifDK–M(Co)	1110 ± 7	72 ± 2	70 ± 1	14 : 0.91 : 0.88

[a]Normalized to theoretical Fe content of the respective sample.

We next turned to EPR spectroscopy to assess if any FeMo-co was present in this sample (in the DTH reduced state), and if the putative CoFeMo-co exhibited a new, novel EPR signal. In our EPR study, two samples were prepared (Fig. 4.3A): (1) NafY loaded with FeMo-co (NafY–M); and (2) NafY loaded with the putative Co-substituted cofactor (NafY–M(Co)). When FeMo-co is in its DTH reduced state (analogous to M^N in NifDK) bound to NafY it exhibits a strong $S = {}^3/_2$ EPR signal with $\boldsymbol{g_{eff}}$ = [4.42, 3.71, 2.00] (Fig. 4.3B, top).[28] An EPR silent state can readily be accessed by oxidizing the cofactor by one electron (analogous to M^{OX} in NifDK) with the addition of excess thionine. Contrary to NafY–M(Fe), the EPR spectrum of NafY–M(Co) in the DTH reduced state only contains a very weak $S = {}^3/_2$ EPR signal (Fig. 4.3B). This indicates that only a small portion of the Mo present in the sample can be assigned to FeMo-co (ca. 10% or less), perhaps suggesting that the rest of the intact cofactor is associated with the EPR silent CoFeMo-co. Indeed, one-electron oxidation of the NafY–M(Co) with excess thionine results in the appearance of a new $S = {}^1/_2$ signal centered at around g = 1.97 (Fig. 4.3C, bottom and S4.2). The EPR data presented on the NafY-bound cofactors are consistent with the expected EPR properties upon the substitution of Fe^{2+} for Co^{2+}; that is, upon substitution with one Co^{2+}, the total number of electrons in the cofactor is increased by one (with respect to the same charge state). Therefore, M^{OX} must be EPR active, and in this case has an $S = ½$ spin state, while M^N is EPR silent. Encouraged by the metal analysis and EPR spectra of NafY–M(Co), we next moved to inserting CoFeMo-co into apo-NifDK.

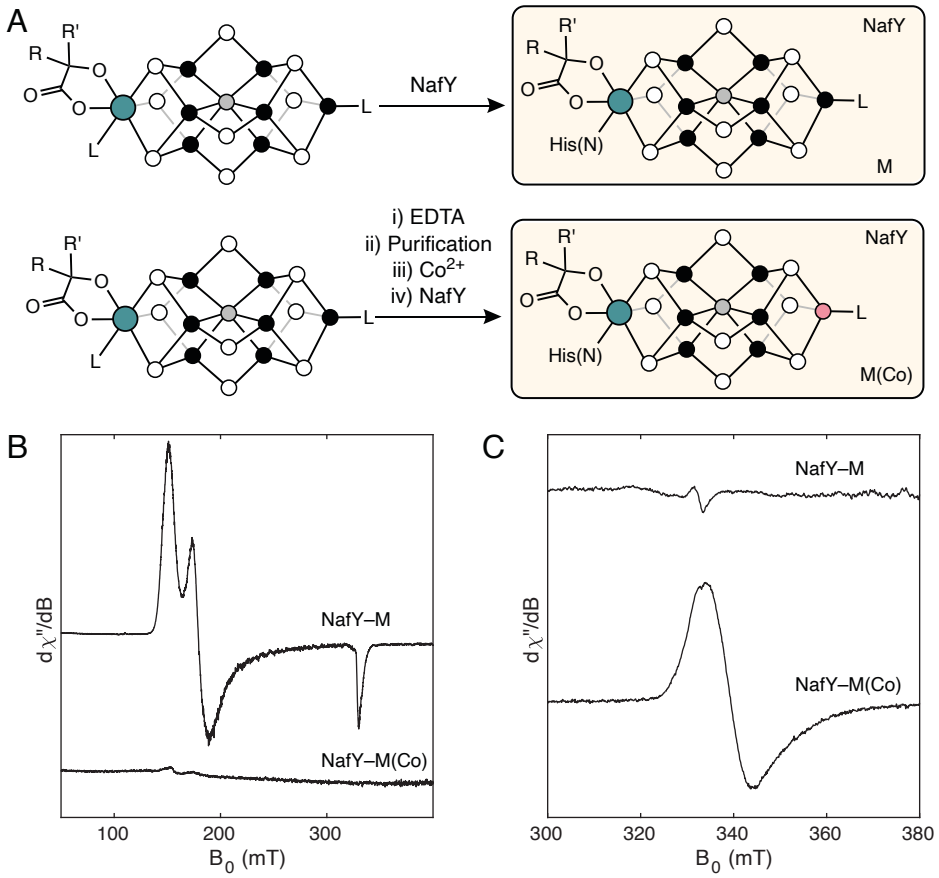

Figure 4.3. EPR analysis of the Co-substituted cofactor on NafY. A, Preparation of the NafY–M and NafY–M(Co) samples. **B,** Corresponding EPR spectra of both samples in the DTH reduced state recorded at 9.37 GHz, 5 K, and 1 mW. **C,** Corresponding EPR spectra in the thionine oxidized state recorded at 9.37 GHz, 12 K, and 1 mW. Full spectra are shown in Fig. S4.2. Black, white, gray, teal, and pink circles represent Fe, S, C, Mo, and Co, respectively. R,-$CH_2CO_2^-$; R′, -$(CH2)_2CO_2$.

A significant challenge with the generation of the NifDK–M(Co) sample was minimizing the substitution of the incorporated Co with any exogenous Fe present in the insertion mixture. In our previous protocol for generating the NifDK ^{57}Fe isotopologues, the cofactor insertion was accomplished by incubating FeMo-co with the crude lysate of DJ1143 (an *Azotobacter vinelandii* strain that produces His-tagged apo-NifDK) and subsequently purifying the resulting holo-protein. Using this protocol to generate NifDK–M(Co) resulted in a mixture of CoFeMo-co and FeMo-co in NifDK. We hypothesized that the exogenous Fe in the crude lysate would displace the terminal Co site prior to the cofactor insertion into apo-NifDK. To mitigate this side reaction, we used three strategies

to suppress the scrambling of the terminal metal site: (1) the addition of excess thiophenol (PhSH) (we hypothesized that it would bind to the terminal metal site and decrease the rate of metal scrambling during the insertion); (2) the partial purification of apo-NifDK using a DEAE-sepharose column (see methods) to remove any free mononuclear Fe in the crude lysate prior to the cofactor insertion; and (3) the addition of 100 equiv Co^{2+} to the partially purified apo-NifDK. The combination of these three strategies minimized the amount of FeMo-co present in the generation of NifDK–M(Co). Metal analysis of this sample after extensive purification (see Experiment and methods) afforded a sample with a ratio of Fe:Co:Mo of approximately 14:1:1 (Table 4.2), consistent with the proposed metal composition for NifDK–M(Co) (8 × Fe from the P-cluster; 6 × Fe, 1 × Mo, and 1 × Co from CoFeMo-co). Like with our NafY experiments, these metal ratios indicate close to full incorporation of CoFeMo-co (with little to no FeMo-co), along with the presence of an intact P-cluster.

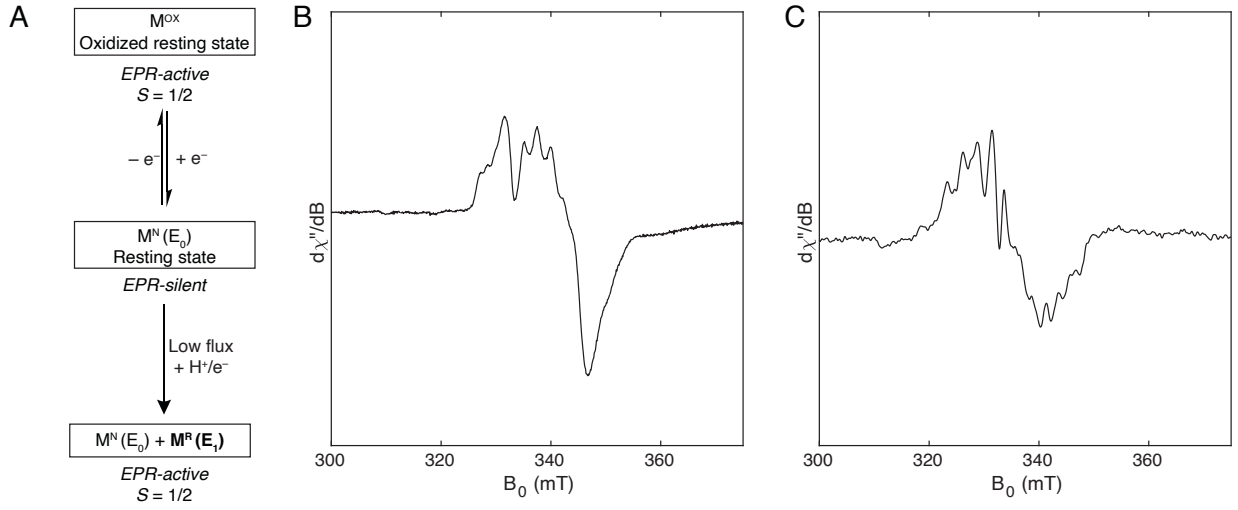

Figure 4.4. EPR Spectra of the Co-substituted cofactor on NifDK. A, Scheme showing how M^{OX} and $M^{R}(E_1)$. **B,** EPR spectrum of thionine oxidized NifDK–M(Co). This poises the cofactor in the M^{OX} state. Note the sharp feature at ~330 mT which corresponds to some residual thionine that has been subtracted out (Fig. S4.4). Recorded at 9.37 GHz, 15 K, and 1 mW. **C,** EPR spectrum of NifDK–M(Co) under low flux. Under these conditions CoFeMo-co is in a mixture of $M^{N}(E_0)$ and $M^{R}(E_1)$. The $M^{R}(E_1)$ state is EPR active and is S = ½. Note impurities from the resting state have been subtracted out (see Fig. S4.3). Recorded at 9.37 GHz, 15 K, and 1 mW.

Excited with the metal analysis of the putative NifDK–M(Co), we used EPR spectroscopy to assess (1) if any FeMo-co is present; and (2) if NifDK–M(Co) exhibited similar EPR properties to that of its NafY counterpart. Like NafY, the EPR spectrum of NifDK–M(Co) poised in the DTH reduced state (Fig. S4.3, top) exhibited a small amount of $S = {}^{3}/_{2}$ signal from FeMo-co (accounting for ca. less than 10% the total Mo content) and a minor $S = ½$ species (Fig. S4.3, bottom) most likely attributed to a small amount of degraded P-cluster (we observed similar species in the previously reported[21] NifDK isotopologue samples). One-electron oxidation of NifDK–M(Co) with excess thionine revealed a new axial $S = ½$ EPR signal (Fig. 4.4B and S4.4), and is consistent with what we observed in NafY. Interestingly—like the EPR signal for FeMo-co in NifDK—the $S = {}^{1}/_{2}$ signal is sharper than that of the NafY sample and more excitingly, the spectrum is rich with hyperfine features. Given that ^{59}Co is in 100% abundance and is $I = {}^{7}/_{2}$, we strongly believe the hyperfine arises due to the incorporation of Co; furthermore, there must be a sufficient spin density on the Co to observe such hyperfine features. Attempts to simulate the NifDK–M(Co) M^{OX} EPR signal—to extract the $\boldsymbol{A}(^{59}Co)$—have been unsuccessful as the Co hyperfine and the *g*-values of this species are not well-resolved at X-band. Future experiments at multiple different frequencies will address these issues.

An alternative explanation for observing an EPR spectrum with Co^{2+} hyperfine could be the presence of some contaminating Co^{2+} species. However, under these sample preparation conditions, the only reasonable ligands to Co^{2+} would be water-derived ligands (H_2O, OH^-), Cl^-, or different amino acid residues (His, Ser, Cys); these are all weak-field donors and therefore the Co^{2+} would be high-spin ($S = {}^{3}/_{2}$), inconsistent with the $S = {}^{1}/_{2}$ species we observe. Thus, we argue against assigning this EPR signal as non-specifically bound mononuclear Co. Altogether the metal analysis and EPR properties of both the NafY and NifDK samples are consistent with the substitution of Co^{2+} for Fe^{2+} in the terminal metal site of FeMo-co.

We next investigated if the integration of CoFeMo-co into NifDK yielded in an active enzyme, and if so, how it fares against WT His-NifDK. Given the myriad of substrates[5] that nitrogenases can reduce, such as H^+, C_2H_2, CN^-, CO, and N_2, we opted to focus on N_2 reduction, as it provides a stringent test for the generation and incorporation of

CoFeMo-co into NifDK. N_2 reduction using the Mo nitrogenase framework requires an intact cluster core with a homocitrate moiety and the correct placement of the cofactor within the active site pocket of NifDK; the reduction of other substrates, such as H^+ or C_2H_2, could be catalyzed by a cofactor with defects (*e.g.*, lacking the homocitrate) or located outside the desired binding site (*e.g.*, in the isolated state or non-specifically bound to the protein). As such, observation of N_2 reduction activity in the NifDK–M(Co) sample would provide additional evidence to support our structural assignment of the generated product—a [$MoFe_6CoS_9C$-homocitrate] cluster inserted in the cofactor binding pocket of NifDK. Using previously reported protocols,[29] we determined that the specific activity of NifDK–M(Co)[30] for N_2 reduction to NH_3 ranges from 20 to 50% of the control (WT His-NifDK). Although it is unclear why the range of specific activity for N_2 reduction is so large for the Co substituted Mo nitrogenase, a hypothesis is that upon cofactor insertion, the resulting protein is in multiple states. Recent experiments in our lab have hinted at this, where samples that contain excess Co and Mo can be converted to clean samples by subjecting them to high-flux turnover conditions and re-purifying them. Future studies will determine the specific activity of these post-turnover, re-purified samples. Regardless, the preliminary activity assays have demonstrated that NifDK–M(Co), to some extent, is an active nitrogenase and therefore the cofactor must be intact.

Given that this construct is active for catalysis, we next tested our hypothesis for using the Co-substituted cofactor as a mechanistic tool for understanding biological nitrogen fixation. Because we have demonstrated that the resting state of the Co-substituted cofactor, M^N, is EPR inactive and its corresponding oxidized state, M^{OX}, is EPR active ($S = 1/2$), the first intermediate of nitrogen fixation, E_1 (where CoFeMo-co is in the M^R state), must be EPR active (Fig. 4.1B) as it is the product of adding one electron and one proton to the EPR-silent E_0 state. This intermediate would then be amenable to characterization using techniques such as ENDOR or magnetic Mössbauer spectroscopy. As described in Chapter 3, it has been previously reported that subjecting WT NifDK to low-flux turnover conditions (*i.e.*, turnover conditions in which NifDK is in vast excess to the FeP) generates a mixture of E_0 and E_1 (FeMo-co in M^N or M^R for E_0 and E_1, respectively).[31-35] We hypothesized that under similar conditions, the Co-

substituted Mo nitrogenase would also generate a mixture of E_0 and E_1. The NifDK–M(Co) EPR spectrum under low flux turnover is shown in Fig. 4.4C and S4.5, and shows a new $S = {}^1/_2$ EPR signal centered around $g = 2.00$. Excitingly, the EPR signal, like in M^{OX}, exhibits what we assign as Co hyperfine, suggesting that this new EPR signal arises due to CoFeMo-co being in the M^R state; multi-frequency EPR experiments are planned for this EPR species as well. We have demonstrated that the Co-substituted Mo nitrogenase can be used to study the chemical and electronic structure of E_n ($n = 1, 3, 5, 7$) states as these states are EPR active. The next paragraph will discuss the future directions with the system.

4.4. Conclusions and future directions of the Co-substituted cofactor

Here we report the expansion of the site-selective ^{57}Fe labeling of FeMo-co to the site-selective substitution of the terminal Fe to Co. To overcome the thermodynamic limitations with incorporating Co into isolated FeMo-co in the presence of EDTA, we developed a method to purify M(–Fe1) in its isolated state. Reconstitution of the purified M(–Fe1) with Co^{2+} and subsequent insertion into either NafY or apo-NifDK afforded the corresponding CoFeMo-co loaded protein. EPR studies of both samples revealed that CoFeMo-co, in the presence of DTH, is EPR-silent; this is distinct from that of FeMo-co which exhibits an $S = {}^3/_2$ EPR signal. Oxidation of both NafY and NifDK samples by one electron afforded a novel $S = {}^1/_2$ EPR signal, with the NifDK–M(Co) EPR spectrum containing Co-hyperfine features. We also demonstrated that NifDK–M(Co) is a nitrogenase, opening the door for using this sample as a mechanistic tool. As an example, we demonstrated that under low flux turnover, the E_1 state can be generated and that it has an overall spin state of $S = ½$; like the M^{OX} state, the EPR spectrum of CoFeMo-co in the M^R state exhibits Co hyperfine. Because the EPR-inactive states in the native enzyme are now EPR-active with the Co-substituted cofactor, techniques such as ENDOR and magnetic Mössbauer spectroscopy can be used to elucidate the electronic and chemical structure of these intermediates. For example, ^{1}H ENDOR studies on the E_1 state of NifDK–M(Co), analogous to those performed on the Janus intermediate of WT NifDK, can determine the site of protonation (at an Fe *vs.* at a S). Previous studies of the

Mo nitrogenase have not been able to address this question because this intermediate is EPR inactive. In addition to the studies of CoFeMo-co, the isolation of M(–Fe1) enables the generation of other heterometal-substituted cofactors. Work in this area is in progress.

4.5. Supplemental information

4.5.1. Additional EPR spectra

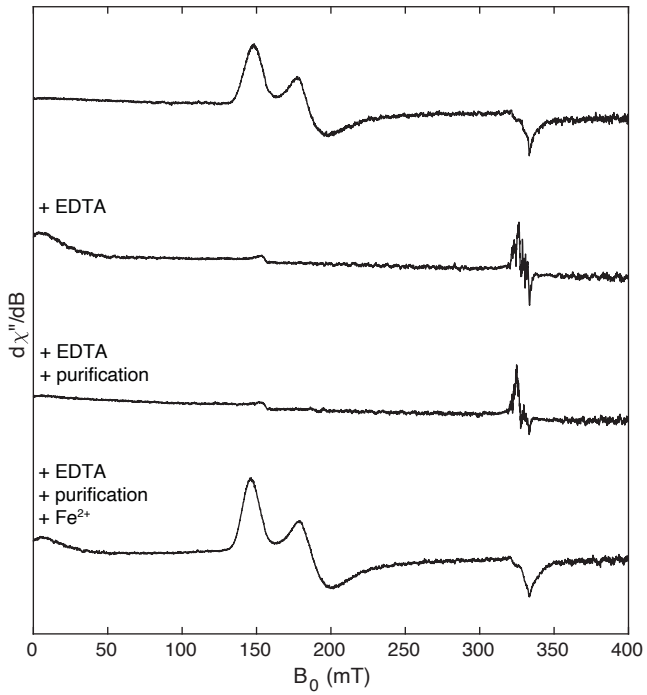

Figure S4.1. Full EPR spectra of the generation and purification of Fe1-deficient FeMo-co. Recorded at 9.37 GHz, 5 K, and 1 mW.

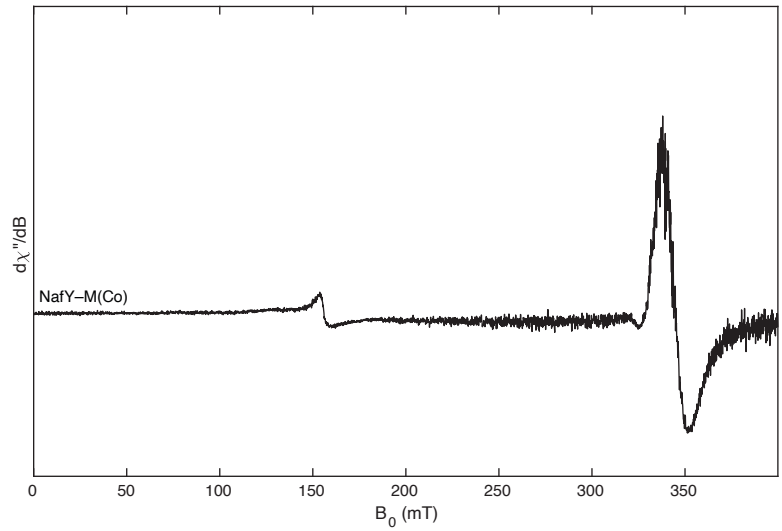

Figure S4.2. Full EPR Spectra of the Co-substituted cofactor on NafY in the thionine oxidized state. The full EPR spectra of thionine oxidized NafY–M(Co). Recorded at 9.37 GHz, 5 K, and 1 mW.

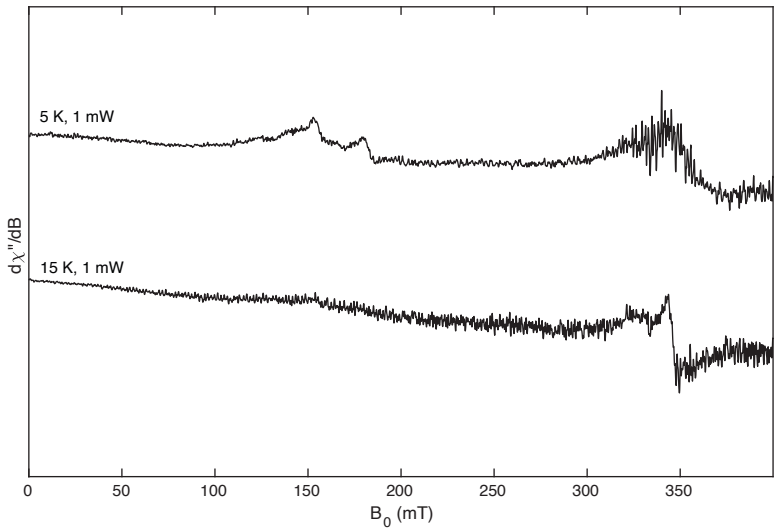

Figure S4.3. EPR Spectra of the Co-substituted cofactor on NifDK in the DTH reduced state. EPR spectra of DTH reduced NifDK–M(Co). The top spectrum was recorded at 9.37 GHz, 5 K, and 1 mW. The bottom spectrum was recorded at 9.37 GHZ, 15 K, and 1 mW. Note the species at around $g = 2$ corresponds to degraded P-cluster.

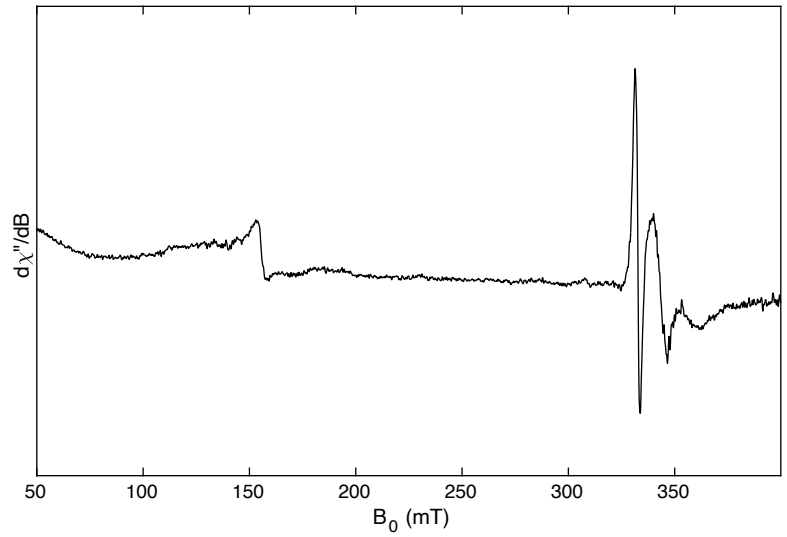

Figure S4.4. EPR Spectrum of the Co-substituted cofactor on NifDK in the thionine oxidized state. EPR spectrum of thionine oxidized NifDK–M(Co). Recorded at 9.37 GHz, 5 K, and 1 mW.

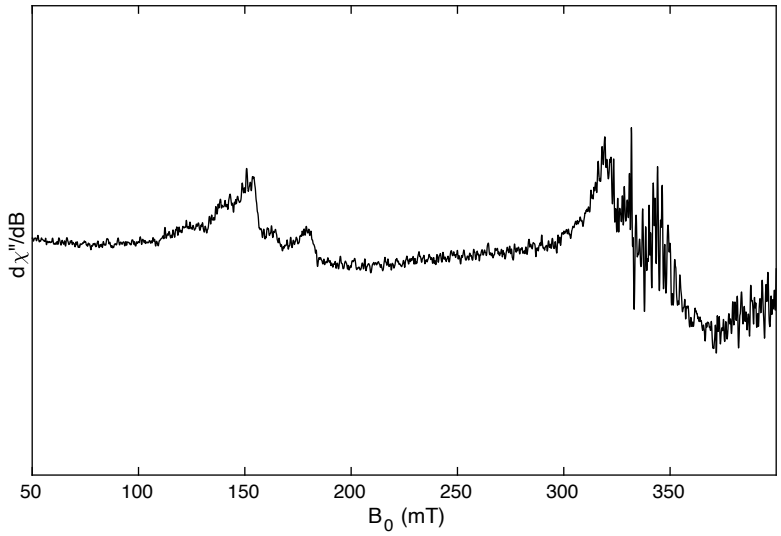

Figure S4.5. EPR Spectrum of the Co-substituted cofactor on NifDK under low flux turnover. EPR spectrum of the NifDK–M(Co) sample under low flux turnover (see methods). Recorded at 9.37 GHz, 5 K, and 1 mW.

4.6. Experimental and methods

Cell growth

The *Azotobacter vinelandii* strains DJ1141 (produces His-tagged NifDK), DJ1143 (produces His-tagged apo-NifDK), and wild-type (WT) *A. vinelandii* were cultured in 18 L batches in a 20 L B. Braun Biostat C bioreactor using Burk's minimal medium (6 mM sucrose, 0.9 mM $MgSO_4 \cdot 7H_2O$, 0.6 mM $CaCl_2 \cdot 2H_2O$, 18 µM $FeSO_4 \cdot 7H_2O$, 2 mM KH_2PO_4, 2 mM KH_2PO_4, 5 mM KH_2PO_4) supplemented with 1 µM $Na_2MoO_4 \cdot 2H_2O$.

For overproducing holo-NifDK and apo-NifDK, growths were supplemented with 6 mM ammonium acetate (BN media). Derepression was initiated upon ammonium depletion, and cells were harvested after 3 hours.[36] Cell paste was flash-frozen in LN_2 and stored at –80 °C until purification.

NifDK purification

All NifDK purification procedures were carried out in a Coy Labs glove box (<5 ppm O_2). All aqueous solutions used were sparged with N_2 overnight. Cells were lysed using the osmotic shock method as followed: DJ1141 cell paste was resuspended with 3 mL of 25 mM HEPES pH 7.5, 50% glycerol, and 2 mM sodium dithionite (DTH) for every gram of cell paste. After stirring at room temperature for 15 minutes, the cells were pelleted at 25,000 × g for 15 minutes. The supernatant was poured off and the pelleted cells were resuspended with 3 mL buffer containing 25 mM HEPES pH 7.5, 2 mM DTH, 3 mM phenylmethylsulfonyl fluoride (PMSF), 1 mg/mL lysozyme, and 100 µg/mL DNase I for every gram of cell paste. After 15 minutes of stirring, the lysate was pelleted at 100,000 × g for 1 hour and loaded onto a Ni-NTA column equilibrated with buffer containing 500 mM NaCl, 25 mM HEPES pH 7.5, 20% glycerol, and 2 mM DTH. The immobilized protein was washed with 10 column volumes of equilibration buffer and eluted with equilibration buffer containing 200 mM imidazole. NifDK was further purified using anion exchange chromatography: the protein solution was diluted 4-fold with buffer containing 25 mM HEPES pH 7.5, 20% glycerol, and 2 mM DTH and then loaded onto a DEAE-sepharose column charged with NaCl and equilibrated with the dilution buffer. The column was washed with 10 column volumes of 160 mM NaCl, 25 mM HEPES pH 7.5, 2 mM DTH,

and 20% glycerol. The immobilized protein was then eluted with buffer containing 500 mM NaCl, 25 mM HEPES pH 7.5, 2 mM DTH, and 20% glycerol. Purified NifDK was concentrated using an AMICON stirred cell equipped with a 30 kDa filter, flash-frozen, and stored in LN_2. The concentration of NifDK was estimated by determining the Mo content using inductively coupled plasma mass spectrometry (ICP-MS).

Note: In our study, the reported concentration of NifDK is based on the αß heterodimer concentration (with one FeMo-co per heterodimer in holo-NifDK) rather than the $\alpha_2ß_2$ heterotetramer concentration (with two FeMo-co per heterotetramer in holo-NifDK).

NifH purification

The purification of NifH was carried out in an MBRAUN glove box (<5 ppm O_2) and was performed similarly to what has been previously reported.[37] WT *A. vinelandii* cell paste was lysed as described above. Lysate was loaded onto a DE-52 column charged with NaCl and equilibrated in 25 mM HEPES pH 7.5 and 2 mM DTH. The column was washed with a stepwise gradient with buffer containing 125 mM, 200 mM, 300 mM, and 500 mM NaCl. Fractions were analyzed by EPR spectroscopy; those determined to have NifH were pooled and concentrated using a DE-52 cellulose column and AMICON spin filters equipped with a 10 kDa filter. NifH was then purified further using an Superdex 200 column equilibrated with buffer containing 200 mM NaCl, 25 mM HEPES pH 7.5, and 2 mM DTH. Purified NifH was subsequently concentrated and flash-frozen in LN_2. The concentration of NifH was estimated by UV-vis spectroscopy.[37]

Isolation of FeMo-co

The protocol for FeMo-co isolation was adapted from a previously reported procedure.[22] Protein manipulation was performed in a Coy Labs glove box (<5 ppm O_2) and FeMo-co manipulation was carried out in an MBRAUN or Vacuum Atmospheres glove box (<5 ppm O_2). NifDK (typical protein concentrations ranging from 100 to 400 µM αß dimer) was diluted 10-fold with aqueous 2 mM DTH. The protein was denatured by the addition of 100 mM citric acid (1.67 mL per 10 mL of diluted protein) added dropwise at 0 ˚C with stirring. After incubating the mixture for 30 s the protein was precipitated by

addition of 200 mM Na_2HPO_4 (1.7 mL per 10 mL of diluted protein). The precipitated protein was transferred to a 15 mL conical tube and moved to the Mbraun box where the protein was pelleted at 120 × g for 5 min using a Labnet Z100A centrifuge. The supernatant was removed and the pellet was washed with *N,N*-dimethylformamide (DMF) (5 mL) and pelleted. This DMF wash step was performed once more. FeMo-co was then extracted by resuspending and vortexing the pellet with 1 to 2 mL of *N*-methylformamide (NMF) containing 2 mM Na_2HPO_4 (from a 200 mM aqueous stock solution). After a 5-minute incubation at room temperature, the extract was centrifuged at 500 × g for 5 minutes, and the brown supernatant was poured off and collected. The process was repeated until the solution was colorless, and the extracts were combined. The concentration of FeMo-co was estimated by UV-vis spectroscopy using an extinction coefficient of PhS-bound FeMo-co in NMF: 14,800 $M^{-1}\,cm^{-1}$ at 450 nm (See Chapter 2).

Post-biosynthetic modification of FeMo-co (Co-incorporation)

Isolated FeMo-co was treated with 30 equiv EDTA (added as a 100 mM aqueous stock solution), mixed, and incubated at room temperature for 5 minutes. Then the treated cofactor was immobilized onto a DEAE column equilibrated in NMF. The immobilized Fe-deficient cofactor was washed with 5 column volumes of NMF containing 65 mM tetraethylammonium chloride and eluted with 3 column volumes of NMF containing 500 mM tetraethylammonium chloride. The concentration of Fe-deficient cofactor was determined using a molar extinction coefficient of 9500 $M^{-1}\,cm^{-1}$ at 450 nm. To generate the Co-substituted cofactor, 10 equiv $CoCl_2$ (added as a 100 mM aqueous stock solution in 200 mM HEPES, pH 7.5) was added followed by 2 mM DTH and 2 mM PhSH (final concentrations).

Preparation of partially purified apo-NifDK protein

DJ1143 cells were lysed using the osmotic shock method as followed: DJ1143 cell paste was resuspended with 3 mL of 25 mM HEPES pH 7.5, 50% glycerol, and 2 mM sodium dithionite (DTH) for every gram of cell paste and pelleted by centrifugation at 100,000 × g for 15 min. The supernatant was poured off and the pelleted cells were resuspended with 3 mL buffer containing 25 mM HEPES pH 7.5, 2 mM sodium dithionite,

3 mM phenylmethylsulfonyl fluoride (PMSF), 1 mg/mL lysozyme, and 100 µg/mL DNase I for every gram of cell paste. After 15 minutes of stirring, the lysate was pelleted at 100,000 × g for 1 hr, and the cleared lysate was loaded onto a DEAE Sepharose column charged with NaCl and equilibrated with 25 mM HEPES pH 7.5, 20% glycerol, and 2 mM DTH. The column was then washed with the equilibration buffer until the flowthrough was clear (typically around 5 column volumes). The immobilized proteins were then eluted with a buffer containing 500 mM NaCl, 25 mM HEPES pH 7.5, 2 mM DTH, and 20% glycerol. The eluate was then diluted to the appropriate volume such that the final concentration of NMF after cofactor addition is 1% (v/v). The amount of DJ1143 cell pasted used for each experiment was determined by independently measuring the yield of apo-NifDK isolated from a single Ni-NTA column per gram of DJ1143 cell paste.

Overexpression of NafY

The pDB2118 plasmid which contains the *nafY* gene with an N-terminal Strep-tag on a pT7-7 expression vector (amp resistance) was generously gifted from the Dean lab.[38] *E. coli* BL-21(DE3) pLysS was transformed with the pDB2118 plasmid. An overnight LB media starter culture supplemented with 100 µg/mL of ampicillin was inoculated from a single colony and incubated at 250 RPM at 37 °C. 50 mL of the overnight starter culture was used to inoculate a 16 L batch of LB media (20-L B. Braun Biostat C bioreactor). The growth was cultured at 37 °C, with stirring at 200 rpm and a continuous air flow of 15 L per min. Overexpression of the *nafY* gene was induced at 30 °C with 40 g of lactose at an OD_{600} of approximately 0.4. Cells were harvested 3 hours after induction by centrifugation, flash frozen in LN_2, and stored at –80 °C until purification.

Purification of NafY

The purification of Strep-tagged NafY was adapted from previous procedures.[20, 38] First, *E. coli* cells were lysed using the osmotic shock method described for *Av.* The cleared lysate was applied to a Strep column equilibrated with 25 mM HEPES, pH 7.5 and 10% glycerol. The column was then washed with five column volumes of the equilibration buffer and the protein was eluted using the equilibration buffer containing 50 mM biotin. The isolated protein was concentrated using an AMICON stirred cell equipped

with a 10 kDa filter and gel-filtered into the equilibration buffer using a PD10 column. The concentration of NafY was estimated using the absorbance at 280 nm with ε_{280} = 20110 M^{-1} cm^{-1} obtained from the ProtParam tool from Expasy Proteomics Resource Portal.[39]

Insertion of CoFeMo-co into NafY

The procedure for inserting CoFeMo-co into NafY was adapted from what we reported previously for the L-cluster.[20] CoFeMo-co was inserted into NafY by adding it dropwise to a solution of NafY diluted in 25 mM HEPES pH 7.5, 5 % glycerol, and 2 mM DTH such that the final concentration of NMF after cofactor addition is 1% (v/v). NafY was always present in excess (up to 1.5 equiv) as adding CoFeMo-co in excess resulted in FeMo-co generation (any excess FeMo-co eventually degrades liberating 6 equiv. of Fe which can substitute the Co). Following cofactor addition, the resulting holo-NafY was concentrated using an AMICON stirred cell equipped with a 10 kDa filter. The concentrated sample was purified through size-exclusion chromatography using a Superdex 200 column. The dark brown eluate was concentrated and flash frozen and stored in LN_2 until further use.

Insertion of CoFeMo-co into apo-NifDK protein

The procedure for inserting CoFeMo-co into apo-NifDK was adapted from what we reported[21] for the site-selective incorporation of ^{57}Fe, as well as protocols reported previously.[35, 40] To the stirred solution of freshly prepared, partially purified apo-NifDK at room temperature were added ATP (final concentration 500 µM), $MgCl_2$ (final concentration 500 µM), and $CoCl_2$ (100 equiv with respect to apo-NifDK), followed by the dropwise addition of freshly generated CoFeMo-co. Immediately after the addition of CoFeMo-co, the insertion mixture was quickly loaded onto a Ni-NTA column equilibrated with equilibration buffer (25 mM HEPES pH 7.5, 20% glycerol, and 2 mM DTH). After loading, the column was quickly washed with 10 column volumes of equilibration buffer containing 10 mM imidazole, before the protein was eluted with equilibration buffer containing 200 mM imidazole. NifDK–M(Co) was then further purified using a DEAE Sepharose column as described for the purification holo-NifDK. Once isolated, the protein was concentrated to about 5 mL and subjected to the high flux turnover condition, before

being concentrated and further purified using a Superdex 200 column as described previously.

N_2 reduction assays

The specific activity of NifDK was assessed using the N_2 reduction activity assay. Assays were performed in 10-mL crimped vials under an atmosphere of N_2 in a water bath at 30 °C. Each assay contained 500 µL ATP mix (25 mM Tris buffer, pH 7.9, 30 mM creatine phosphate disodium salt, 5 mM ATP disodium salt, 5 mM $MgCl_2$, 25 units mL^{-1} phosphocreatine kinase, and 20 mM DTH), 50 µg NifDK and 400 µg NifH. Assays were initiated with the addition of NifH and quenched after 15 min with 400 µL of 4 M NaCl. NH_3 production was measured using a modified *o*-phthalaldehyde (OPA) fluorescence detection method.[41] Quenched samples were centrifuged with a 10 kDa cutoff AMICON filter. The flowthrough of each sample was diluted 5-fold with ddH_2O and 200 µL of the diluted sample was added into 3.8 mL of the active OPA assay solution. The resulting mixture was incubated for 2 hr before the fluorescence measurement. The active OPA assay solution is comprised of a 1:1 mixture of 10 mM OPA in 25% MeOH and 6 mM Na_2SO_3, 100 mM sodium phosphate, pH 11.0. These stock solutions were prepared freshly in the dark. Fluorescence was measured at an excitation wavelength of 365 nm and an emission wavelength of 422 nm. Calibration curves were prepared with NH_4Cl in parallel with the samples.

Spectroscopy and spectrometry

EPR samples were prepared in an anaerobic glove box with an N_2 atmosphere and an O_2 level of <5 ppm. X-band EPR spectra were recorded on a Bruker EMX spectrometer at 9.37 GHz. Q-band ENDOR data were collected using a locally constructed spectrometer.[42] Inductively coupled plasma mass spectrometer (ICP-MS) data were recorded on an Agilent 7900 ICP-MS instrument. Protein samples were digested with concentrated nitric acid (TraceMetal Grade, Fischer) at 70 °C and were diluted with Milli-Q water to final concentration of 2% nitric acid. Standards for Fe, Mo and Co were prepared from a 1000 ppm standard solution (VWR BDH Chemicals).

4.7. References

1. Ahmed, M. H., Ghatge, M. S. & Safo, M. K., Hemoglobin: Structure, Function and Allostery. *Subcell Biochem* **2020,** *94*, 345-382.
2. Shimizu, T., Huang, D., Yan, F., Stranava, M., Bartosova, M., Fojtíková, V. & Martínková, M., Gaseous O_2, NO, and CO in Signal Transduction: Structure and Function Relationships of Heme-Based Gas Sensors and Heme-Redox Sensors. *Chemical Reviews* **2015,** *115* (13), 6491-6533.
3. Broderick, J. B., Duffus, B. R., Duschene, K. S. & Shepard, E. M., Radical S-Adenosylmethionine Enzymes. *Chemical Reviews* **2014,** *114* (8), 4229-4317.
4. Manikandan, P. & Nagini, S., Cytochrome P450 Structure, Function and Clinical Significance: A Review. *Current Drug Targets* **2018,** *19* (1), 38-54.
5. Seefeldt, L. C., Yang, Z.-Y., Lukoyanov, D. A., Harris, D. F., Dean, D. R., Raugei, S. & Hoffman, B. M., Reduction of Substrates by Nitrogenases. *Chemical Reviews* **2020,** *120* (12), 5082-5106.
6. Can, M., Armstrong, F. A. & Ragsdale, S. W., Structure, Function, and Mechanism of the Nickel Metalloenzymes, CO Dehydrogenase, and Acetyl-CoA Synthase. *Chemical Reviews* **2014,** *114* (8), 4149-4174.
7. Moore, E. J., Steck, V., Bajaj, P. & Fasan, R., Chemoselective Cyclopropanation over Carbene Y-H Insertion Catalyzed by an Engineered Carbene Transferase. *Journal of Organic Chemistry* **2018,** *83* (14), 7480-7490.
8. Kleingardner, J. G., Kandemir, B. & Bren, K. L., Hydrogen evolution from neutral water under aerobic conditions catalyzed by cobalt microperoxidase-11. *Journal of the American Chemical Society* **2014,** *136* (1), 4-7.
9. Key, H. M., Dydio, P., Liu, Z., Rha, J. Y. E., Nazarenko, A., Seyedkazemi, V., Clark, D. S. & Hartwig, J. F., Beyond Iron: Iridium-Containing P450 Enzymes for Selective Cyclopropanations of Structurally Diverse Alkenes. *ACS Central Science* **2017,** *3* (4), 302-308.
10. Key, H. M., Dydio, P., Clark, D. S. & Hartwig, J. F., Abiological catalysis by artificial haem proteins containing noble metals in place of iron. *Nature* **2016,** *534* (7608), 534-7.
11. Hoffman, B. M. & Petering, D. H., Coboglobins: Oxygen-Carrying Cobalt-Reconstituted Hemoglobin and Myoglobin. *Proceedings of the National Academy of Sciences* **1970,** *67* (2), 637-643.
12. Maxwell, J. C. & Caughey, W. S., Infrared evidence for similar metal-dioxygen bonding in iron and cobalt oxyhemoglobins. *Biochemical and Biophysical Research Communications* **1974,** *60* (4), 1309-1314.
13. Yonetani, T., Yamamoto, H. & Woodrow, G. V., 3rd, Studies on cobalt myoglobins and hemoglobins. I. Preparation and optical properties of myoglobins and hemoglobins containing cobalt proto-, meso-, and deuteroporphyrins and thermodynamic characterization of their reversible oxygenation. *Journal of Biological Chemistry* **1974,** *249* (3), 682-90.
14. Tsubaki, M. & Yu, N. T., Resonance Raman investigation of dioxygen bonding in oxycobaltmyoglobin and oxycobalthemoglobin: structural implication of splittings of the

bound O–O stretching vibration. *Proceedings of the National Academy of Sciences* **1981,** *78* (6), 3581-3585.
15. Wagner, G. C., Gunsalus, I. C., Wang, M. Y. & Hoffman, B. M., Cobalt-substituted cytochrome P-450cam. *Journal of Biological Chemistry* **1981,** *256* (12), 6266-6273.
16. Mackin, H. C., Tsubaki, M. & Yu, N. T., Resonance Raman studies of Co-O_2 and O-O stretching vibrations in oxy-cobalt hemes. *Biophysical Journal* **1983,** *41* (3), 349-57.
17. Bruha, A. & Kincaid, J. R., Resonance Raman studies of dioxygen adducts of cobalt-substituted heme proteins and model compounds. Vibrationally coupled dioxygen and the issues of multiple structures and distal side hydrogen bonding. *Journal of the American Chemical Society* **1988,** *110* (18), 6006-6014.
18. Martinie, R. J., Pollock, C. J., Matthews, M. L., Bollinger, J. M., Jr., Krebs, C. & Silakov, A., Vanadyl as a Stable Structural Mimic of Reactive Ferryl Intermediates in Mononuclear Nonheme-Iron Enzymes. *Inorganic Chemistry* **2017,** *56* (21), 13382-13389.
19. Davis, K. M., Altmyer, M., Martinie, R. J., Schaperdoth, I., Krebs, C., Bollinger, J. M., Jr. & Boal, A. K., Structure of a Ferryl Mimic in the Archetypal Iron(II)- and 2-(Oxo)-glutarate-Dependent Dioxygenase, TauD. *Biochemistry* **2019,** *58* (41), 4218-4223.
20. Srisantitham, S., Badding, E. D. & Suess, D. L. M., Postbiosynthetic modification of a precursor to the nitrogenase iron–molybdenum cofactor. *Proceedings of the National Academy of Sciences* **2021,** *118* (11), e2015361118.
21. Badding, E. D., Srisantitham, S., Lukoyanov, D. A., Hoffman, B. M. & Suess, D. L. M., Connecting the geometric and electronic structures of the nitrogenase iron–molybdenum cofactor through site-selective ^{57}Fe labelling. *Nature Chemistry* **2023**.
22. Shah, V. K. & Brill, W. J., Isolation of an iron-molybdenum cofactor from nitrogenase. *Proceedings of the National Academy of Sciences* **1977,** *74* (8), 3249-53.
23. Schwarzenbach, G. & Freitag, E., Komplexone XX. Stabilitätskonstanten von Schwermetallkomplexen der Äthylendiamin-tetraessigsäure. *Helvetica Chimica Acta* **1951,** *34* (5), 1503-1508.
24. Yang, S. S., Pan, W. H., Friesen, G. D., Burgess, B. K., Corbin, J. L., Stiefel, E. I. & Newton, W. E., Iron-molybdenum cofactor from nitrogenase. Modified extraction methods as probes for composition. *Journal of Biological Chemistry* **1982,** *257* (14), 8042-8048.
25. McLean, P. A., Wink, D. A., Chapman, S. K., Hickman, A. B., McKillop, D. M. & Orme-Johnson, W. H., A new method for extraction of iron-molybdenum cofactor (FeMoco) from nitrogenase adsorbed to DEAE-cellulose. 1. Effects of anions, cations, and preextraction treatments. *Biochemistry* **1989,** *28* (24), 9402-6.
26. Wink, D. A., McLean, P. A., Hickman, A. B. & Orme-Johnson, W. H., A new method for extraction of iron-molybdenum cofactor (FeMoco) from nitrogenase adsorbed to DEAE-cellulose. 2. Solubilization of FeMoco in a wide range of organic solvents. *Biochemistry* **1989,** *28* (24), 9407-12.
27. George, S. J., Igarashi, R. Y., Xiao, Y., Hernandez, J. A., Demuez, M., Zhao, D., Yoda, Y., Ludden, P. W., Rubio, L. M. & Cramer, S. P., Extended X-ray absorption fine structure and nuclear resonance vibrational spectroscopy reveal that NifB-co, a FeMo-co precursor, comprises a 6Fe core with an interstitial light atom. *Journal of the American Chemical Society* **2008,** *130* (17), 5673-80.

28. Rubio, L. M., Singer, S. W. & Ludden, P. W., Purification and characterization of NafY (apodinitrogenase gamma subunit) from Azotobacter vinelandii. *Journal of Biological Chemistry* **2004,** *279* (19), 19739 - 19746.
29. Rutledge, H. L., Rittle, J., Williamson, L. M., Xu, W. A., Gagnon, D. M. & Tezcan, F. A., Redox-Dependent Metastability of the Nitrogenase P-Cluster. *Journal of the American Chemical Society* **2019,** *141* (25), 10091-10098.
30. Determining a more precise specific activity for the Co-substituted Mo nitrogenase is ongoing.
31. Christiansen, J., Tittsworth, R. C., Hales, B. J. & Cramer, S. P., Fe and Mo EXAFS of Azotobacter vinelandii Nitrogenase in Partially Oxidized and Singly Reduced Forms. *Journal of the American Chemical Society* **1995,** *117* (40), 10017-10024.
32. Harris, D. F., Yang, Z.-Y., Dean, D. R., Seefeldt, L. C. & Hoffman, B. M., Kinetic Understanding of N_2 Reduction versus H_2 Evolution at the E_4(4H) Janus State in the Three Nitrogenases. *Biochemistry* **2018,** *57* (39), 5706-5714.
33. Van Stappen, C., Davydov, R., Yang, Z.-Y., Fan, R., Guo, Y., Bill, E., Seefeldt, L. C., Hoffman, B. M. & DeBeer, S., Spectroscopic Description of the E_1 State of Mo Nitrogenase Based on Mo and Fe X-ray Absorption and Mössbauer Studies. *Inorganic Chemistry* **2019,** *58* (18), 12365-12376.
34. Van Stappen, C., Thorhallsson, A. T., Decamps, L., Bjornsson, R. & DeBeer, S., Resolving the structure of the E_1 state of Mo nitrogenase through Mo and Fe K-edge EXAFS and QM/MM calculations. *Chemical Science* **2019,** *10* (42), 9807-9821.
35. Yoo, S. J., Angove, H. C., Papaefthymiou, V., Burgess, B. K. & Münck, E., Mössbauer Study of the MoFe Protein of Nitrogenase from *Azotobacter vinelandii* Using Selective ^{57}Fe Enrichment of the M-Centers. *Journal of the American Chemical Society* **2000,** *122* (20), 4926-4936.
36. Lee, C.-C., Ribbe, M. W. & Hu, Y., Purification of Nitrogenase Proteins. In *Metalloproteins: Methods and Protocols*, Hu, Y., Ed. Springer New York: New York, NY, 2019; pp 111-124.
37. Burgess, B. K., Jacobs, D. B. & Stiefel, E. I., Large-scale purification of high activity *Azotobacter vinelandII* nitrogenase. *Biochimica et Biophysica Acta (BBA) - Enzymology* **1980,** *614* (1), 196-209.
38. Jimenez-Vicente, E., Yang, Z. Y., Ray, W. K., Echavarri-Erasun, C., Cash, V. L., Rubio, L. M., Seefeldt, L. C. & Dean, D. R., Sequential and differential interaction of assembly factors during nitrogenase MoFe protein maturation. *Journal of Biological Chemistry* **2018,** *293* (25), 9812-9823.
39. Duvaud, S., Gabella, C., Lisacek, F., Stockinger, H., Ioannidis, V. & Durinx, C., Expasy, the Swiss Bioinformatics Resource Portal, as designed by its users. *Nucleic Acids Research* **2021,** *49* (W1), W216-W227.
40. McLean, P. A., Papaefthymiou, V., Orme-Johnson, W. H. & Münck, E., Isotopic hybrids of nitrogenase. Mössbauer study of MoFe protein with selective ^{57}Fe enrichment of the P-cluster. *Journal of Biological Chemistry* **1987,** *262* (27), 12900-12903.
41. Genfa, Z. & Dasgupta, P. K., Fluorometric measurement of aqueous ammonium ion in a flow injection system. *Analytical Chemistry* **1989,** *61* (5), 408-412.

42. Davoust, C. E., Doan, P. E. & Hoffman, B. M., Q-Band Pulsed Electron Spin-Echo Spectrometer and Its Application to ENDOR and ESEEM. *Journal of Magnetic Resonance, Series A* **1996,** *119* (1), 38-44.